Computational Study of Convective Cooling and Windage Losses of Axial Flux Permanent Magnet Synchronous Machines

Computationele studie van de convectieve koeling en luchtcirculatieverliezen van permanentemagneetbekrachtigde synchrone machines met axiale flux

Alireza Rasekh

Promotoren: prof. dr. ir. J. Vierendeels, prof. dr. ir. P. Sergeant
Proefschrift ingediend tot het behalen van de graad van
Doctor in de ingenieurswetenschappen: werktuigkunde-elektrotechniek

UNIVERSITEIT
GENT

Vakgroep Mechanica van Stroming, Warmte en Verbranding
Voorzitter: prof. dr. ir. J. Vierendeels
Faculteit Ingenieurswetenschappen en Architectuur
Academiejaar 2016 - 2017

ISBN 978-94-6355-016-1
NUR 959, 978
Wettelijk depot: D/2017/10.500/51

Promoter:

Prof. dr. ir. Jan Vierendeels
Prof. dr. ir. Peter Sergeant

Department:

Department of Flow, Heat and Combustion Mechanics (FloHeaCom)
Ghent University
Sint-Pietersnieuwstraat 41
B-9000 Gent, Belgium

Members of the exam committee:

Chairman:	
Prof. dr. ir. Patrick De Baets	Faculty of Engineering and Architecture, UGent
Secretary:	
Prof. dr. ir. Joris Degroote	Faculty of Engineering and Architecture, UGent
Reading committee:	
Prof. dr. ir. Vincent Lemort	Faculty of Applied Sciences, ULG
Prof. dr. ir. Pieter Rauwoens	Faculty of Engineering Technology, KULeuven
Dr. ir. Bernd Ameel	Faculty of Engineering and Architecture, UGent
Other members:	
Dr. ir. Hendrik Vansompel	Faculty of Engineering and Architecture, UGent
Prof. dr. ir. Joris Degroote	Faculty of Engineering and Architecture, UGent
Prof. dr. ir. Peter Sergeant	Faculty of Engineering and Architecture, UGent
Prof. dr. ir. Jan Vierendeels	Faculty of Engineering and Architecture, UGent

Acknowledgements

I wish to express my sincere appreciation to those who have contributed to this thesis and supported me in one way or the other during this amazing journey.

First of all, I am extremely grateful to my main supervisor, prof. Jan Vierendeels, for his guidance and all the useful discussions and brainstorming sessions. His deep insights helped me at various stages of my research. I really appreciate his willingness to meet me at short notice every time. My sincere gratitude is reserved for prof. Peter Sergeant for his invaluable insights and suggestions. I remain amazed that despite his busy schedule, he was able to go through several drafts of my papers at short notice every time. He is an inspiration. Moreover, I would like to acknowledge the Ghent University Association for their financial support through the FWO association research project G.0110.13.

Special thanks to Ahmed Hemeida for strong collaboration during these four years. Further, I would like to thank Dr. Hendrik Vansompel for preparing the experimental set-up and also for his technical advices in the course of the experiment.

I would also like to take this opportunity to thank Griet Blondé and Annie Harri for their administrative helps. A big "Thank you!" also goes out to Yves Maenhout for always being ready to help me with all kinds of computer problems.

Many thanks to my colleagues in Fluid mechanics group at Ghent University, in particular, Prof. Joris Degroote, Iva Papes, Gilberto Santo and Jolan Wauters. Thanks for being such a joy to work with.

I am very grateful to my officemates who always made a pleasant working environment, particularly, my good friend Akil Osman, and recently Lucas Delcour and Laurent De Moerloose deserve exceptional appreciation. Very special thanks to a very good friend Nicholas Agon for all the great moments in office or outside.

I would like to express my gratitude to my friends in Gent for providing support and friendship that I needed, in particular, Mohamed Eldib and Bardia. Your friendship is irreplaceable. My special gratitude also goes to my friends in The Netherlands, Amin Joneidi and Mehdi Sedighi.

Lastly, I would like to thank my parents Sakineh and Aliasghar for their unconditional love and supports. I love them so much, and I would not have made it this far without them. And I would also like to say a heartfelt thank you to my sisters Fatemeh, Neda and Mohadeseh for all their supports throughout the years.

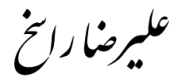

Alireza Rasekh
Gent, June 8, 2017

Summary

Disk type electrical machines such as axial flux permanent magnet synchronous machines (AFPMSM) are beneficial in electrical engineering applications that demand high power density, high efficiency, compact construction, and very strict geometrical constraints. In electrical vehicles, disk type motors with high efficiency can be used as "in-wheel" motor [1]. In hybrid electric vehicles, disk type motors can be - thanks to their short axial length - inserted between the internal combustion engine and the gear box [2]. In this thesis, the most common topology of an AFPMSM, i.e., the yokeless and segmented armature (YASA) is thoroughly investigated. These machines have two rotors and one stator [3, 4].

Overheating is one of the main issues in the electrical machines, which can tremendously degrade the lifetime and the performance of such devices. Therefore, a sophisticated thermal model is required to predict the adverse temperature rise within the materials in the machine. The main focus of this thesis is on the fundamental understanding of the heat transfer factors, including the rotational speed of the rotor, the air-gap size between rotor and stator, as well as the shape of the Permanent Magnets (PMs). Convection heat transfer is the main mechanism of heat transfer in this regard. Therefore, the goal is to find an effective, fast and robust model for assessing the heat transfer coefficients (HTC) for all the surfaces in the AFPMSM.

After the extensive survey of the relevant literature on the thermal modeling of AFPMSMs, the first part of this research is related to the accurate modeling of the heat transfer and fluid mechanics in the air-gap between the rotor and the stator disk. Thus, a simplified discoidal system is modeled through computational fluid dynamics (CFD). The objective is to find fast and robust formulations to estimate the convective heat transfer coefficients that account for various values of the rotational speed of the rotor as well as the air-gap distance. Contrary to the studies in the literature that considered the ambient temperature as the reference temperature to define the heat transfer coefficient, the average bulk fluid temperature adjacent to the corresponding surface is used in this work. By doing so, the proposed correlations are applicable for several working conditions, i.e., they are independent of the ambient temperature as well as the surface temperature of the rotor and the stator disk. In order to predict the average bulk fluid temperature, a linear correlation between the surface temperature of the rotor, the stator and the cover is made. The unknown coefficients of that

linear equation are found with the aid of the least squares method. Afterwards, the appropriate equations for the mean Nusselt number together with the average bulk temperature for all the surfaces are given through curve fittings. To check the validity of the proposed formulations, the results are compared with the available data in literature and good agreement has been found. It is shown that, for a given Reynolds number, there is a gap size ratio for which the average convective heat transfer of the stator surface in the gap reaches a minimum. Moreover, it can be concluded that the proposed correlation is a quite versatile tool for the thermal modeling of disk type electrical machines.

Having known the flow pattern and the heat transfer in the simple rotor-stator configuration, the next step is to find out the influence of the protrusions at the rotor, resembling the PMs, on the thermal performance of the rotor-stator arrangement in the YASA topology of the AFPMSM. The case-study here is composed of an open rotor-stator with sixteen magnets at the periphery of the rotor with an annular opening in the entire disk. Air can flow in a channel being formed between the magnets (air-channel) and in a small gap region between the magnets and the stator surface (air-gap). The idea is to use the space in between adjacent rotor magnets as cooling air-channels. The rotor disk with the magnets then behaves as a centrifugal fan causing efficient air gap cooling. To construct the correlations, CFD simulations are performed at the practical ranges of important non-dimensional parameters including the gap size ratio, the rotational Reynolds number, the magnet angle ratio and the magnet thickness ratio. Moreover, the Frozen Rotor (FR) approach is employed to simulate the rotary motion of the rotor together with the fluid around it. Likewise the simple rotor-stator system, it is crucial to make the correlations for the convective heat transfer coefficients independent of the ambient temperature and also surface temperatures. It is assumed that the reference temperature can be written as a linear correlation between the surface temperature of the rotor, the stator and the ambient temperature. To obtain the unknown coefficients of this linear formulation, a minimization algorithm is applied so long as the average bulk fluid temperature, used in the simple discoidal system, found to be no longer useful here. It is realized that the proposed correlations can strongly predict the convection heat transfer rates for all surfaces within the machine at the practical ranges of the magnet geometrical parameters and other significant factors. A more clear insight about the heat transfer in the rotor-stator system in this type of electrical machine is presented. It is demonstrated that the overall heat transfer improves significantly with an increase in the magnet thickness ratio, whereas the opposite trend is observed as the magnet angle ratio goes up. Moreover, the results reveal that the stator heat transfer in the gap reaches a maximum for a certain gap thickness.

Another issue that can be vital in the optimization of an AFPMSM is the windage power loss. In order to be able to perform an overall optimization

of such a machine, it is required to obtain fast equations to assess these losses. In similar manner to derive the equations for the convective heat transfer, a set of correlations for the windage power losses in an AFPMSM is presented. Two categories of formulations are defined to make the windage losses dimensionless based on whether the losses are mainly due to the viscous forces or the pressure forces. It is concluded that the pressure forces are responsible for the windage losses for the side surfaces in the air-channel, whereas for the surfaces facing the stator surface in the gap, the viscous forces mainly contribute to the windage losses. The parametric study is also undertaken to find the minimal value of the windage losses in line with the geometrical sizes of the magnets. The proposed correlations in this section along those obtained for the convective heat transfer coefficients can be very useful tools in the design and optimizations of this type of electrical machine.

The next part of this thesis focuses on the influence of the curved-shape PMs on the cooling air characteristics in the machine. As mentioned earlier, the rotor disks with magnets forms a radial air-channel. To exploit this effect further, the presence of the curved-shape magnets instead of the conventional PMs with the trapezoidal shape is investigated. CFD simulations are carried out to discover the thermal performance and the overall windage losses according to various curved-shape magnets. To this end, the conjugate heat transfer (CHT) analysis is undertaken to estimate the steady state surface temperature of the rotor and the stator in the full load of the machine. To get more insight about this problem, the experimental analysis is conducted in this research, as well. To that purpose, several dummy rotor disks with their distinctive curved-shape magnets are constructed. The results reveal that using the curved-shape magnet of ($\theta_1 = 2.5, \theta_2 = -2.5$) can be advantageous for the thermal purposes, whereas the designer should pay the penalty for the greatest windage losses. From an electromagnetical point of view a curved-shape magnet will also have an influence on certain design characteristics, such as the cogging torque (PhD thesis A. Hemeida [5]). As a result, defining an optimal shape of the magnet on the rotor disk represents a trade-off problem that should be solved by finding the compromise between these factors.

The last chapter of this dissertation presents an overview of the major findings and overall conclusion. Furthermore, final recommendations are made towards future research.

Samenvatting

Schijfvormige elektrische machines, zoals permanente-magneetbekrachtigde synchrone elektrische machines met axiale flux (AFPMSM) hebben gunstige eigenschappen voor elektrotechniektoepassingen waar een hoge vermogensdichtheid, hoge efficiëntie, compacte bouw vereist zijn en er bovendien zeer strenge geometrische beperkingen zijn. In elektrische voertuigen, kunnen schijfvormige motoren met een hoog rendement worden gebruikt als 'in-wheel"motor [1]. In hybride elektrische voertuigen kunnen schijfvormige motoren - dankzij hun korte axiale lengte – worden gemonteerd tussen de verbrandingsmotor en de versnellingsbak [2]. In dit proefschrift, wordt de meest voorkomende topologie van zulk een machine onderzocht, nl. met dubbele rotoruitvoering. Dergelijke machines worden ook "Yokeless and Segmented Armature" (YASA) machines genoemd. Deze machines hebben twee rotors en één stator [3, 4].

Oververhitting is een belangrijk aspect in elektrische machines, die de levensduur en de prestaties van dergelijke machines kunnen beïnvloeden. Daarom zijn geavanceerde thermische modellen nodig die de temperatuurstijging in de machine kunnen voorspellen. De focus van dit onderzoek is het fundamenteel begrip van de convectieve warmteoverdracht in deze machines en de invloed van operationele en designparameters zoals de rotatiesnelheid van de rotor, de grootte van de luchtspleet tussen de rotor en de stator en de vorm van de permanente magneet (PM). Het doel is om een snel en nauwkeurig model te bekomen voor de bepaling van de warmteoverdrachtscoëfficiënten van alle oppervlakken van de AFPMSM.

Na een literatuurstudie over de thermische modellering van AFPMSMs, is het eerste deel van dit onderzoek gewijt aan een nauwkeurige modellering van de warmteoverdracht en stromingsmechanica in de luchtspleet tussen de rotor en de stator schijf. Een vereenvoudigd discoïdaal systeem met platte rotor en stator wordt geanalyseerd door middel van numerieke stromingssimulaties (CFD). Het doel is om snelle en nauwkeurige correlaties voor de convectiecoëfficiënten te vinden als functie van de rotatiesnelheid van de rotor en de luchtspleetafstand tussen de rotor en de stator. Verschillend van de studies in de literatuur die de omgevingstemperatuur als referentietemperatuur gebruiken om de convectiecoëfficiënt te bepalen, wordt de gemiddelde bulktemperatuur naast het betreffende oppervlak gebruikt in dit werk. Hierdoor zijn de voorgestelde correlaties toepasbaar voor verschillende werkomstandigheden, d.w.z. ze worden op die manier onafhan-

kelijk van de omgevingstemperatuur en de oppervlaktetemperatuur van de rotor en de stator. Om de gemiddelde bulktemperatuur voorspellen, wordt een eenvoudige lineaire correlatie tussen de oppervlaktetemperatuur van de rotor, de stator en de behuizing gemaakt. De onbekende coëfficiënten van die lineaire vergelijking worden gevonden met behulp van de kleinstekwadratenmethode. Daarna worden de vergelijkingen voor het gemiddelde Nusseltgetal en de gemiddelde bulktemperatuur van alle oppervlakken gegeven door curve fitting. Om de geldigheid van de voorgestelde formuleringen te controleren, worden de resultaten vergeleken met beschikbare gegevens uit de literatuur en een goede overeenstemming werd gevonden. Er wordt aangetoond dat voor een gegeven Reynoldsgetal er een luchtspleetafstand is waarvoor de gemiddelde convectieve warmteoverdracht van het statoroppervlak in de spleet een minimum bereikt. Verder kan worden geconcludeerd dat de voorgestelde correlatie een bruikbare tool is voor de thermische modellering van schijfvormige elektrische machines.

Met de kennis van het stromingspatroon en de warmteoverdracht in de eenvoudige rotor-stator configuratie, is de volgende stap het analyseren van de invloed van typische vormen van permanente magneten op de rotor op de thermische prestaties van de rotor-stator configuratie van de AFPMSM. De topologie die hier wordt onderzocht bestaat uit een open rotor-stator met zestien magneten op de omtrek van de rotor en met een ringvormige opening tussen de as en de magneten zodat lucht kan aangezogen worden. Lucht kan aldus stromen in een kanaal gevormd tussen de magneten (luchtkanaal) en een kleine luchtspleet tussen de magneten en het statoroppervlak. De rotorschijf met de magneten gedraagt zich dan als een soort centrifugale ventilator met efficiëntere luchtspleetkoeling. Om correlaties te construeren worden CFD simulaties uitgevoerd over een praktisch bereik van belangrijke dimensieloze parameters zoals de luchtspleetratio, het rotatie-Reynoldsgetal, de magneethoekverhouding en de magneetdikteverhouding. De 'Frozen Rotor' (FR) techniek wordt toegepast om het draaieffect van de rotor in rekening te brengen. Zoals in het vereenvoudigd discoïdaal systeem met platte rotor en stator is het noodzakelijk om de correlaties voor de convectiewarmteoverdrachtcoëfficiënten onafhankelijk van de omgevingstemperatuur maken en ook oppervlaktetemperaturen. Aangenomen wordt dat de referentietemperatuur kan benaderd worden door een lineair verband tussen de oppervlaktetemperatuur van de rotor en de stator en de omgevingstemperatuur. Om de onbekende coëfficiënten van dit lineair verband te verkrijgen, wordt een minimalisatie-algoritme toegepast aangezien de werkwijze met de gemiddelde bulktemperatuur, die voor het eenvoudig discoïdaal systeem gebruikt werd, hier niet meer bruikbaar bleek te zijn. De voorgestelde correlaties blijken zeer goed de convectieve warmteoverdracht te voorspellen van alle oppervlakken in de machine in het praktische bereik van de geometrische parameters en andere belangrijke operationele parameters. Een duidelijker inzicht werd ook bekomen in de warmteoverdracht van het rotor-stator systeem in een dergelijke elektrische machine. Er is

aangetoond dat de totale warmteoverdracht aanzienlijk verbeterd met een toename van de dikteverhouding van de magneten, terwijl det tegenovergestelde trend werd waargenomen als de hoekverhouding van de magneten stijgt. Bovendien laten de resultaten zien dat de warmteoverdracht van de stator in de spleet een maximum bereikt voor een bepaalde dikte van de spleet.

Een andere invloed die van belang is in de optimalisatie van een AFPMSM, is het vermogensverlies door de luchtcirkulatie. Om een globale optimalisatie van zo'n machine mogelijk te maken, is het nodig om snelle correlaties te bekomen om deze verliezen te beoordelen. Op gelijkaardige manier als werd gedaan voor de correlaties voor de convectieve warmteoverdracht, worden een reeks correlaties voor het vermogensverlies door luchtcirkulatie in een AFPMSM voorgesteld. Twee soorten dimensieloze formuleringen worden gedefinieerd afhankelijk van het feit of de verliezen voornamelijk te wijten zijn aan viskeuze krachten of aan drukkrachten. Geconcludeerd wordt dat de drukkrachten verantwoordelijk zijn voor de verliezen voor de zijvlakken in het luchtkanaal, terwijl voor de oppervlakken parallel aan het statoroppervlak in de spleet, uiteraard enkel de viskeuze krachten bijdragen aan de verliezen. Een parametrische studie werd ook uitgevoerd om de invloed van geometrische afmetingen van de magneten op deze verliezen te kunnen begroten. De voorgestelde correlaties in dit gedeelte zijn net als die voor de convectiecoëfficiënten nodige input voor een globaal ontwerp en optimalisatie van een dergelijke elektrische machine.

Het volgende deel van de thesis richt zich op de invloed van een gekromde vorm van de permanente magneten op de koelingseigenschappen in de machine. Zoals eerder vermeld, vormt een conventionele rotorschijf met magneten een radiaal luchtkanaal. In dit gedeelte wordt de invloed van een gekromde vorm van de permanente magneten onderzocht. CFD simulaties worden uitgevoerd om de thermische prestaties en de luchtcirkulatieverliezen voor diverse gebogen vormen van de magneten te begroten. Hiertoe wordt een analyse met gekoppelde warmteoverdracht in het materiaal en in de lucht gebruikt om de stationaire oppervlaktetemperatuur van de rotor en de stator in vollast van de machine te bekomen. Om meer inzicht te krijgen over dit probleem, wordt ook een experimentele analyse uitgevoerd. Daartoe worden verschillende rotorschijven met dummy magneten met gekromde vorm geconstrueerd. Uit de resultaten blijkt dat het gebruik van de gekromde vorm van de magneet ($\theta_1 = 2.5, \theta_2 = -2.5$) het meest gunstig voor de koeling is, terwijl deze keuze wel de grootste luchtcirkulatieverliezen geeft. Uit elektromagnetisch standpunt heeft een gekromde vorm van de permanente magneten ook een invloed op design parameters zoals bv. het 'cogging' koppel (Phd thesis A. Hemeida [5]). Bijgevolg is de bepaling van een optimale vorm van de magneet op de rotorschijf het vinden van een compromis tussen deze factoren.

In het laatste hoofdstuk van dit proefschrift wordt een overzicht gegeven van de belangrijkste bevindingen en de algemene conclusie. Verder werden

aanbevelingen gedaan voor toekomstig onderzoek.

Table of Contents

Nomenclature

Abbreviations

2-D	Two dimensional
3-D	Three dimensional
AFPMSM	Axial Flux Permanent Magnet Synchronous Machine
CFD	Computational Fluid Dynamics
DNS	Direct Numerical Simulation
FE	Finite Element
FEM	Finite Element Methodology
FR	Frozen Rotor
HTC	Heat Transfer Coefficient
IR	Infra-red
LES	Large Eddy Simulation
LP	Lumped Parameter
MRF	Multiple Reference Frame
PM	Permanent Magnet
RANS	Reynolds-Averaged Navier Stokes
SAT	Segmented armature torus
SM	Sliding Mesh
SVV	Spectral Vanishing Viscosity
UDF	User-defined Function
YASA	Yokeless and Segmented Armature

Roman symbols

a	Coefficient in Eqs. 3.6-4.6	-
b	Coefficient in Eqs. 3.6-4.6	-
Bi	Biot number	-
C	Sutherland constant	-
c_p	Specific heat capacity	J/(kg.K)
C_w	Non-dimensional flow rate	-
G	Gap size ratio	-
h	Heat transfer coefficient	W/(m^2.K)

$\overline{h}$	Mean heat transfer coefficient	W/(m^2.K)
h_f	specific enthalpy	J/kg
I	Electric current	A
k	Thermal conductivity	W/(m.K)
k_t	Turbulent thermal conductivity	W/(m.K)
L	Magnet angle ratio	-
$\dot{m}$	Mass flow rate	kg/s
n	Number of temperature combinations	-
Nu	Nusselt number	-
$\overline{Nu}$	Mean Nusselt number	-
p	Pressure	Pa
P	Windage power losses	W
$P^{'}$	Non-dimensional Windage power losses	-
$P^{'}_{\rho}$	Non-dimensional windage losses due to pressure forces	-
$P^{'}_{\nu}$	Non-dimensional windage losses due to viscous forces	-
Pr	Prandtl number	-
Q	Volumetric flow rate	m^3/s
$\dot{Q}$	Convective heat transfer rate	W
$\overline{q}$	Average heat flux	W/m^2
R	Electrical resistance	Ω
R	Radius of the disks	m
$\overline{R}$	Specific gas constant	J/(kg.K)
Re	Rotational Reynolds number	-
Re_j	Jet Rotational Reynolds number	-
Re_s	Gap Rotational Reynolds number	-
s	Gap size	m
t	Time	s
t	Magnet thickness	m
T	Temperature	°C
T_{ad}	Adiabatic temperature	°C
T_q	Torque on the rotor disk	N.m
Ta	Taylor number	-
U	Radial velocity	m/s
V	Axial velocity	m/s
V	volume	m^3
v	Tip velocity of the magnet	m/s
$\overrightarrow{v_r}$	relative velocity with respect to the rotating frame	m/s
$\overrightarrow{v}$	absolute velocity in the stationary frame	m/s
W	Tangential velocity	m/s
X_0	Parameter in Eq.2.5	-

Greek symbols

α	Magnet angle	$^\circ$
α_m	Magnet angle ratio	-
μ	Dynamic viscosity	kg/(m.s)
μ_t	Turbulent viscosity	kg/(m.s)
ν	kinematic viscosity	m^2/s
ρ	Density	kg/m^3
σ	Standard deviation	-
ω	Rotational speed of the rotor	rad/s
$\overrightarrow{\Omega}$	Rotational velocity vector of the rotating domain	rad/s
ℓ_f	Length scale	m

Subscripts

atm	Atmospheric
amb	Ambient
C	Cover
f	Surface that heat flux being measured
R	Rotor
rad	Radiation
ref	Reference
sur	Surface
S	Stator
∞	Free stream

Superscripts

$*$	Values at the reference point

1 Introduction

1.1 Background

Electrical machines are devices which convert mechanical energy into electrical energy or vice versa. These machines consume more than half of the global electricity produced and this trend is ever increasing [6]. They are quite common in the modern societies with their extensive applicability such as in power stations, fans, mixers in food industry, blowers and pumps, hybrid electric vehicles and so forth. More importantly, electrical machines have been commonly used in the wind turbine industry as the major source of the clean and sustainable energy. Thus, any improvement in the electrical machines can substantially impact the renewable energy development. In this way, society would find an alternative for the fossil fuels and solve some main issues like the climate change and the shortage of the energy resources. Besides that, electrical machines are environment-friendly, clean, rather cheap and very efficient. Therefore, these can be the answers to the question "Why are electric machines so ubiquitous in modern daily life?".

After the invention of the electrical machines in mid 19th century - thanks to the dedicated scientists Michael Faraday, Nikola Tesla and other pioneer researchers - the emergence of the permanent magnets (PM) at 1980s has revolutionized the design of rotating electrical machines. To make PM machines commercially viable, optimizations with the aid of computer simulation have been performed in the past few decades. This has resulted in the electromagnetic behavior of PM machines becoming very

well-understood. In contrast to this, less attention has been paid to the thermal study of the electrical machines.

The design of the cooling system in the electrical machines is of equal importance as the electromagnetic design of the machine, inasmuch as the temperature rise of the machine determines the maximum allowable output power [6]. In addition to that, the accurate management of heat transfer becomes more significant in the modern electrical machines such as an axial flux permanent magnet synchronous machine (AFPMSM) due to the compact construction, and very strict geometrical constraints.

In this research, the goal is to provide a comprehensive knowledge of the fluid mechanics and more in-depth insight into the convective heat transfer in an AFPMSM. The idea is to present a more systematic approach such as defining scaling laws for the geometry, i.e., a set of correlations to determine the thermal and fluid mechanics aspects according to the governing geometrical and physical parameters of such a machine.

1.2 Axial Flux Permanent Magnet Synchronous Machine

There are several ways to classify the electrical machines. In line with the direction of the magnetic field, for instance, there are three distinct categories of the electrical machines, namely the transversal flux, the radial flux and the axial flux electrical machines. The latter, which is the subject of this research, directs the magnetic field axially across the air-gap between the rotor and the stator (see Fig. 1.1).

The basic operation principle of an AFPMSM is similar to the one of radial flux PM machines. The PMs, which are mounted on the surface of the rotor, produce a magnetic field. As adjacent permanent magnets are alternately magnetized, they generate a pulsating magnetic field that crosses the air-gap to the stator and returns back again to the rotor in a stationary mode. When an external force rotates the rotor disc with respect to the stator, a time varying magnetic flux is generated in the stator teeth. The time variation in the magnetic flux induces a back electromotive force (EMF) in the stator windings. This back EMF produces a current in the connected load. In this case, the AFPMSM acts as a generator. In motor mode, an external imposed current leads to a magnetic field that interacts with the one produced by the PMs and results in a rotation of the rotor. In this case electric power is transferred into mechanical power, available at the shaft of the machine. [5]

In contrast to the radial electrical machines, the axial flux permanent magnet machines have the following advantages [7]:

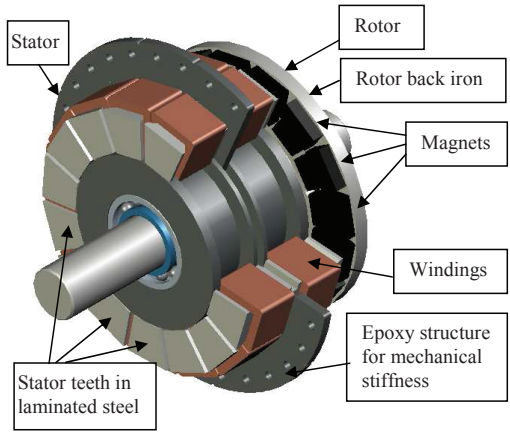

Figure 1.1: AFPMSM with two rotors on both sides of the stator (front rotor removed for clarity) [7].

- AFPMSMs have a compact design construction and usually take less space than the radial machines. Thus, they are very suitable for the applications where the axial length of the machine is limited.

- They have a high energy efficiency (about 95 %) as well as an excellent power density. Chen et al. [8] performed a comparative study between different types of radial and axial flux machine for wind turbine applications. They demonstrated that at the power levels ranging from 1 kW to 200 kW, the axial flux machines have a smaller volume for a given power rating, making the power density very high as compared to the radial flux machine.

1.3 Yokeless And Segmented Armature Topology

There exist several topologies of AFPMSMs. In this research, a yokeless and segmented armature (YASA) is taken into consideration. The YASA topology, which is sometimes called the segmented armature torus (SAT), is the common variant of the stator-rotor arrangement in the AFPMSM, shown in Fig. 1.2. This topology is made of a single stator placed between the two rotor disks. The paths of the magnetic flux in the YASA topology of the AFPMSM is indicated in Fig. 1.3.

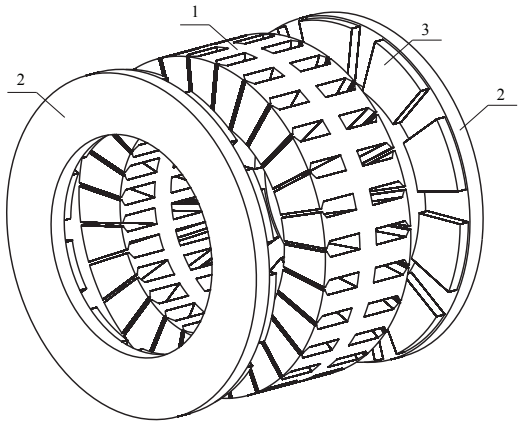

Figure 1.2: Schematic diagram of the YASA topology of an AFPMSM. 1) Stator, 2) rotor, 3) permanent magnet [7].

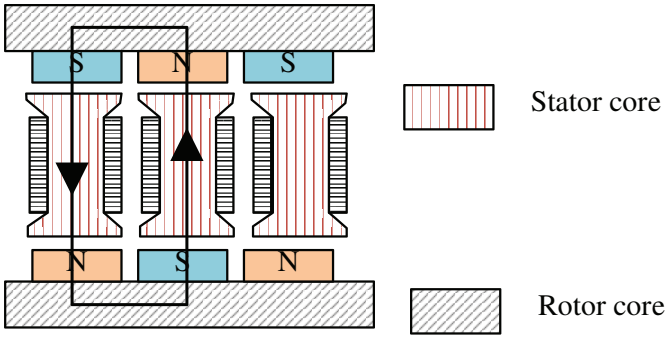

Figure 1.3: Schematic representation of the path of magnetic flux in YASA machine [5].

1.4 Applications of AFPMSMs

AFPMSMs are being used in various applications in recent years. Some examples of the main existing applications of these machines are listed below along with the machine operating speed:

- **Electric and hybrid vehicles**: Lamperth et al. [9] used an AFPMSM for heavy-duty hybrid and electric vehicle applications with the power density of 1.8 kW/kg and the efficiency up to 96 % at 3600 rpm.
- **High-speed generator driven by a gas turbine**: Pullen et al. [10] investigated the application of a multi-disk AFPMSM in a high

speed portable gas turbine for 10, 30, 50 kW at 60,000 rpm.

- **Renewable energy**: Bumby and Martin [11] designed an AFPMSM for a vertical axis wind turbine. Their prototype was capable of producing 1 kW at 300 rpm and 2 kW at 500 rpm.
- **Pumps**: Caricchi et al. [12] used an AFPMSM in a pump with the power of 880 W at 2800 rpm.

1.5 Thermal issue in AFPMSMs

Likewise all kinds of electrical machines, the generated losses in an AFPMSM manifest themselves as the production of heat. This leads to an adverse temperature rise within the materials, which is detrimental to the performance of the machine and causes overheating. In fact, the overheating of the machine brings about some problems such as:

- Demagnetization occurs in the magnet as the temperature exceeds the critical value (e.g. $T_c = 150°\text{C}$ for SH type NdFeB magnets) [7].
- The resistivity of the copper winding in the stator goes up with temperature (about 0.4%/K) and it negatively affects the efficiency of the machine [13].
- The designer should provide excessive cooling through the external fan, resulting in an extra energy consumption, which in turn decreases the energy efficiency.
- The excessive heat could reduce the lifetime of the insulation materials in the stator winding.

Apart from the above mentioned drawbacks, different individual losses terms (copper loss, iron loss, losses in magnets, windage loss and etc) in the machine are always a function of temperature. This means that the surface temperature distribution should be known in order to compute the machine's efficiency accurately. This requires an accurate and reliable thermal model of AFPMSMs. This model needs to be capable of predicting the required cooling to maintain both a long life time and a high reliability of such machines.

The cooling of the AFPMSM can be achieved either by water or air. The usage of water has some advantages. As the thermal capacity of water is greater than air, water cooling can be more compact. However, possible water leakage presents an unacceptable safety risk. Therefore, the provision of cooling by air is much more convenient and useful, and therefore it is the subject of this research.

1.6 Research goals

In order to design the AFPMSM, the objective function should be defined in such a way to maximize the energy efficiency and the power density. This means the losses in the machine, e.g., the electromagnetic losses and the windage losses needs to be minimized. In general, these losses manifest themselves as the production of heat. The operating temperature of an electrical machine can be controlled by balancing between heat generated and heat removal rate. Controlling the machine operating temperature is crucial, in order to avoid overheating which was discussed in the preceding section. This means the maximum attainable temperature in the machine is a design constraint that limits the power density. As a consequence, it is imperative to have a sophisticated thermal model to predict the surface temperature in such a machine.

Since the losses in the machine are usually temperature dependent, a fully coupled model for thermal and electromagnetic analysis is required, allowing complex optimizations to be undertaken. The main purpose of this thesis is to formulate the convective heat transfer coefficients in the AFPMSMs. These correlations are used as an input to the coupled model developed by Hendrik Vansompel [14], and also to a lumped parameter model in the PhD thesis of A. Hemeida [5].

As a result, the current research aims to address the following objectives:

- Firstly, the overall understanding of the convective heat transfer in a simple rotor-stator system is studied. This can provide a clear view about the air-gap convection in the real machine. A thermal model is presented, to predict the convective heat transfer coefficients for surfaces in the air-gap, as a function of the rotational speed of the rotor, disk diameter as well as the air-gap size. The reference temperature should be chosen in such a way that the correlations for the heat transfer coefficients become generally applicable.

- Secondly, the impact of the presence of the PMs on the convective heat transfer is investigated. The objective is to construct a set of correlations for the convective heat transfer coefficients, as a function of various various physical and geometrical parameters, including the magnet angle, magnet thickness as well as the gap size, the rotational speed of the rotor and the surface temperatures.

- Similar to the convective heat transfer coefficients modeling, a set of correlations for the prediction of windage power losses in the current AFPMSM will be developed. These fast and robust formulations will facilitate the optimization of the machine.

- At last, the influence of the curved-shape magnets at the rotor disk on the performance of the AFPMSM is investigated. The goals are to predict the impact of using curved magnets on the rotor and stator temperatures and to validate the accuracy of the prediction with experimental results.

1.7 Outline

Aside from this introductory chapter, the structure of this thesis consists of the following parts:

- Overview of the scientific literature
- Flow and heat transfer in a simple discoidal configuration
- Convective heat transfer modeling in an AFPMSM
- Windage power losses modeling in an AFPMSM
- Effects of the curved-shape magnets on the performance of an AFPMSM
- Overall conclusions and future perspectives

Chapter 2 provides a concise overview of the literature for the thermal aspects of the disk-type electrical machines. The state-of-the-art research for the thermal modeling in the AFPMSMs is explained in detail.

Chapter 3 deals with the CFD simulation of a simple rotor-stator system enclosed in a cylindrical cover. The different types of the flow patterns occurring inside the air-gap between the rotor and stator are classified. Moreover, the parametrized correlations to fully predict the convective heat transfer for all surfaces within this system are presented, according to different values of the gap size ratio and the rotational Reynolds number. The reference temperature is defined in such a way that the predicted convective heat transfer coefficients become approximately independent of the surface temperatures. The application of these correlations in the coupled electromagnetic and thermal study of an AFPMSM is also discussed. To achieve this, a strong collaboration with a doctoral dissertation done by A. Hemeida [5] has been established.

Chapter 4 presents formulations to assess the average convective heat transfer in an AFPMSM. CFD simulations are performed for an open rotor-stator system considering the essence of the magnets on the rotor disk. A minimization algorithm is employed to assess the reference temperature instead of using either the average bulk fluid temperature or the ambient

temperature. The effect of the magnet geometrical parameters on the overall heat transfer within this configuration, especially at the stator disk of the machine are presented.

Chapter 5 introduces a set of correlations for the windage power losses in an AFPMSM, based on the CFD simulations. Two categories of formulations are defined to make the windage losses dimensionless, based on whether the losses are mainly due to the viscous forces or the pressure forces. Also, the overall windage losses in the machine are calculated according to the geometrical parameters of the magnets.

Chapter 6 discusses the influence of the curved-shape magnets on the thermal performance and windage losses in the machine. To that end, CFD simulations along with an experimental analysis are undertaken.

Chapter 7 concludes this research and provides some thoughts and recommendations for future perspective of the efficient cooling system and thermal performance of an AFPMSM.

1.8 Publications covering this work

1.8.1 Peer-reviewed publications

- A. Rasekh, P. Sergeant, and J. Vierendeels. Convective heat transfer prediction in disk-type electrical machines. *Applied Thermal Engineering*, 91:778–790, 2015
- H. Vansompel, A. Rasekh, A. Hemeida, J. Vierendeels, and P. Sergeant. Coupled electromagnetic and thermal analysis of an axial flux PM machine. *IEEE Transactions on Magnets*, 51(11):8108104, 2015
- A. Rasekh, P. Sergeant, and J. Vierendeels. Development of correlations for windage power losses modeling in an axial flux permanent magnet synchronous machine with geometrical features of the magnets. *Energies*, 9, 1009:doi:10.3390/en9121009, 2016
- A. Rasekh, P. Sergeant, and J. Vierendeels. Fully predictive heat transfer coefficient modeling of an axial flux permanent magnet synchronous machine with geometrical parameters of the magnets. *Applied Thermal Engineering*, 110:1343–1357, 2017
- A. Rasekh, P. Sergeant, and J. Vierendeels. CFD-parametric study in stator heat transfer of an axial flux permanent magnet machine. *International Journal of Mechanical, Aerospace, Industrial, Mechatronic and Manufacturing Engineering*, 11(1):61–65, 2017
- A. Rasekh, A. Hemeida, H. Vansompel, P. Sergeant, and J. Vierendeels. Influence of the curved-shape magnets on the performance of an axial flux permanent magnet synchronous machine. *To be submitted*

1.8.2 Conference Proceedings

- A. Rasekh, P. Sergeant, and J. Vierendeels. Heat transfer study in an enclosed rotor-stator system. *6th International Conference on Advanced Computational Methods in Engineering (ACOMEN), Ghent*, 2014
- A. Rasekh, P. Sergeant, and J. Vierendeels. a parametric-CFD study for heat transfer and fluid flow in a rotor-stator system. *11th World Congress on Computational Mechanics (WCCM XI), Barcelona*, pages 4475–4483, 2014
- A. Rasekh, P. Sergeant, and J. Vierendeels. A study of convective heat transfer in a rotor-stator system of disk-type electrical machines. *11th International Conference on Heat Transfer, Fluid Mechanics and Thermodynamics (HEFAT), South Africa*, pages 487–492, 2015

- A. Rasekh, P. Sergeant, and J. Vierendeels. Stator heat transfer prediction of disk-type electrical machines. *Proceedings of the 1st Thermal and Fluid Engineering Summer Conference, (TFESC), New York*, pages 1–10, 2015

- A. Hemeida, P. Sergeant, A. Rasekh, and J. Vierendeels. An optimal design of a 5MW AFPMSM for wind turbine applications using analytical model. *XXII International Conference on Electrical Machines (ICEM), Switzerland*, pages 1290–1297, 2016

- A. Rasekh, P. Sergeant, and J. Vierendeels. Computational fluid dynamics (CFD)-parametric study in stator heat transfer of an Axial Flux Permanent Magnet Machine. *19th International Conference on Heat Transfer and Applications (ICHTA), London*, 2017

2 Literature review

2.1 Introduction

This chapter presents an overview of studies undertaken on thermal aspects of the disk-type electrical machines. The different approaches for the thermal analysis of AFPMSMs, namely numerical models, experimental techniques and lumped parameter methods are elaborately explained. Moreover, the previous work on the windage power losses modeling in this type of electrical machine is discussed. Since the air-gap convection plays an important role in cooling of AFPMSMs, a detailed review of preceding studies on the flow and heat transfer characteristics in rotor-stator systems are also described in more detail.

2.2 Thermal modeling of AFPMSMs

The aim of the thermal modeling is to predict the temperature distribution within the machine. To achieve this, distinct ways have been used in the literature including:

- Numerical modeling
- Experimental analysis
- Lumped parameter method

The state-of-the-art research in each of the aforementioned parts will be discussed in detail in the following sections.

2.2.1 Numerical modeling

Over the past decade, the numerical modeling including computational fluid dynamics (CFD) and finite element (FE) analysis are being increasingly applied to investigate the thermal design of electrical machines [26–31]. In this sense, Huai et al. [32] accurately predicted the temperature rise in an electric induction motor using the FE methodology. They showed that the highest temperature occurs in the end winding area (about 100°C) and found good correspondence between numerically predicted and experimentally measured temperature in this region.

Marignetti et al. [33] developed a FE method to simulate the flow in the air-gap of an AFPMSM. Only the air flow confined in the gap region was taken into consideration, and empirical equations for convective heat transfer towards the environment for the outer surfaces have been used in order to expedite the proposed thermal model. In another paper by Marignetti and his colleague [34], an axisymmetric 2-D model with a swirl-flow formulation was used to model the airflow inside an AFPMSM. It was indicated that the FE results for the rotor temperature is lower than the measured value as the influence of slot harmonics was neglected in the simulations.

Airoldi et al. [35, 36] performed CFD simulations of all the rig components and the air inside it in an AFPMSM. There were six magnets on the rotor disk and due to system periodicity only one complete magnet was modeled. The Multiple Reference Frame (MRF) method has been used to consider the rotation of the generator's components and the cooling air. They also used the realizable $k-\epsilon$ turbulent model. It was shown that there exists a significant region of reversed flow inside the running clearance which reduces the peak temperature on the stator disk.

Seghir-Oualil et al. [37] investigated the thermal behaviour of a synchronous motor with permanent magnets using CFD simulations along with a lumped parameter method. Three different cooling solutions were introduced. Firstly, in order to decrease the magnet temperature in a significant way, the interior of the rotor was equipped with longitudinal fins. Secondly, the use of an auxiliary pipe into the rotor operating as a heat exchanger was found to maintain the magnet temperature far from the critical temperature. Finally, the utilization of thermal bridges for the end-winding cooling could improve the heat transfers and this lowered the end-winding temperature. The authors suggested that the implementation of these cooling solutions limits the temperatures of the whole machine far below the

critical values.

Kolondzovski et al. [38] presented a new approach for thermal design of a high-speed permanent magnet (PM) machine. A numerical-multiphysics method was used which coupled computational fluid dynamics and heat transfer equations. The flow and temperature field of the cooling fluid were simulated using COMSOL Multiphysics software in a 2-D axisymmetric domain. On the other hand, the temperature distribution in the solid domain of the machine was estimated with a 3-D finite element thermal model. The temperature and flow field information from the 2-D method were used to define boundary conditions for the 3-D thermal model. They reported that the proposed technique allows a rough estimation of the local temperature distribution with a minimum amount of computational resources.

Chon et al. [39, 40] developed CFD methods for a NGenTec axial flux permanent magnet prototype generator operating at 100 rpm to understand the thermal performance of the machine. Their CFD model consisted of multiple solid and fluid regions comprising the coils, epoxy, fins, permanent magnets, rotor and air. The MRF approach was used to model the motion of the rotor for time-averaged steady-state flow and conjugate heat transfer. The energy losses in the stator were the inputs for CFD thermal modeling since they were dissipated as heat. It was perceived that convective heat transfer dominates the cooling process in the generator because of the strong air motion through the machine when the rotor is rotating.

Sarrafan and Darabi [41] estimated the steady state temperature distribution in an AFPMSM using FE method. The cooling system consisted of heat pipes with water as the working fluid. They showed that the stator core temperature reaches up to 135°C, while the rotor core temperature could be around 80°C.

Kahourzade et al. [42] undertook the CFD simulation of an AFPMSM and discovered that the heat generated in the windings transfers to the stator through conduction and is then conducted to the motor's body where the body surface cools down by the ambient air. As shown in Fig. 2.1, the difference between the coolest and the hottest spot on the stator surface is approximately 12°C, while it is about 4°C for the rotor disk. Furthermore, the maximum temperature of 87°C took place in stator areas, in particular, adjacent to the winding coils.

Another numerical study on the air-cooled disk-type electrical generator has been carried out by Moradnia and his colleagues [43–45]. They have used two numerical approaches, a fully predictive approach in which the flow is simulated independently of the experimental results, and another approach with inlet and outlet boundary conditions, specified from the experimental data. It was concluded that a fully predictive simulation gives

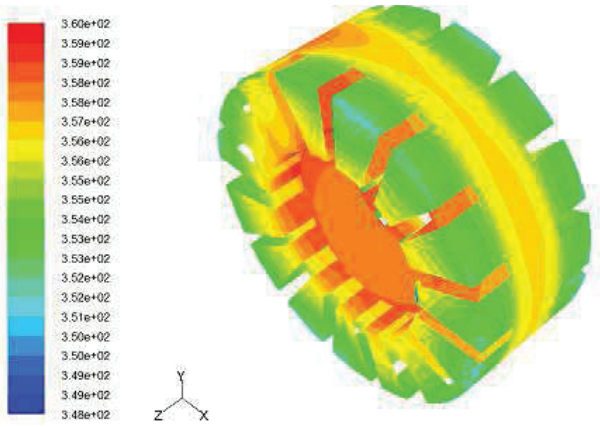

(a)

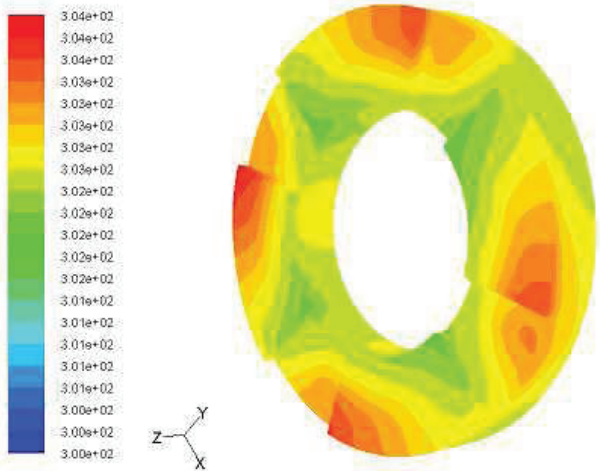

(b)

Figure 2.1: Temperature (K) contour for both rotor and stator of the motor representing the thermal distribution (a) Stator (b) Rotor [42].

more accurate results for the pressure coefficients at the stator cooling channel. The comparison between different pole and stator geometries indicated that the addition of stator baffles helps to increase the volume flow in the generator and removes the outward velocities at the inlet.

Recently, Polikarpova et al. [46] examined the influence of potting of the stator on the thermal behavior of an axial-flux generator with one-rotor-two-stator topology. A liquid cooling system has been applied on the

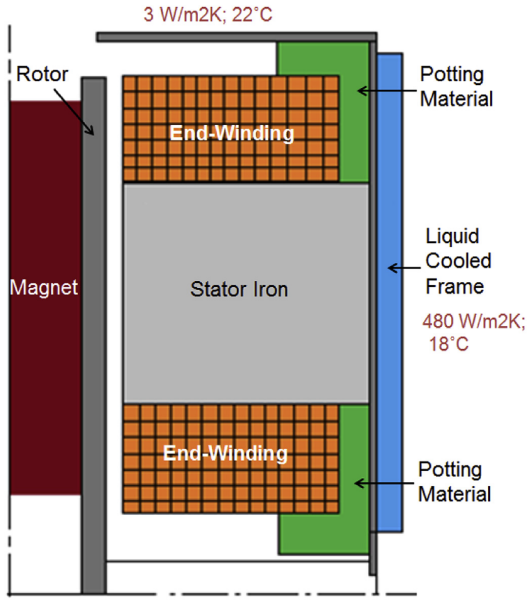

Figure 2.2: Indirect stator cooling system [46].

stator frame, and the potting material in the end-winding region is thermally connected the end winding to the housing heat sink, as illustrated in Fig. 2.2. Simplified thermal models based on CFD were used to analyze the temperature distribution through the machine. The volumetric heat losses, shown in Table 2.1, were utilized as the input data for the 3-D CFD model. The temperature results of the simulation for 75% load is listed in Table 2.2. They reported that the calculated temperatures of the machine with the proposed cooling solution are below the thermal constraints of the magnets and the winding insulation, and therefore, provide reliable and long-term operation.

Table 2.1: Heat losses generated within the machine parts at 75% load [46].

Machine Part	Heat losses (W)	Volumetric heat losses (kW/m^3)
Stator iron	675	196
Copper winding	1114	230
Rotor iron	150	168
Permanent magnet	225	273

Table 2.2: Calculated temperatures at 75% load [46].

Machine Part	75% load nonpotted stator temperature (°C)	75% load potted stator temperature (°C)
End winding air gap side	136	132
End winding, frame side	136	132
Slot winding	138	135
Air gap	120	115
Stator iron	120	110
Rotor iron (laminate)	103	95
Rotor magnets	103	95

2.2.2 Experimental analysis

In order to apply the numerical models for the thermal analysis in AFPMSMs with reliability and confidence, it is necessary to carry out an experimental validation. The AFPMSMs have compact construction that demand very strict geometrical constraints. This not only results in the experimental study becoming very expensive, but it also becomes extremely difficult to construct the set-up test itself. For this reason, the number of experiments on the thermal performance assessment of the AFPMSMs are very limited.

Nevertheless, Wang et al. [47, 48] constructed a prototype of an AFPMSM. The machine was set up with a discharge duct. Along one side of the duct, several tapping points were made for evaluating the static pressure with a manometer. Near the outlet of the duct, a provision was made whereby the velocity was measured using a hot-wire anemometer probe. The static pressure difference $\triangle p$ was measured as a function of volumetric flow rate ($Q = Av$) for different motor speeds varying from 200 to 1400 rpm.

Scowby et al. [49] experimentally evaluated the thermal performance of an AFPMSM. The prototype, which is shown in Fig. 2.3, has a diameter of 860 mm, an axial width of 105 mm and a power rating of 300 kW at 2300 rpm, operating at an energy efficiency of 95%. They showed that the theoretically predicted pressure and mass flow rates agree well with measured values. They reported that the rotor hub's straight blades determine the flow rate through the machine and also result in relatively large energy losses.

Lim et al. [50] conducted an experiment to assess the convective heat transfer coefficients in an AFPM generator (1.5 kW & 1500 rpm) at the range of rotational Reynolds number ($Re = \frac{\omega R^2}{\nu}$) from 0 to 2×10^6 and

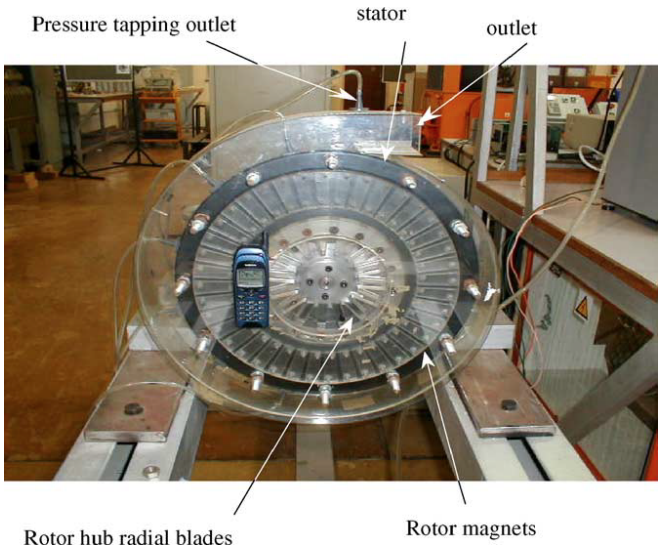

Figure 2.3: Transparent model of the AFPMSM [49].

the non-dimensional flow rate ($C_w = \frac{Q}{\nu R}$) of 0 to 11000 where the gap size ratio ($G = \frac{G}{R}$) was kept fixed at 0.016. The measured data showed a linear dependency between the non-dimensional flow rate with the rotor rotational speed. CFD simulations were also performed. It has been shown that by overlooking the effect of the natural convection, the CFD model under-predicts the surface heat transfer coefficients on the stator disk. In fact, due to the large size of the scaled-up rig, natural convection played a significant part in the heat transfer and this had to be compensated for in the forced convection heat transfer coefficient calculations.

Camilleri et al. [51] experimentally investigated the heat transfer coefficient (HTC) in an oil-cooled electrical machine with a segmented stator using double layered heat flux gauges. The Seider-Tate equation for the laminar flow in a short pipe was used to compare with their experimental results:

$$Nu = 1.86(Pr.Re)^{0.33}(D_h)^{0.33}(\frac{\mu_b}{\mu_w})^{0.14} \tag{2.1}$$

where μ_b & μ_w represent the fluid viscosity at the bulk temperature and the wall temperature, respectively. They concluded that the existing laminar correlations i.e. the Seider-Tate correlation for the laminar flow in a short pipe under-predicts the values of the heat transfer coefficient when applied to the settings of a directly oil cooled electrical machine. Instead, they fitted

new correlations from the experimental data as,

$$Nu = 25.12Re^{15.407} \tag{2.2}$$

Pyrhönen et al. [52] manufactured a tooth-coil AFPM prototype generator with 75kVA target power having 12 stator slots and 10 poles to elucidate the thermal performance of the machine. The thermal conductance was improved by using copper bars as extra heat carriers in the construction and by using high-conductance potting material in the end windings of a liquid-jacket-cooled machine. Furthermore, potting of the stator of the axial machine could reduce the temperatures of the machine in an efficient way. The authors emphasized that axial-flux machines are quite vulnerable to overheating problems.

2.2.3 Lumped parameter model

Another approach for the thermal modeling of electrical machines is the application of the lumped parameter (LP) method [53–59]. In this technique, the electrical machine is split into a number of lumped components (or control volumes), which are connected to each other in the calculation scheme through thermal impedances to form a thermal circuit. The LP methods are known for their simplicity, quickness and acceptable level of accuracy. As a result, they can be a feasible alternative to the CFD modeling as well as the experimental analysis of AFPMSMs.

Numerous researchers have used LP thermal models to investigate the thermal performance of disk-type electrical machines. Hey et al. [60, 61] developed a hybrid LP and finite difference model to study the heat transfer process in an AFPMSM. Their results revealed that the model is able to predict the temperature of the machine within the acceptable experimental error margin. The simplicity of the mathematical model, used in the hybrid model allowed for fast computation which is essential for transient temperature prediction.

Lim et al. [62] used a 2-D (radial and axial directions) LP model which provides the steady state solution of temperatures within axisymmetric single-sided, slotted axial flux permanent magnet generators. The solid components and the internal air flow domain of the machine were split into a number of interacting control volumes, representing by thermal resistances and capacitances, shown in Fig. 2.4. The results have compared with the CFD and the experimental models in Fig. 2.5. The predicted temperatures from the LP model were slightly higher than the experimental ones. They demonstrated that in order to calculate the outlet air temperature accurately through the LP model, the results of the convective heat transfer

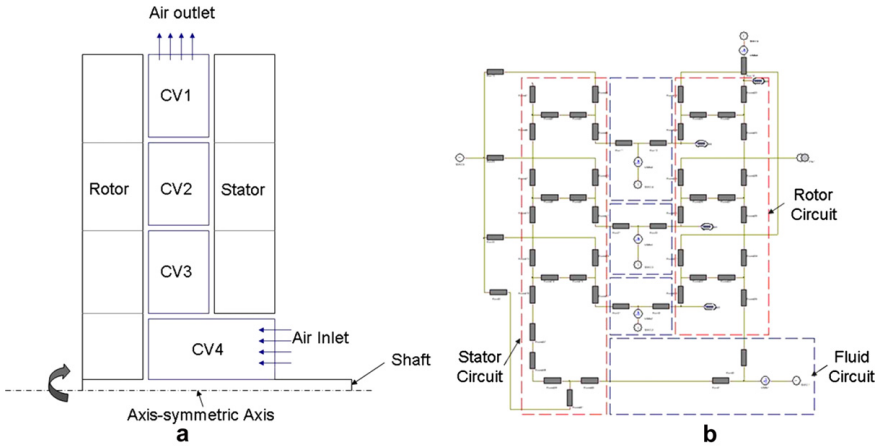

Figure 2.4: (a) Simplified single-sided slotted axial flux generator and (b) the corresponding lumped parameter thermal circuit [62].

coefficient from CFD model should be used instead of the empirical correlation reported by Owen [63]. In fact, Owen [63] provided an approximation solution for the flow between a rotating and a stationary disk, which relates the stator side average Nusselt number to the volumetric flow rate Q by the following equation,

$$\overline{Nu} = \frac{0.333Q}{\pi\nu R} \tag{2.3}$$

Rostami and his collogues [64] implemented the thermal analysis of a 5kW AFPMSM by means of a LP thermal method. As illustrated in Fig. 2.6, the geometry of the machine was subdivided into 13 elements with equivalent lumped-parameter blocks. All heat transfer mechanisms, namely conduction, convection and radiation, were included in the T-equivalent LP method. The empirical correlations reported by Sahin [28] have been used for the air-gap convection. It was shown by Sahin [28] that the mean Nusselt number in the air-gap can be defined by he gap Reynolds number $Re_s = \frac{vs}{\nu}$ and the corresponding Taylor number $Ta = (Re_s)^2 \frac{s}{R}$ as follows,

$$\overline{Nu} = \left\{ \begin{array}{ccc} 2 & if & Ta < 1700 \\ 0.128Ta^{0.367} & if & 1700 < Ta < 10^4 \\ 0.409Ta^{0.241} & if & 10^4 < Ta < 10^7 \end{array} \right\} \tag{2.4}$$

where v is the circumferential speed of the rotor. According to the comparison with the experimental data presented in Table 2.3, the LP method

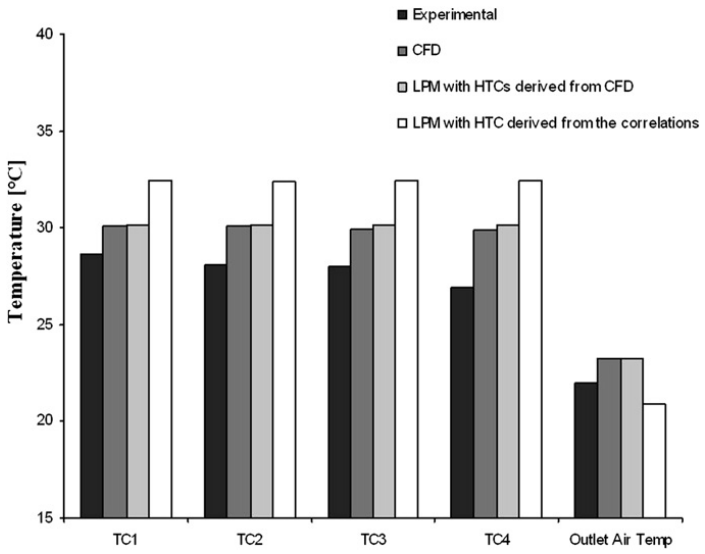

Figure 2.5: The temperatures measured and predicted from experimental rig and numerical models (CFD and LP) [62].

presented by Rostami et al. [64] is able to accurately predict the temperatures in different parts of the machine.

Table 2.3: Calculated and measured temperatures for designed AFPM generator [64].

Point	Calculated (°C)	Measured (°C)
Outer-end-winding	102	99
Slot winding	99	95
Magnet	80	79
Rotor	80	79
Frame	75	74
Bearing shield	80	78
Shaft	83	79

Notwithstanding the extensive applicability of LP methods in the aforementioned works, they are heavily dependent on the correctness of the surface heat transfer coefficient (HTC), particularly in the air-gap region of the disk-type electrical machines. In the literature, the lack of fast formulations to calculate t

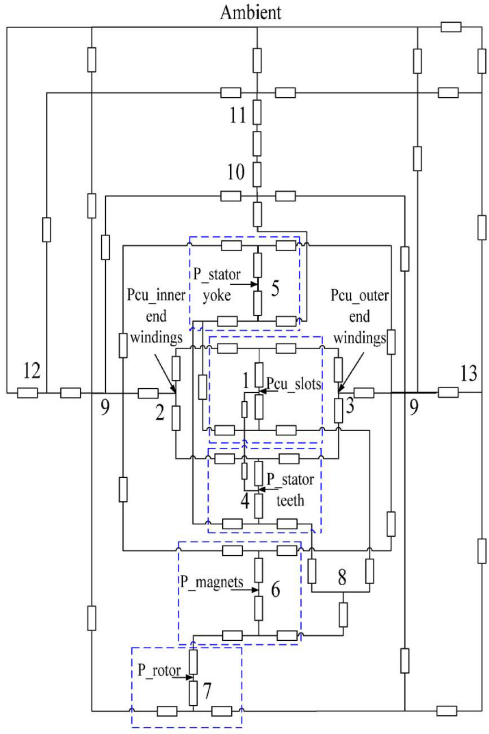

Figure 2.6: Equivalent thermal resistance network of an axial flux machine [64].

2.3 Windage losses in AFPMSMs

In AFPMSMs, the main sources of losses are the copper losses, the iron losses and the mechanical losses [65]. The latter are composed of the bearing losses and the windage losses. Windage power losses account for the power associated with the aerodynamic forces (viscous or pressure) against the rotary parts of the machine. The proportion of windage losses in electrical machines is usually moderate, albeit not completely insignificant [66]. While the electromagnetic analysis in the AFPMSMs has been widely addressed [67–69], the issue of windage losses in this type of electrical machines is not fully investigated [70–73].

Nonetheless, Vranick [74] pioneered the problem of the windage losses in rotating electrical machines considering the rotor as a long cylinder rotating in a stator with close gap distance. He developed a mathematical equation for drag losses in the alternators. Wild et al. [75] presented a computational method of the flow in the axial gap of the rotor and the stator along with

experimental windage torque measurement. They indicated that the Taylor vortices result in axial variations of the azimuthal shear stress. Anderson et al. [76] simulated air cooling and windage losses in a high-speed electric motor. They proposed correlations to ascertain the drag force acting on the rotor of the motor that matched with the empirical data.

For disk-type electrical machines, empirical correlations that treat the rotor as a flat disk have been used to calculate the windage power losses [77–79]. Giovanni [80], however, took the effect of the magnets in the rotor disk on the windage power losses assessment into account. They carried out a CFD-parametric study in an AFPMSM with rotor diameter of 220 mm, gap size of 2 mm and the angular velocity of 1500 rpm for various magnet thicknesses. They found that an increase in the magnet groove depth from 2 to 18 mm can noticeably intensify the air mass flow rate and the windage losses (up to 10 W) through the generator (see Fig. 2.7).

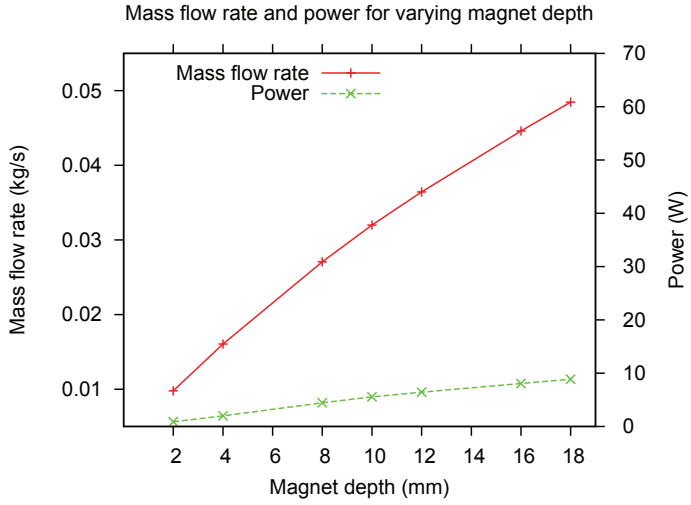

Figure 2.7: Windage losses and mass flow rate [80].

Furthermore, the influence on the windage losses of protrusions at the rotor disk, resembling the magnets in the machines, has been discussed by Luo et al. [82], for a rotor-stator system with superimposed central inflow. They showed that the effect of the protrusion totally undermines the effect of the air-gap size on the friction torque. Liu et al. [83] shed further light on the effect of the angular distance between protrusions and their thickness on the windage losses in the rotor-stator systems.

Wrobel et al. [81, 84] performed CFD simulations to assess the windage losses in an AFPMSM. They investigated the aerodynamic effects occurring

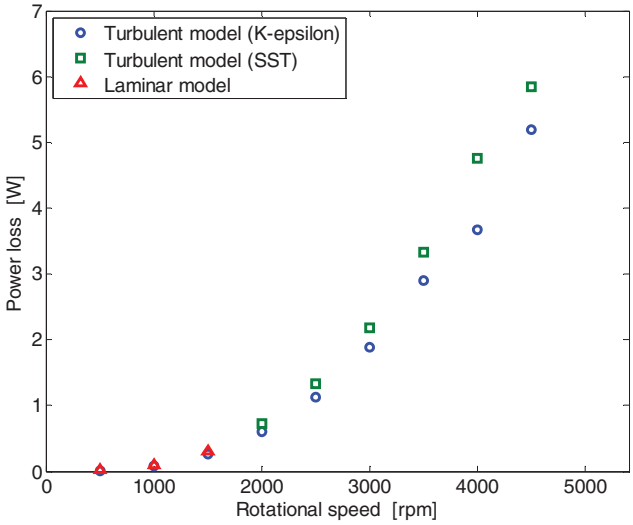

Figure 2.8: CFD prediction of windage/drag loss [81].

within the air-gap. They calculated the variation of windage losses in the machine versus the rotational speed of the rotor given by various turbulence models according to Fig. 2.8. It was also concluded that the windage/drag loss generated in the analysed machine assembly is relatively small e.g. about 8% of the bearing loss, at 4000 rpm.

Similar to the correlations for the convective heat transfer coefficients, the presence of fast correlations to assess the the windage losses in an AF-PMSM is missing in the literature.

2.4 Rotor-stator flow and heat transfer

Although the real machine has a very complex geometry, the understanding of the flow pattern in a simple rotor-stator system can be instructive and a good representative of the flow and heat transfer in a real disk-type electrical machine. Thus, the literature study in this regard will be explained in the sections below.

2.4.1 Flow structure in rotor-stator systems

The literature is thriving with several aspects of the rotor-stator configurations. The classification ranges from through/in-flow of air in the rotor-stator cavity, the enclosed/fully open discoidal systems and different flow regimes, i.e., laminar or turbulent flow.

Batchelor [85] mathematically solved the flow between infinite rotor and stator disks. He showed that there are two distinguishable boundary layers on each disk with an inviscid rotating core of fluid at large Reynolds numbers. By contrast, Stewartson [86] identified a different flow structure where the tangential velocity is maximum on the rotor surface and it starts to drop away from the rotor and reaches to zero at the stator surface, with no core rotation. This historic controversy for the same problem was later attributed to the appearance of the enclosure [87]. In other words, the Batchelor flow type is observed for the case of the enclosed rotor-stator system, while the absence of the core rotating flow, i.e. Stewartson flow type, occurs for the open rotor-stator arrangements. It is the condition at the boundary that determines whether the flow will tend toward a Batchelor or a Stewartson type pattern. In an enclosed rotor-stator system, a recirculation of fluid from rotor to stator occurs at the periphery leading to Batchelor flow, whereas the core rotation is often destroyed in open discoidal system with radial through-flow resulting in a Stewartson flow.

In addition to that, Soo [88] demonstrated that the flow structure depends on the parameter X_0, for laminar flow in a rotor–stator system with an imposed airflow at the center of the stator with large gap size ratio.

$$X_0 = \left(\frac{C_w Re^{-1/2}}{\pi}\right)^{1/2} \tag{2.5}$$

In this equation $Re = R\omega^2/\nu$ is the rotational Reynolds number, $C_w = \dot{m}/\mu R$ represents the mass flow rate coefficient, $\dot{m}$ is the mass flow rate, μ denotes the dynamics viscosity of air, and R is the radius of the rotor disk. It has been deduced that when $X_0 < 1$, the flow is of the Batchelor type with a radial outflow on the rotor and a radial inflow on the stator, separated by a core of fluid rotating at approximatively 0.38ω, where ω is the angular velocity of the rotor. For the case of $X_0 > 1$, the flow is of the Stewartson type with an radial outflow on the rotor and without the formation of a rotating core of fluid.

Daily and Nece [89] conducted an experimental study and defined four different flow regimes in a totally enclosed rotor-stator system with no through-flow, shown in Fig 2.9, depending on the values of the non-dimensional gap size ratio, $G = s/R$, and the rotational Reynolds number, $Re = \omega R^2/\nu$ as follows,

- Regime I: merged laminar boundary layers (at low G and Re).
- Regime II: two distinguishable laminar boundary layers separated by a core rotating fluid (at high G and low Re)
- Regime III: merged turbulent boundary layers (at low G and high Re)

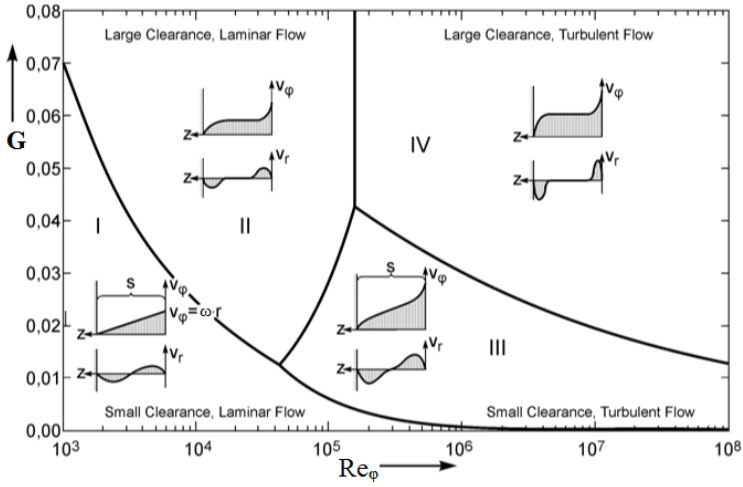

Figure 2.9: Four distinct flow regimes by Daily and Nece [89].

- Regime IV: two distinguishable boundary layers (at high G and Re)

It is clear from Fig. 2.9 that regimes II and IV correspond to a Batchelor type flow with the core rotation. Also, the narrow gap sizes (I and III) essentially represent a viscous Couette-type of flow. Furthermore, Daily and Nece [89] presented correlations for the non-dimensional moment coefficients, C_m, in each regime:

$$C_m = \left\{ \begin{array}{cc} \frac{\pi}{G.Re} & RegimeI \\ 1.85G^{\frac{1}{10}}Re^{-\frac{1}{2}} & RegimeII \\ 0.04G^{-\frac{1}{6}}Re^{-\frac{1}{4}} & RegimeIII \\ 0.0501G^{\frac{1}{10}}Re^{-\frac{1}{5}} & RegimeIV \end{array} \right\} \tag{2.6}$$

From the above equation, the torque on the rotor disk T_q, is then calculated as,

$$T_q = 0.5C_m\rho\omega^2R^5 \tag{2.7}$$

From the torque, the windage power losses $P = T_q\omega$, can be easily estimated.

After some subsequent progress in the rotor-stator flow [90–92], Cooper and Reshotko [93] reported that near the axis of rotation the flow is laminar and the boundary layer thickness is approximately constant. If the gap width is large, the boundary layers are separated. After transition to turbulence, the separated boundary layers thicken and eventually merge when the gap size ratio, G, is sufficiently small. Kobayashi [94] pointed out that for

a single disk rotating in a quiescent environment the flow is fully turbulent at the rotational Reynolds number $Re = 3.9 \times 10^5$, whereas for the confined rotor-stator system transition occurs at lower Reynolds numbers. Daily and Nece [89] concluded that the flow becomes fully turbulent at $Re \approx 1.5 \times 10^5$ for the gap size ratio larger than 0.04. For the gap size ratio smaller than 0.04, the transition to turbulence takes place at lower Reynolds numbers (See Fig. 2.9). Additionally, Itoh et al. [95] showed through an experiment that the transition to fully turbulent flow was completed at $Re = 4.6 \times 10^5$ for $G = 0.08$.

Singh and Rajvanshi [96] presented the numerical solution for the flow between a rotating and a stationary disk made up of porous material. The skin friction was predicted for different values of the Reynolds number. Bujurke and Achar [97] found a semi-analytical solution to the same problem with lower Reynolds numbers, and found the singularity of the perturbation series.

As mentioned earlier, the type of flow pattern in a rotor-stator system also depends on the presence of an enclosure. For the case of the enclosed rotor-stator arrangement, Cheah et al. [98] experimentally investigated the rotor-stator cavity for the Reynolds number range from 0.3×10^6 to 1.6×10^6. Three different experimental techniques, including laser-Doppler anemometry, hot-film velocimetry and the yaw-tube method, were employed to measure the variation of the mean and some of the fluctuating velocity components across the rotor-stator cavity. They showed that at high rotational speeds, the Ekman-type boundary layer on the rotor is laminar over the inner half of the cavity and turbulent at the outer radial locations. The stator boundary layer, on the other hand, is turbulent over most of the cavity, and the high near-wall turbulence levels extend further into the core. By contrast, at low rotational speeds ($Re \leq 0.3 \times 10^6$) the rotor boundary layer is laminar over almost the entire cavity. The stator boundary layer remains turbulent. The distinct behaviour on the rotor and the stator surface was interpreted as a result of the outward radial flow near the rotor boundary layer, whereas there is radially inward flow adjacent to the stator disk. The problem of the flow field between rotating disks enclosed by a cylinder has been further studied by Bhattacharyya and Pal [99]. They indicated that the similarity solution is useful in describing the flow between finite disks for small values of the Reynolds number. Severac et al. [100] performed Large Eddy Simulation (LES) by means of a Spectral Vanishing Viscosity (SVV) technique to solve the turbulent enclosed rotor-stator flow up to $Re = 10^6$. They have also showed that the stator boundary layer is turbulent over most of the cavity if the Reynolds number is larger than 10^5. The rotor layer becomes progressively turbulent from the outer radial

locations, although the rotating hub is shown to destabilize the inner part of the boundary layers.

Regarding the open rotor-stator systems, Lygren and Andersson [101, 102] used direct numerical simulation (DNS) to unveil the coherent structures of the rotor-stator flow. They indicated that the origin of the crossflow near the rotating disk is an imbalance between the centrifugal and pressure forces, while the crossflow near the stationary disk is pressure driven. Nevertheless, the ensemble-averaged coherent structures in the boundary layers near the rotating and stationary disks were noticeably similar to each other. Moreover, it was found that the variation of the mean tangential velocity between two disks closely resembles the mean velocity profile in plane Couette flow. Jacques et al. [103] performed numerical simulations of turbulent flows in rotor stator cavities using a finite difference algorithm based on a multi-domain decomposition strategy under the assumption of axisymmetry. It was shown that the flow becomes first turbulent on the stator while the rotor boundary layer remains completely laminar and that the two boundary layers continue to behave differently at larger Reynolds numbers. In the turbulent regime, it was realized that the large eddies ejected from the stator boundary layer into the core keep the internal waves in the core permanently excited.

Furthermore, Andersson and Lygren [104] performed LES of the axisymmetric and statistically steady turbulent flow between a rotating and a fixed disk. Both narrow and wide gap sizes were studied. It was demonstrated that the variation of the tangential mean flow between the disks for the narrow-gap closely resembled the S-shaped mean velocity profile in a turbulent Couette flow. In the wide-gap cases, however, a nearly homogeneous core region separated the three dimensional boundary layers adjacent to the rotor and the stator. In spite of the fundamentally different core regions for the narrow and wide gap sizes, the three-dimensional flow fields in the vicinity of the two disks exhibit the same general features.

Cros et al. [105] experimentally examined the transition to turbulence of the flow confined between a stationary and a rotating disk using visualization and video image analysis. Nevertheless, in the review reported by Launder et al. [106], it was indicated that the question of the transition scenario in the rotor-layer still remains open.

Nevertheless, Howey [107] indicated that the Langtry and Menter $\gamma - \theta$ transition provides good results to model the transitional flow in the rotor-stator configuration in the disk-type electrical machines.

2.4.2 Heat transfer in rotor-stator systems

Soo et al. [108] pioneered the problem of the laminar heat transfer in a discoidal configuration. The predicted Nusselt number was scaled by the gap size (s). Owen [109, 110] used the Reynolds analogy to a rotor-stator system assuming a turbulent Prandtl number ($Pr_t = \overline{V_\theta' V_z'} \frac{\partial V_\theta}{\partial z} / \overline{T' V_z'} \frac{\partial T}{\partial z}$) of unity and equal radial and tangential eddy viscosities. It was shown that considering the frictional heating effects one can find the adiabatic rotor disk temperature as,

$$T_{ad} = T_\infty + \frac{1}{2}\omega^2 r^2 / c_p \tag{2.8}$$

where c_p is the specific heat capacity at constant pressure.

Arora and Stokes [111] investigated the heat transfer for the steady axisymmetric flow of an incompressible fluid between two parallel infinite disks. It was shown that once both disks rotate with the same angular velocity, the fluid moves as a rigid body having the same angular velocity as that of the disk. Hence, there is no dissipation and the heat transfer is only due to conduction through the fluid. The theoretical investigation on the unsteady mixed convection flow and heat transfer between two infinite coaxial isothermal disks was carried out by Soong and Ma [112]. The density variation in the centrifugal force term was considered so as to account for the centrifugal-buoyancy effects. They showed that for the asymptotic mode, centrifugal-buoyancy can only alter the steady-state solutions quantitatively; however, the qualitative natures of the transient flow, e.g., the growth and decay of the Ekman layer and the period of the transient stage, cannot be significantly affected by the centrifugal-buoyancy effect.

Wilson et al, [113] measured the heat transfer in a preswirl rotor-stator rig, and the measurements were compared with computations obtained from an axisymmetric elliptic solver. It was reported that the computed Nusselt numbers for the rotor tended to underpredict the measured values.

Harmand et al. [114] conducted an experiment to estimate the local convective heat transfer from a rotor with a 310 mm outer radius at a distance of 3 mm from a coaxial crown-shaped stator. The local heat flux distribution from the rotor surface was identified by resolving the Laplace equation by finite difference method using the experimental temperature distribution as boundary conditions. The author suggested that the local convective heat transfer decreases as a function of the radius on the rotor facing a crown-shaped stator and featuring a large central opening, contrary to the free disc. Ellwood and Korchinsky [115] experimentally studied the viscous dissipation energy generated by a closely spaced rotor-stator system. They indicated that theoretical predictions of viscous dissipation rates were

near those obtained experimentally.

Roy et al. [116] performed an experimental analysis of the fluid temperature distribution and the convective heat transfer coefficient assessment on the rotor disk surface in a rotor-stator disk cavity. The heat transfer coefficient was obtained as the ratio of the local surface heat flux and the local temperature difference across the thermal boundary layer. Then, in the range of $4.6 \times 10^5 \leq Re \leq 8.6 \times 10^5$ they developed an empirical correlation for the local convection coefficient on the rotor disk as a function of local rotational Reynolds number as,

$$Nu_r = 0.0195 Re^{0.80} \tag{2.9}$$

Boutarfa and Harmand [117] performed an experiment to investigate the flow structure and the local convective exchanges in the air-gap of a rotor-stator system. Infrared thermography was utilized to measure the surface temperatures of the rotor for the range of $5.87 \times 10^4 \leq Re \leq 1.74 \times 10^5$ and $0.01 \leq G \leq 0.17$. The mean Nusselt numbers were reported for different ranges of the gap size ratio as show in Eq. (2.10),

$$\begin{array}{ll} \overline{Nu} = 7.46 Re^{0.32} & G = 0.01 \\ \overline{Nu} = 0.50(1 + 5.47 \times 10^{-4} e^{112G}) Re^{0.5} & 0.02 \leq G \leq 0.06 \\ \overline{Nu} = 0.55(1 + 0.462 e^{\frac{-13G}{3}}) Re^{0.5} & G > 0.06 \end{array} \tag{2.10}$$

Beretta and Malfa [118] developed a semi-empirical model for the adiabatic-rotor/isothermal-stator configuration to find the temperature fields and heat fluxes. It was observed that the radial distribution of temperature difference between rotor and stator surfaces is parabolic. The rotor-stator temperature difference does not depend on the fluid density, but depends merely on the specific heat and only slightly on thermal conductivity and viscosity through the Prandtl number. Thus, density reduction will reduce the power dissipation but will not increase the rotor surface temperature.

Pellé and Harmand undertook a number of researches to investigate different aspects of the heat transfer in rotor-stator systems [119–122]. The same experimental set-up was used for all studies. The set-up is based on the infra-red (IR) thermography method and is depicted in Fig. 2.10

In their first study [119], the rotor-stator system was open at the periphery, but it had no air inlet at the center. Four different regimes with corresponding correlations for heat transfer were identified, based on different values of G and Re. It was found that for the case of wide-gap size ratios, the rotor heat transfer is approximately the same as that of a free disk. With some modification to the experimental set-up, the presence of the impinging air jet on the rotor surface from the stator inlet was taken into account [120, 121]. The jet was defined by a jet Reynolds number

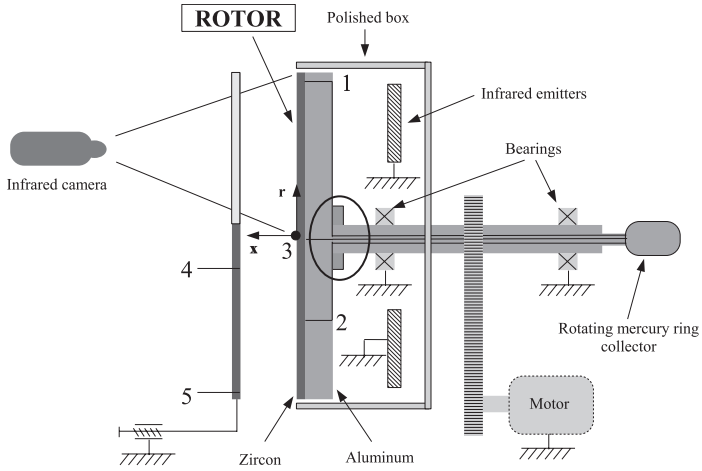

Figure 2.10: Experimental set-up [119].

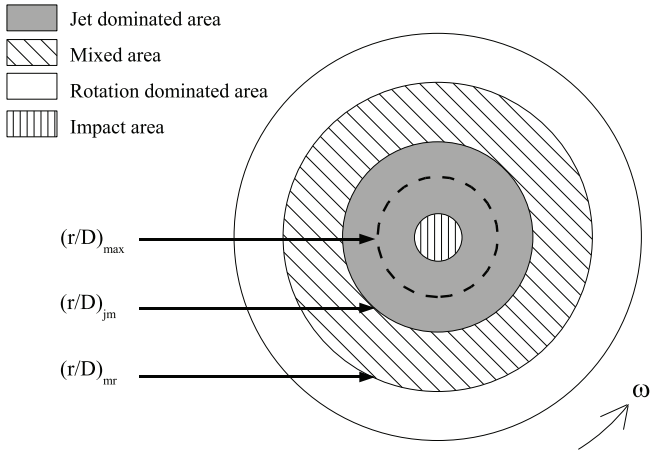

Figure 2.11: Phenomena at the rotor surface-correlated parameters [121].

($Re_j = V_j D/\nu$), with a range of $0 < Re_j < 4.2 \times 10^4$. Different areas on the rotor surface were detected. It was concluded that the addition of a jet impinging on the center of the rotor is advantageous for the heat transfer, primarily near the stagnation point. For higher radii, the experimental convective heat transfer rates were similar to those obtained without a jet. The influence of a natural suction through multiple holes in the stator of a discoidal configuration was studied in [122]. They demonstrated that the maximum convective heat transfer rates are obtained when $G = 0.02$. They

are lowest when the stator is a full disk.

In most studies concerning the heat transfer phenomena in the discoidal arrangement, the rotor disk was mainly focused on as it is much of interest in turbo-machinery applications [123–130]. The stator surface heat transfer has received less attention. In this sense, Yuan et al. [131] experimentally determined the stator heat transfer in an open rotor-stator disk system with no through-flow, using thermographic liquid crystals for stator temperature measurements. CFD simulations were also performed, using the RNG $k-\epsilon$ turbulence model. Only three gap size ratios were considered, namely $G = \{0.049, 0.073, 0.098\}$. The rotational Reynolds varied between 1.42×10^5 and 3.33×10^5. The authors concluded that there exists an optimum rotor-stator distance for a given Reynolds number, at which the average heat transfer rate on the stator reaches maximum. When the Reynolds number increases, the maximum shifts towards smaller disk-distances.

Besides that, concerning the stator heat transfer, there are a number of studies conducted by Howey et al. [107, 132–136]. In all of these works, both CFD simulations and experimental analysis have been undertaken. Two rotor configurations were tested: a flat rotor ($R1$), and a rotor with 16 protrusions designed to mimic the magnets on an AFPMSM ($R2$). An electrical heater array was used to measure the stator heat transfer rate in a rotor-stator system, with axial inflow from an inlet at the stator center. In the simulations using rotor $R2$, the inlet mass flow rate was specified directly from the experimental results, instead of specifying the inlet total pressure. Additionally, the $R2$ simulations used a rotating reference frame for the fluid domain, with boundary conditions specified in relation to this. It was demonstrated that the average stator heat transfer rate for various gap sizes using $R1$ (flat rotor) can be correlated in the turbulent regime according to a power law as,

$$\overline{Nu}_{turb} = ARe^B \tag{2.11}$$

The constants A and B are given in Table 2.4; these are valid in the range of $5.19 \times 10^5 \leq Re$ for the data shown.

On the other hand, the measured stator heat transfer rate for rotor $R2$ may be correlated by a linear equation in the range $7.4{\times}10^3 \leq Re \leq 5.9{\times}10^5$ as follows:

$$\begin{aligned} \overline{Nu} &= 0.00067Re + 118 \quad \text{for} \quad G = 0.0212 \\ \overline{Nu} &= 0.00062Re + 110 \quad \text{for} \quad G = 0.0106 \end{aligned} \tag{2.12}$$

A comparison between measured stator heat transfer for $R1$ and $R2$ was made in Fig. 2.12. The results showed that the average stator heat transfer with $R2$ is about 20-30 % higher than $R1$ at a comparable speed.

Table 2.4: The coefficients of Eq. (2.11) for different gap size ratios [133].

G	A	B
0.0106	0.0790	0.640
0.0127	0.0888	0.633
0.0170	0.0406	0.628
0.0212	0.0315	0.691
0.0297	0.0347	0.679
0.0467	0.0234	0.712

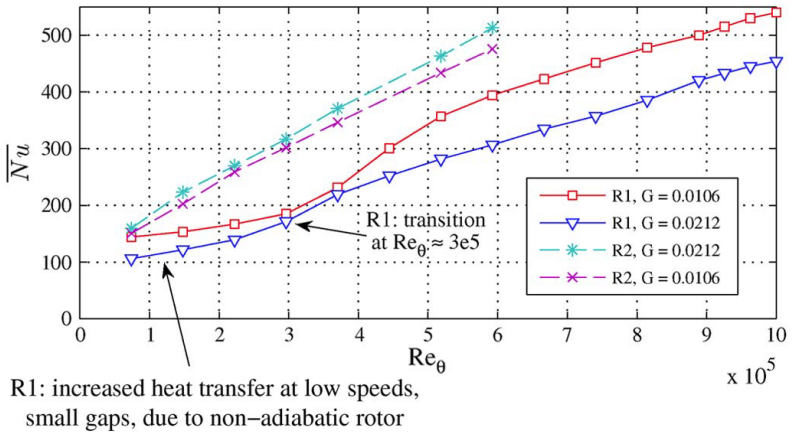

Figure 2.12: Comparison of measured average heat transfer $R1$ versus $R2$ [134].

Most of the aforementioned studies, for simplicity, have used the air ambient temperature as the reference temperature to calculate the convective heat transfer coefficient in the gap between the rotor and the stator. By doing so, the estimated convection coefficient becomes dependent on the ambient temperature which is an unwanted effect. In fact, it results in a limited applicability of those correlations. The main contribution of this work is to give a way of determining the bulk temperature in a relatively straightforward manner, by the barycentric combination of the surface temperatures and the ambient or cover temperature.

2.5 Conclusion

In this chapter, different aspects of thermal analysis of an AFPMSM studied in the literature were presented. In order to avoid overheating, which is detrimental to the machine performance, proper thermal modeling should be used to accurately predict the temperature distribution within the machine in the course of peak load of the working condition. To this end, three approaches have been increasingly used, namely numerical methods, experimental studies as well as LP thermal models.

The numerical modeling of the complete machine, through both CFD and FE models, was shown to be effective with providing the aerodynamics effects of the rotor with magnets, acting like radial channels. The RANS models have mostly been used in the literature for the thermal modeling in AFPMSM.

Given the complexity of the real machine, the experimental study of the AFPMSM has gained less attention. In addition to the numerical and the experimental techniques, the most common way to calculate the temperature distribution in the machines is the LP method, which is relatively fast to solve using a thermal resistance network. However, the accuracy of this method substantially depends on the accuracy of the convective heat transfer coefficients of the machine surfaces.

The windage power loss is another aspect in the machine which can be very important at high speed applications. The literature seems to be missing the quick formulations to predict theses losses for different physical and geometrical parameters.

Also, it was indicated that the air-gap convection has a significant impact on the cooling of disk-type electrical machines. From the survey of the available literature, it appears that the ambient temperature is used as the reference temperature to evaluate the convective heat transfer coefficient in the rotor-stator systems. This makes the presented correlations for the mean Nusselt numbers only applicable for a given surface temperature of the rotor and the stator, which is a serious drawback. To tackle this problem, different approaches are taken into account in the current research. The details will be explained in the next chapters.

3

Rotor-Stator system in an enclosed cylinder [1]

The literature review in the previous chapter has demonstrated that the accurate modeling of the fluid mechanics in the air-gap between the rotor and the stator is of great practical concern in the cooling of the disk-type electrical machines. This chapter, therefore, discusses the numerical modeling of the flow and heat transfer in a simple rotor-stator arrangement enclosed in a cylinder, which represents a simplified geometry of the actual topology of the AFPMSM.

Most of the previous studies, for simplicity, have used the air ambient temperature as the reference temperature to calculate the convective heat transfer coefficient in the gap between the rotor and the stator. By doing so, the estimated convection coefficient is only valid for the specific surface temperature used in the development of the correlation. This is an unwanted effect that results in a limited applicability of those correlations. In this chapter, however, the average bulk fluid temperature has been calculated and is used as the reference temperature. In this way, the convective heat transfer coefficients and the mean Nusselt numbers in the gap will be

[1] This chapter is based on the journal paper: A. Rasekh, P. Sergeant and J. Vierendeels, "Convective heat transfer prediction in disk-type electrical machines" Journal of Applied Thermal Engineering, 91:778-790, 2015 and the conference paper: A. Rasekh, P. Sergeant and J. Vierendeels, "A parametric-CFD study for heat transfer and fluid flow in a rotor-stator system", 11TH World congress in computational mechanics, VOLS II - IV. p.4475-4483, 2015.

independent of both the ambient temperature as well as the corresponding surface temperatures.

First, the different flow types occurring in the air-gap region of a simple rotor-stator system are discussed. Furthermore, the influence of the holes in the rotor disk on the overall heat transfer in the current discoidal system is investigated. Based on the CFD results, parameterized correlations for the convective heat transfer coefficient in the rotor-stator system used in disk-type electrical machines are developed. Details of the proposed method and the applications of these correlations are presented in the following sections.

3.1 Problem set-up

Fig. 3.1 shows the actual configuration of the rotor-stator in a typical AFPMSM. The simplified arrangement of the discoidal system has been illustrated in Fig. 3.2, where the left disk represents the rotor and the right one is the stator. The rotor-stator system is enclosed in a cylindrical cover. The case study consists of two rotors and one stator in the middle. Hence, a symmetry plane has been defined to halve the computational cost. The flow is characterized by the rotational Reynolds number, $Re = \omega R^2/\nu$, and the gap size ratio, $G = s/R$, where ω is the angular velocity of the rotor, R is the radius of the disks, ν is the kinematic viscosity of air and s is the air-gap distance. This model has been constructed in the practical range of AFPMSMs namely $4.19 \times 10^4 \leq Re \leq 4.19 \times 10^5$ and $0.00333 \leq G \leq 0.08$. For the considered disks of 75 mm radius, this range of Reynolds number corresponds to the rotor tip velocity of 10 to 100 m/s and the range of the gap size ratio denotes to the gap size of 0.25 to 6 mm. The following assumptions for constructing the model have been made:

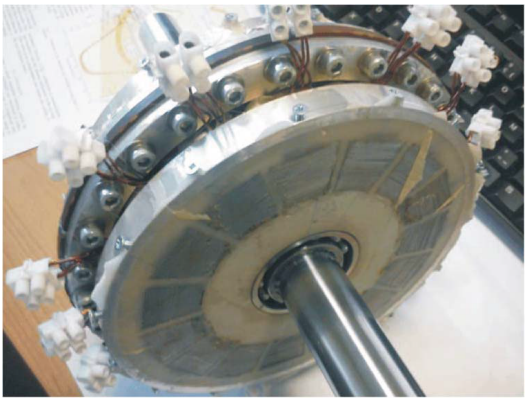

Figure 3.1: The rotor-stator configuration in an AFPMSM [7].

1. Since the thermal conductivity of the material in the rotor and the stator is relatively high, the use of an isothermal boundary condition for each element (rotor, stator & cover) is consistent with the actual operation condition. The Biot numbers ($Bi = \frac{hL_c}{k}$) for the rotor and the stator disks at the reference point are 0.0001 and 0.002, respectively.

2. Air is considered as an incompressible ideal gas, so its density varies with temperature and is computed as below,

$$\rho = \frac{P_{atm}}{\overline{R}T} \tag{3.1}$$

Where P_{atm} is the atmospheric pressure, T is air temperature, and $\overline{R}$ is the specific gas constant.

3. Other fluid properties are estimated at 50°C. The Prandtl number ($Pr = \mu c_p/k$) is 0.7.

4. The radiative heat transfer can be assessed based on the rotor, stator and cover temperatures. For example, radiative heat exchange between rotor and stator disk is calculated through the following equation,

$$\dot{Q}_{rad} = \frac{\sigma(T_s^4 - T_r^4)}{\frac{1-\varepsilon_s}{A_s\varepsilon_s} + \frac{1}{A_s F_{sr}} + \frac{1-\varepsilon_r}{A_r\varepsilon_r}} \tag{3.2}$$

where A_r and A_s are the surface areas of the rotor and the stator in the gap, σ is the Stefan-Boltzmann Constant, ε_r and ε_s denote the emissivity of rotor and stator surfaces, respectively. F_{sr} represents the view factor which is equal to around one as the length of gap is very small. The radiative heat transfer rates from stator surface in gap and stator sidewall are 3.0 and 7.9 W when $T_r = 100$°C, $T_s = 120$°C, $T_c = 50$°C. It should be noted that the convective heat transfer rates will be focused in this thesis, and the radiative heat flux, which is somewhat small, can be separately introduced to the coupled thermal and electromagnetic model.

5. The buoyancy effect is taken into account, and the gravity vector is considered perpendicular to the rotor and the stator axis, shown in Fig. 3.2(b).

3.2 Results of CFD simulation

The case of $Re = 1.26 \times 10^5$ and $G = 0.01333$ is chosen as a reference point. The 3-D CFD simulations have been implemented for different tem-

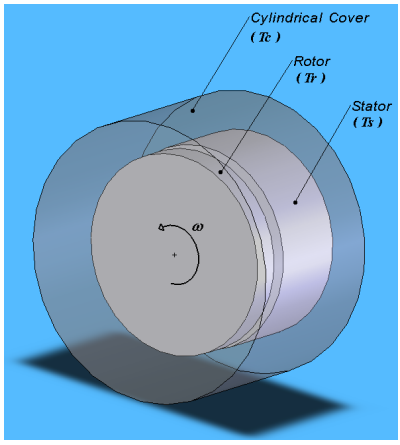

(a)

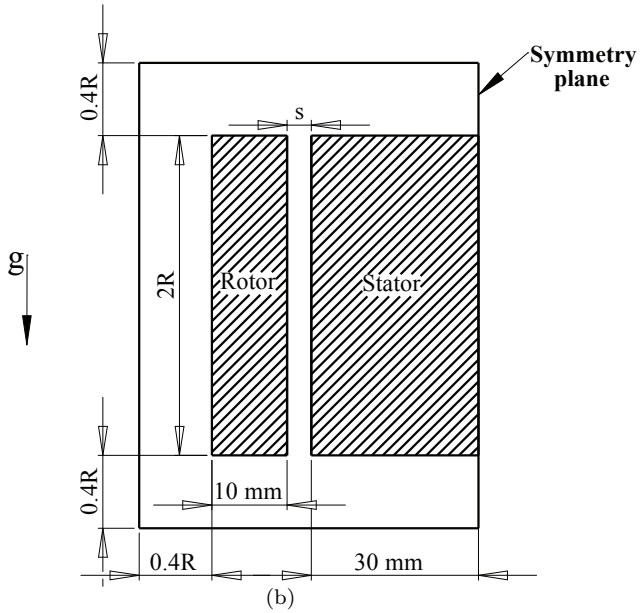

(b)

Figure 3.2: The rotor-stator system in an AFPMSM (a) the schematic diagram (b) the geometrical details.

perature combinations of the rotor, the stator and the cover at the reference point. The commercial CFD software Ansys FLUENT has been used to simulate the 3-D flow fields. The equations are solved by using the SIMPLE-algorithm and the convective terms in the momentum, turbulence and energy equations are spatially discretized using a second-order upwind scheme. The turbulence is treated with a SST $k-\omega$ model and the meshes in the boundary layers around the solid walls were designed to obtain a y^+ value below 1. The convergence of the solution is achieved once the monitored values of the surface heat fluxes reach a constant value, along with keeping the relative residuals of momentum-related variables lower than 10^{-5}, the residuals of the turbulence-related variables below 10^{-6} and the residual of the energy under 10^{-8}.

The mesh constructed for this benchmark consists of hexahedral cells. Fig. 3.3 clarifies the surface mesh of the rotor disk. The length of the first cell in the vicinity of the walls is 100 μm. In the air-gap, there are 30 cells in the axial direction. A mesh refinement analysis was performed to study the effect of the grid size on the heat transfer rate in each surface within the system. The computational mesh contains 2,604,000 cells and by comparing the grids with 753,000 and 6,097,000 cells, it was found that the mesh resolution is fine enough and the results are rather mesh-independent with the relative error of 0.1% in predicting the stator heat transfer rate. Due to the fact that the buoyancy effect has not been neglected a priori, 2-D axisymmetric simulations were not used.

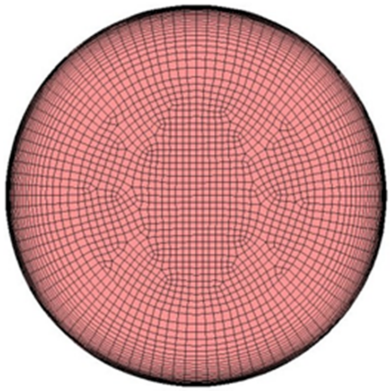

Figure 3.3: The surface mesh of the simple rotor disk.

3.2.1 Flow structure in the air-gap

To give a clear insight about the fluid pattern in this configuration, the radial and axial velocity contours at the periphery of the air-gap between the rotor and stator have been depicted in Fig. 3.4, where the Reynolds number and the gap size ratio are kept at $Re = 1.26 \times 10^5$ and $G = 0.01333$.

Fig. 3.5 shows the velocity vectors at the periphery of the air-gap. Note that the left disk is the rotor and the right one represents the stator. The maximum radial velocity component of the airflow at the outer radial location of the air-gap is about 1.9 m/s. There are two distinguishable regions; a strong radial outflow adjacent to the rotor due to the centrifugal force and a weak inflow region close to the stator disk. The inflow close to the stator is consistent with the conservation of mass.

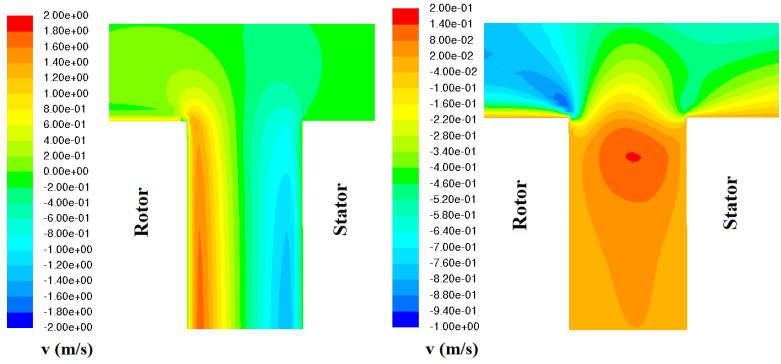

Figure 3.4: Velocity contour in a vertical plane through the axis at the periphery of the air-gap (a) radial velocity, (b) axial velocity at $Re = 1.26 \times 10^5$ and $G = 0.01333$.

To find out more about the flow pattern behaviour, the radial, axial and tangential velocity profiles alongside the air-gap for different gap size ratios are illustrated in Figs. 3.6- 3.8, respectively. The horizontal axis denotes the position in the air-gap, where $x/s = 0$ is the rotor surface and $x/s = 1$ is the stator surface. For the small gap size, the centrifugal boundary layer of the rotor is merged with the centripetal stator boundary layer. The flow is dominated by strong viscous effects, which is known as Couette flow. In fact, the Couette flow structure emerges as the gap Reynolds number ($Re_s = \omega s^2/\nu$) is below 100 [137], and for our cases (G=0.00333, 0.01333, 0.04 & 0.08) in these profiles (Re_s=1.3, 22, 201 & 804).

As the gap distance increases, two unmerged boundary layers appear with a rotating core of the fluid, which is known as the Batchelor flow

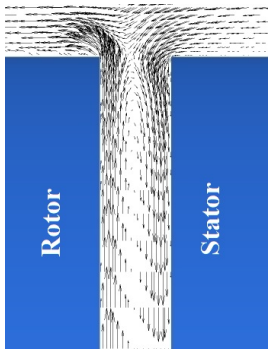

Figure 3.5: Velocity vector at the periphery of the air-gap for $Re = 1.26 \times 10^5$ and $G = 0.01333$.

regime. For $G = 0.04 - 0.08$, there seems to be a strong radial velocity component outward close to the rotor, whereas a weaker inward component of radial velocity near the stator is observed. In other words, the radial velocity component adjacent to the stator is expected to weaken further for the wider gap distances.

Different trends can be seen for the axial velocity component profiles in the air-gap (see Fig. 3.7). In fact, for narrow gaps, there is almost no flow in the axial direction. For wide gaps, the negative values of axial velocity near the rotor disk imply that the flow tends to penetrate towards the rotor boundary layer in almost all radii to replace the fluid which has been pumped out. According to Fig. 3.8, the tangential velocity component variations alongside the air-gap for the narrow gap are almost linear which is compatible with the Couette flow characteristics. For the wide gap size, the variations of the tangential velocity in the gap show two separate boundary layers on the rotor and the stator.

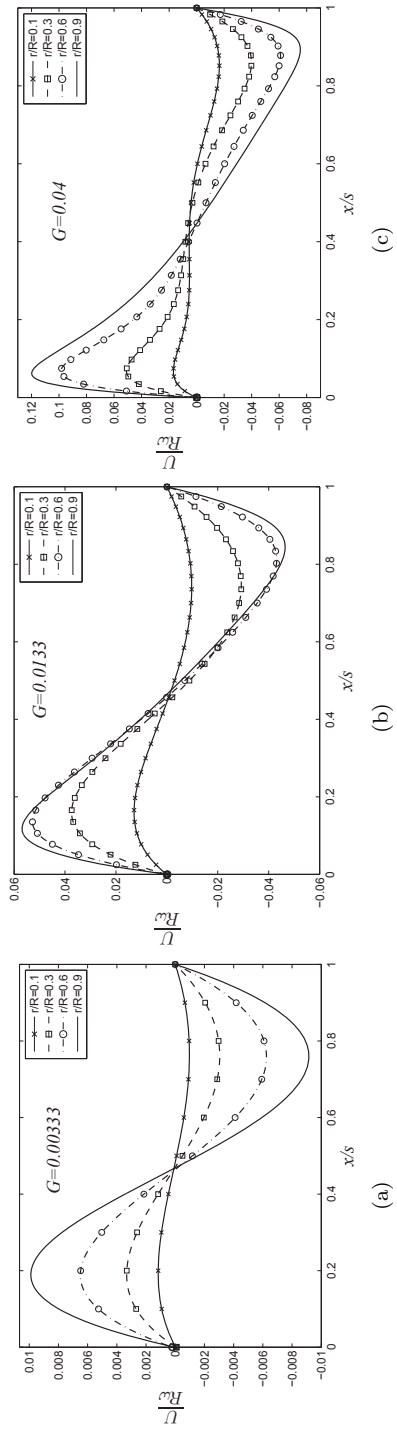

Figure 3.6: Non-dimensional radial velocity variation across the air-gap at $Re = 1.26 \times 10^5$ for (a) G=0.00333 (b) G=0.0133 (a) G=0.04 (a) G=0.08.

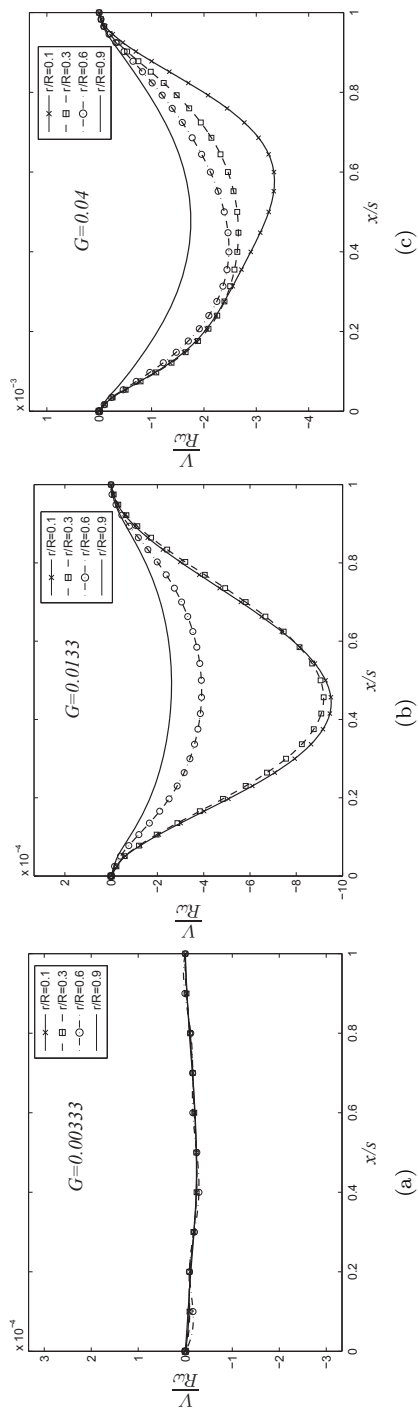

Figure 3.7: Non-dimensional axial velocity variation across the air-gap at $Re = 1.26 \times 10^5$ for (a) G=0.00333 (b) G=0.0133 (a) G=0.04 (a) G=0.08.

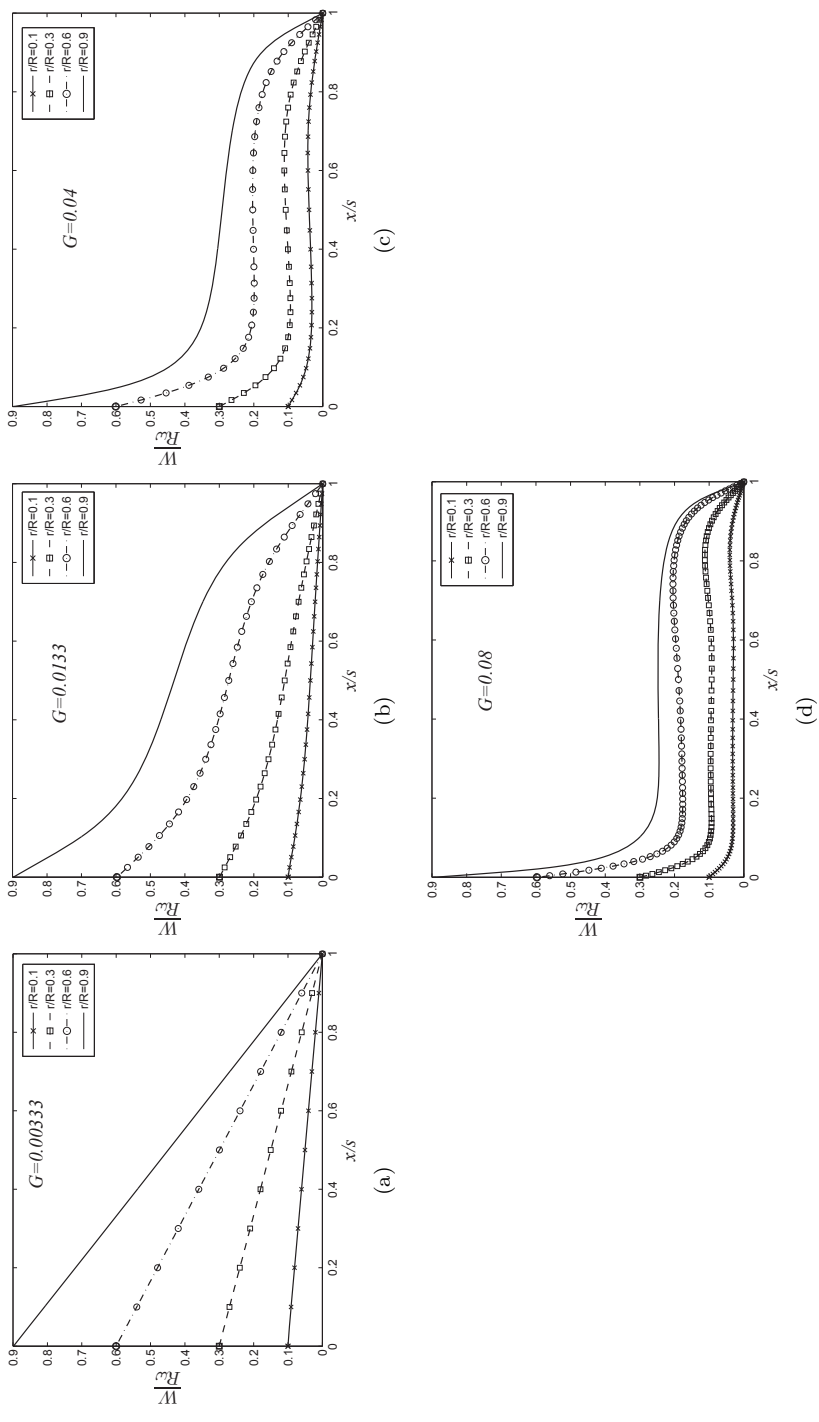

Figure 3.8: Non-dimensional tangential velocity variation across the air-gap at $Re = 1.26 \times 10^5$ for (a) G=0.00333 (b) G=0.0133 (a) G=0.04 (a) G=0.08.

3.2.2 Heat transfer characteristics in the air-gap

The temperature contour in the midplane of the geometry is illustrated in Fig. 3.9, for the case that the surface temperature of the stator, the rotor and the cover are kept at 120 °C, 100 °C and 50 °C, respectively. The coldest region is at the stagnation point at the centerline of the rotor, and the air temperature goes up at the higher radii. The magnified view in the air-gap demonstrates that the temperature drops in the periphery, due to inflow of cold air (in the vicinity to the cover with lower temperature) inside the gap region. Due to considering the natural convection, the air temperature distribution of the upper half is not completely identical to the lower half. Nevertheless, it has been found that the effect of natural convection on the overall heat transfer was negligible. This was verified by a separate calculation without taking into account the effect of gravity. Moreover, in the extreme situation of the low rotor speed (10 m/s), we have $\frac{Gr}{Re^2} = 1.9 \times 10^{-4}$, where Gr is the Grashof number. Therefore, the problem is regarded as a forced convection problem.

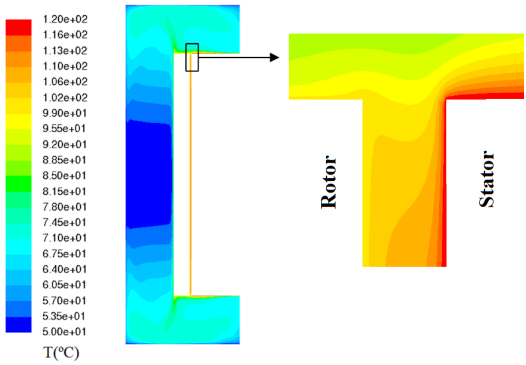

Figure 3.9: Temperature contour in the air-gap at $Re = 1.26 \times 10^5$ and $G = 0.01333$.

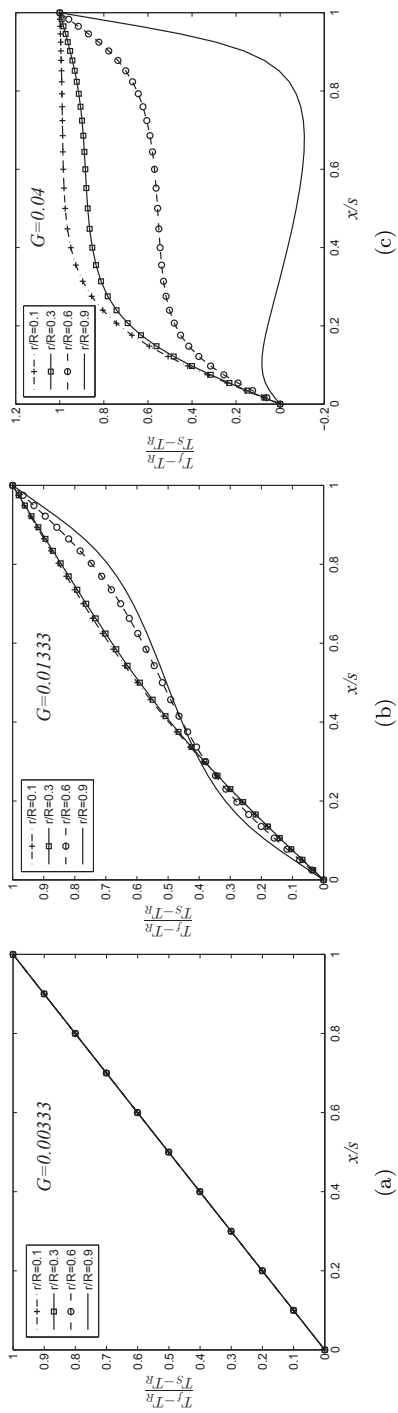

Figure 3.10: Non-dimensional temperature variation across the air-gap at $Re = 1.26 \times 10^5$ for (a) G=0.00333 (b) G=0.0133 (a) G=0.04 (a) G=0.08.

In order to better understand the temperature distribution in the air-gap, it is necessary to present the temperature profiles across this region. Fig. 3.10 depicts air temperature variations alongside the air-gap at different radii for various gap size ratios. It is seen that temperature profiles for the narrow gap ($G = 0.00333$) are relatively similar at different radii, which means that the heat transfer rate between the rotor and the stator surface in the gap is almost identical according to the slope of the profiles and that the heat transfer mechanism is mainly by axial conduction through the air-gap. For the wider gap, however, non-linear temperature distributions are observed in different radii. In line with the slope of the profiles at $x/s = 1$ which corresponds to stator heat transfer rate, it can be interpreted that the stator heat transfer in the gap is minimum in the vicinity of its center and it increases at the periphery of the air-gap (at higher radii). Furthermore, for wide gaps, the temperature at high radius can be lower than both the rotor and stator temperature (negative number of vertical axis). This is caused by cool air entering the air-gap in the radial direction.

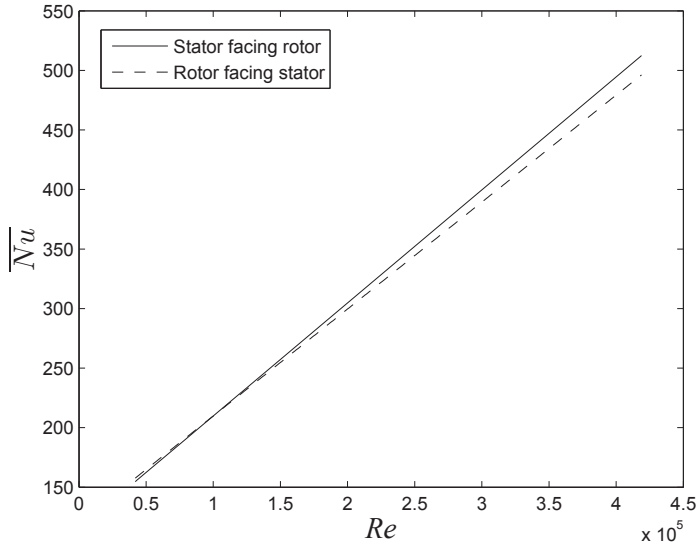

Figure 3.11: Effect of Re on the mean Nusselt number of the stator surface and the rotor surface in the air-gap at $G = 0.01333$.

Fig. 3.11 shows the effect of the Reynolds number on the mean Nusselt number ($\overline{Nu} = \frac{\overline{h}R}{k}$) for the surfaces *"Stator facing rotor"* and *"Rotor facing stator"*. For a fixed $G = 0.01333$, the mean Nusselt numbers for both surfaces increase monotonically with the Reynolds number. An increase of the Reynolds number results in more air recirculating in the gap area, which

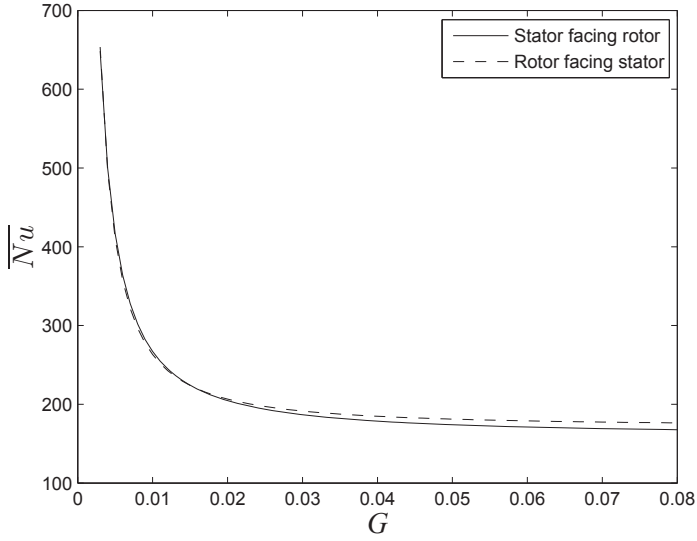

Figure 3.12: Effect of G on the mean Nusselt number of the stator surface and the rotor surface in the air-gap at $Re = 1.26 \times 10^5$.

in turn improves the convective heat transfer.

The effects of the gap size ratio on the mean Nusselt number for the surfaces *"Stator facing rotor"* and *"Rotor facing stator"* have been illustrated in Fig. 3.12 when Reynolds number is kept at 1.26×10^5. A sharp decline in the mean Nusselt number is observed as G increases up to 0.03. Once G goes up from 0.03 to 0.08, the average Nusselt number remains almost unchanged. As mentioned earlier, for the narrow gap, the flow structure is of a Couette-type flow, such that an increase in the gap size results in a decrease in temperature gradients, which consequently decreases heat transfer. By contrast, as the gap size increases further, two separate boundary layers appear on both sides of the disks in the gap, known as Batchelor flow structure. The appearance of two seperate boundary layers results in the mean Nusselt number becoming almost entirely independent of G.

3.3 Effect of the holes in the rotor disk

In this section, the influence of the holes at the rotor disk on the convective heat transfer in the current rotor-stator system is studied. The drawing of the rotor disk with the holes are depicted in the Fig. 3.13(a). The inner and outer diameter of these openings are 60 mm and 90 mm, while the diameter of the rotor is 150 mm.

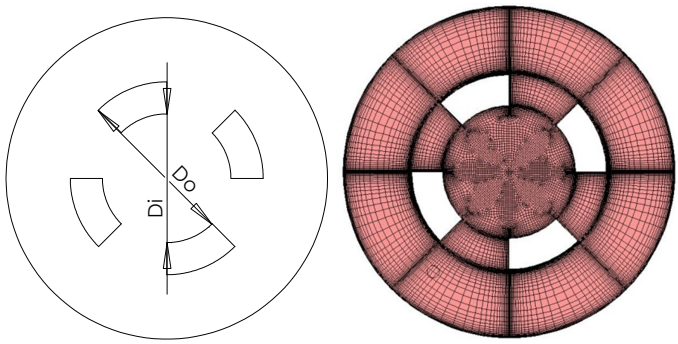

(a) (b)

Figure 3.13: (a) Drawing of the rotor disk with the holes ($D_i = 60$ mm, $D_o = 90$ mm & $D_{rotor} = 150$ mm) (b) Surface mesh of the rotor disk with the holes

CFD simulations are carried out to calculate the heat transfer and flow field. The rotor-stator interaction in this configuration has been modelled using two distinct CFD techniques including multiple reference frame (MRF) and sliding mesh (SM) methodologies. The former case involves steady state computations and produces time averaged flow field, whereas the latter one involves transient computations to produce time accurate flow field. In the MRF technique (or Frozen Rotor), the mesh remains fixed for the computation and the flow in each moving cell zone is solved using the moving reference frame equations. This is analogous to freezing the motion of the moving part in a specific position and observing the instantaneous flow field with the rotor in that position. The SM and MRF results agree for a specific position, unless there is unsteadiness in the flow or interaction between rotor and stator.

Contrary to the MRF approach, the SM method does not neglect unsteady rotor-stator interaction and it accounts for the relative motion of stationary and rotating components. In the SM method, the effect of the changing position of the holes during rotation is taken into account, which makes this method computationally demanding. The results of the flow field and the heat transfer from the MRF method are utilized as the initial solution for the transient sliding mesh calculation.

The surface mesh of the rotor disk with the holes is illustrated in Fig. 3.13(b). To check the independency of the grid size and time step, several exploratory simulations were carried out. Once the length of the first cell in the vicinity of the wall is 100 μm (with 11,586,000 number of cells) and each time step corresponds to the rotation of the rotor equal to 0.5° (time step of 2.1817×10^{-5} with 20 iterations per time step), the results are almost inde-

pendent of the grid and the time step with the error of 0.8% in predicting the stator heat transfer rate. Note that a substantial physical simulation time of $t = 1s$ (equivalent to 63 rotations) is required to get the fully periodic results of a SM simulation.

Table 3.1: Mass flow rate (kg/s) passing through the holes at $Re = 1.26 \times 10^5$ and $G = 0.01333$.

	SM method	MRF method
Net inflow	0.00021	0.00020
Net outflow	0.00021	0.00019

Table 3.1 presents the amount of air that passes into the holes and penetrates into the gap. Due to the conservation of mass, the amount of the incoming air is equal to that leaves the air-gap. A good agreement between these numerical approaches is also observed.

Table 3.2: Comparison between the results of the heat transfer rates (W) from MRF and SM methods.

Surface	SM method	MRF method
Rotor facing rotor	-5.0	-5.1
Stator facing stator	26.5	27.7

The comparisons between the results of heat transfer rates for the rotor and the stator surfaces in the gap through the MRF and the SM methods are shown in Table 3.2. According to this Table, there is a good correspondence between the results of the SM and the MRF methods in prediction of the convective heat transfer rates in this system.

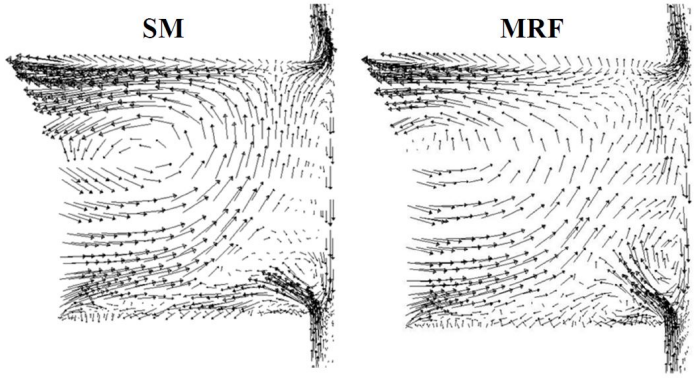

Figure 3.14: Velocity vectors inside the hole in $r - z$ plane for $Re = 1.26 \times 10^5$ and $G = 0.01333$, for the SM technique and the MRF method.

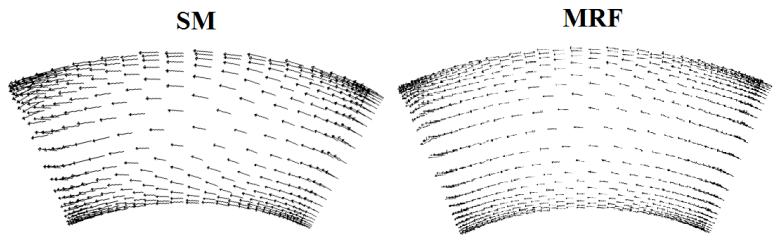

Figure 3.15: Velocity vectors inside the hole in $r-\theta$ plane for $Re = 1.26 \times 10^5$ and $G = 0.01333$, for the SM technique and the MRF method.

To give more insight into the flow pattern inside the hole, the velocity vectors for both the MRF and SM methods in a meridional plane of the rotor and also in a $r-\theta$ plane have been shown in the Figs. 3.14-3.15. The left hand side of the plot (Fig. 3.14) is where the airflow penetrates into a hole and the right side illustrates how airflow enters into the gap. As predicted by the both approaches, there is a recirculating region in the middle of the hole. More importantly, there is an excellent agreement between the results of the SM method and those obtained by the MRF method. From this, the conclusion is drawn that the results of the MRF methodology are satisfactory in the modeling of the rotor-stator interaction. Therefore, from now on, the MRF method will be employed as the numerical tools in this project instead of SM method which entails an enormous amount of computational costs. In fact, each SM simulation requires 1.3×10^4 CPU hours, while 2.3×10^3 CPU hours are needed for each MRF simulation.

Fig. 3.16 shows the velocity vectors in the air-gap region between the rotor and the stator, in order to highlight the influence of the holes in the flow field in the current configuration. The maximum radial velocity component of the airflow at the outer radial location of the air-gap is about 3 m/s. In contrast to the case without the hole, shown in Fig. 3.5, there is a strong net outflow in the air-gap. This improves the cooling of the whole system.

Fig. 3.17 clarifies the contributions of the holes at the rotor disk on the thermal performance of this discoidal arrangement. The comparison of the stator heat transfer rate between the case with and without holes reveals that the stator heat transfer rate can be substantially improved with the presence of the holes at the rotor disk. For example, the heat transfer rate almost doubles at $G = 0.01333$ and $Re = 1.26 \times 10^5$.

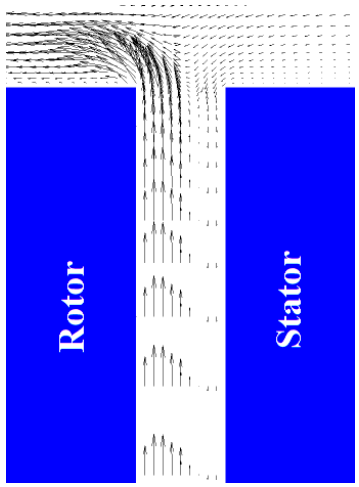

Figure 3.16: Velocity vectors in the air-gap in the presence of the holes on the rotor disk at $Re = 1.26 \times 10^5$ and $G = 0.01333$.

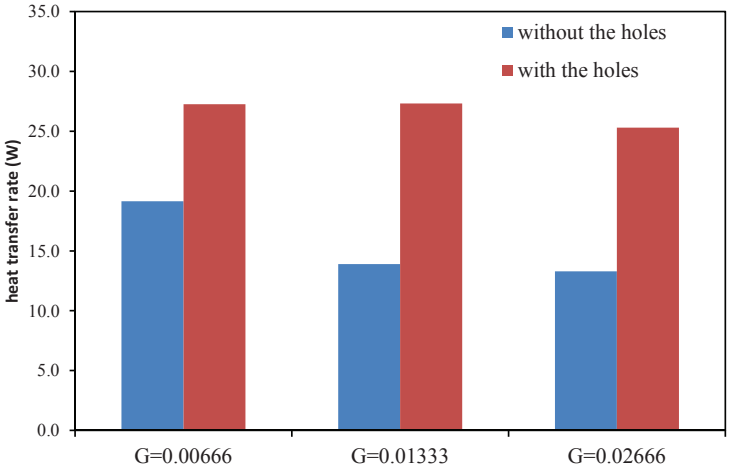

Figure 3.17: Influence of the holes in the rotor disk on the stator heat transfer in the gap for different G at $Re = 1.26 \times 10^5$.

3.4 Correlations for convective heat transfer

3.4.1 Derivation of the correlations

A correlation for the convective heat transfer in the rotor-stator system of an AFPMSM can be developed, based on CFD results. The configuration, shown in Fig. 3.18, consists of seven surfaces namely stator facing rotor,

rotor facing stator, stator sidewall, rotor sidewall, rotor facing cover, cover front side and cover sidewall. This model seeks to fully predict the average convective heat transfer of these surfaces as a function of the important parameters, including the Reynolds number, the gap size ratio, and the surface temperatures. Although it is possible to find accurate results by carrying out the 3-D CFD simulations for each case, it would definitely be computationally demanding. Consequently, having a formulation with an acceptable accuracy is of paramount importance, especially when an optimization for the complete electrical machine has to be done.

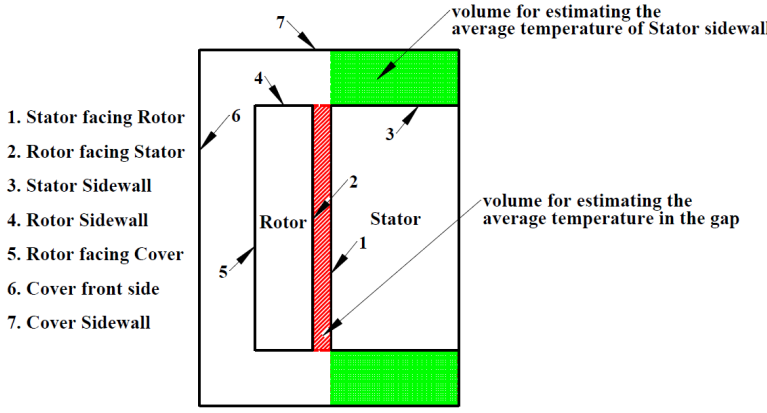

Figure 3.18: The name of each surface in the system.

The surface averaged convective heat transfer coefficient for the isothermal surface f is defined by:

$$\overline{h}_f = \frac{\overline{q}_f}{(T_{surf,f} - \overline{T}_{ref,f})} \tag{3.3}$$

where $\overline{q}_f$ is the average heat flux of the surface f, $T_{surf,f}$ is the surface temperature and $\overline{T}_{ref,f}$ is the bulk fluid temperature as the reference temperature. Moreover, the surface averaged Nusselt number for each surface can be given through the following formulation,

$$\overline{Nu}_f = \frac{\overline{h}_f \ell_f}{k} \tag{3.4}$$

where k is the thermal conductivity of air, and ℓ_f is the length scale, depending upon the surface f which is indicated in Table 3.4. In most studies in the literature, the ambient temperature was used as the reference temperature in calculation of the convection coefficients. For the gap region, it has a consequence that the convection coefficient is no longer independent

of the surface and ambient temperature. Therefore, $\overline{T}_{ref,f}$ should strictly refer to the bulk fluid temperature adjacent to the surface where the measurement for $\overline{q}_f$ is being made. In this way, the convective heat transfer coefficient becomes independent of the surface temperature and the ambient temperature, as well. The following formulation was used to assess the average bulk fluid temperature adjacent to the surface *f*:

$$\overline{T}_{ref,f} = \frac{1}{V_f} \int_{V_f} T dV \tag{3.5}$$

where V_f is the volume adjacent to the corresponding surface. $\overline{T}_{ref,f}$ is estimated by averaging the fluid temperature adjacent to each surface. For instance, the red and green volumes in Fig. 3.18 have been used to assess the average fluid temperature for the surfaces in the gap and the stator sidewall. This has been calculated through a user-defined function (UDF) in FLUENT.

The heat transfer rate from the different surfaces can be dependent on the rotor temperature, the stator temperature and/or the cover temperature. It is found that a combination of the three temperatures (instead of using e.g. ambient temperature when dealing with the heat transfer in the gap as has already been done in literature) needs to be used in the calculation of the heat transfer coefficient. Thus, it is presumed that the bulk fluid temperature can be expressed as,

$$\overline{T}_{ref,f} = a_f T_R + b_f T_S + [1 - (a_f + b_f)] T_C \tag{3.6}$$

where the subscripts *R, S, C* and *f* correspond to the rotor, the stator, the cover, and the surface for which the heat transfer is being evaluated (see Fig. 3.18). The coefficients a_f and b_f are dependent on *Re* and *G*, and are different for each surface which will be discussed later in this chapter.

The procedure of the proposed method has been depicted in the Fig. 3.19. First of all, the CFD simulations are performed when the Reynolds number and the gap size ratio are kept at the reference point ($Re = 1.26 \times 10^5$ and $G = 0.01333$) with six different combinations of T_R, T_S & T_C. In this way, the average bulk fluid temperature and the mean convective heat transfer coefficient for all surfaces in this rotor-stator configuration will be calculated.

With Eq. 3.4, values of the surface averaged $\overline{Nu}_f$ are given for each different temperature combination at the reference point. Although there is a small difference (1.9% the maximum deviation from the averaged value) between these Nusselt numbers for each temperature combination, a mean Nusselt number for each surface is computed by taking the arithmetic mean of these surface averaged $\overline{Nu}_f$. Furthermore, the six different temperature

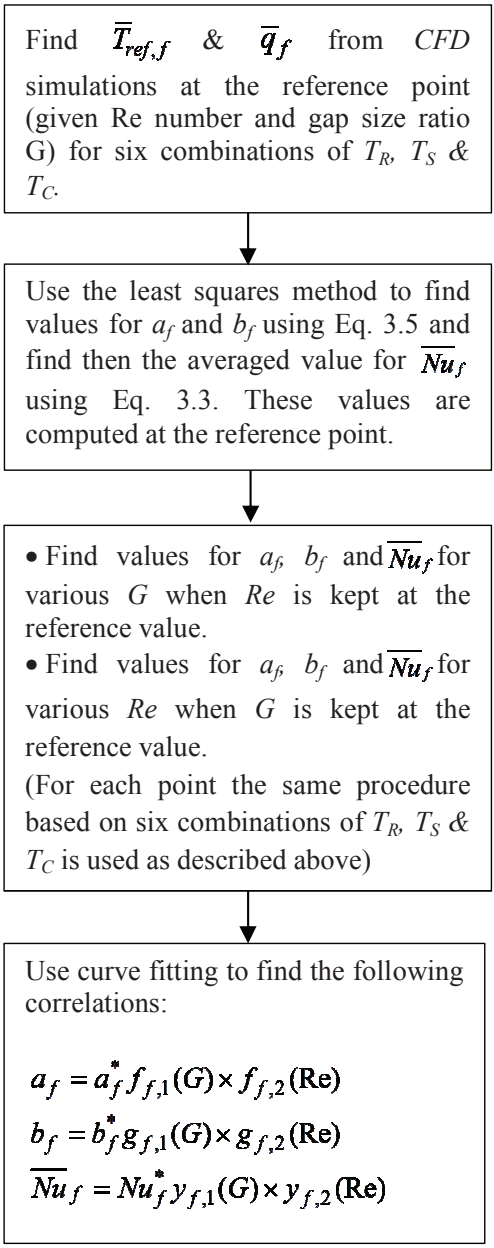

Figure 3.19: The procedure for the convective heat transfer modeling.

Table 3.3: CFD results for different surface temperature combinations and the appropriate values of a_f, b_f and $\overline{Nu}_f$ for stator surface facing rotor ($f = 1$).

Combination	T_S (°C)	T_R (°C)	T_C (°C)	T_f (°C)	a_1	b_1	$\overline{Nu}_1$
1	120	100	50	110			
2	100	80	50	90.1			
3	120	80	50	100.3	0.4829	0.5122	240.7
4	110	90	60	100.1			
5	130	110	60	120			
6	110	70	45	90.4			

combinations result in six equations of type Eq. 3.6. The least squares method is employed to this set of equations in order to find the appropriate values of a_f and b_f. By doing so, the values of a_f, b_f and $\overline{Nu}_f$ are estimated for each surface f at the reference point. The results for the reference point for the surface *"Stator facing rotor"* ($f = 1$) are shown in Table 3.3.

The variations of a_f, b_f and $\overline{Nu}_f$ with G should be known. To do so, CFD simulations are implemented for G=$\{0.00333, 0.00666, 0.02, 0.02666, 0.04, 0.08\}$ at $Re = 1.26 \times 10^5$ for different temperature combinations of the rotor, the stator and the cover. For each gap size ratio G, having the average bulk fluid temperature and the mean convective heat transfer coefficient in each surface for various temperature combinations from the CFD calculations, the least squares method once again is employed to Eq. 3.4 to estimate the values of a_f and b_f, then the mean Nusselt number for each surface is given by averaging the results of Eq. 3.4.

Equally important is the variation of the mean convective heat transfer with the Reynolds number. Thus, CFD calculations are performed for $Re = \{4.19\times10^4, 8.38\times10^4, 2.10\times10^5, 3.35\times10^5, 4.19\times10^5\}$ at fixed $G = 0.01333$ for different T_R, T_S & T_C. In a similar way, the values for a_f, b_f and $\overline{Nu}_f$ for each of these Reynolds numbers are then calculated.

Ultimately, the purpose of this approach is to find the correlations which express the variation of a_f, b_f and $\overline{Nu}_f$ with Re and G as follows,

$$\begin{aligned} a_f &= F_f\,(G, Re) \\ b_f &= G_f\,(G, Re) \\ \overline{Nu}_f &= Y_f\,(G, Re) \end{aligned} \tag{3.7}$$

It is assumed that the above functions of two variables can be written

as the product of two functions of one variable as,

$$\begin{aligned} a_f &= a_f^* f_{f,1}(G) \times f_{f,2}(Re) \\ b_f &= b_f^* g_{f,1}(G) \times g_{f,2}(Re) \\ \overline{Nu}_f &= \overline{Nu}_f^* y_{f,1}(G) \times y_{f,2}(Re) \end{aligned} \tag{3.8}$$

where the superscript $*$ refers to the values of a_f, b_f and $\overline{Nu}_f$ at the reference point. In order to find the formulations, curve fittings of the results have been used for each surface in the system. The weights were used on the reference point in the fitting process. Therefore, the fitting value of these formulas at the reference point is almost one. It turned out the linear fitting is mainly the best choice to obtain the functions. To construct the formulation for Nusselt number for surfaces in the gap, the power-law functions have been considered, which is also common in the literature. As an example, the curve fittings for the surface *"stator facing rotor"* can be found in Appendix 3.A in Fig. 3.28. The details of the formulations for all surfaces are presented in the Table 3.4.

In accordance with Eq. 3.6, as long as the sum of the coefficients a_f and b_f is close to unity, the value of the cover surface temperature, which certainly depends on the ambient temperature, has almost no effect on the bulk fluid temperature adjacent to the surface where heat transfer is measured. This phenomenon happens for the surfaces in the gap namely *"rotor facing stator"* and *"stator facing rotor"* at the actual ranges of gap sizes and Reynolds number (see Table 3.4). As a consequence, the proposed correlations to estimate the average convective heat transfer for the surfaces in the gap are independent of the ambient temperature.

Table 3.4: Correlations for the convective heat transfer prediction in each surface within the discoidal system.

Surfaces:	Stator facing rotor, $f = 1$	Rotor facing stator, $f = 2$	Stator sidewall, $f = 3$	Rotor sidewall, $f = 4$
$\ell_f(m)$	R	R	0.03	0.01
a_f^*	0.4829	0.4829	0.2585	0.2877
b_f^*	0.5122	0.5122	0.1105	0.1252
$\overline{Nu}_f^*$	240.72	243.12	48.61	13.52
$f_{f,1}$	$-7.447G + 1.071$	$-7.447G + 1.071$	$3.017G + 0.9777$	$8.711G + 0.9077$
$f_{f,2}$	$8.524 \times 10^{-8}Re + 1.018$	$8.524 \times 10^{-8}Re + 1.018$	$3.222 \times 10^{-7}Re + 0.9357$	$3.222 \times 10^{-7}Re + 0.9357$
$g_{f,1}$	$2.353G + 0.9839$	$2.353G + 0.9839$	$0.4034G + 0.9429$	$-3.266G + 1.005$
$g_{f,2}$	$3.995 \times 10^{-8}Re + 0.9912$	$3.995 \times 10^{-8}Re + 0.9912$	$-4.319 \times 10^{-7}Re + 1.107$	$-8.514 \times 10^{-7}Re + 1.142$
$y_{f,1}$	$0.001366G^{-1.26} + 0.675$	$0.0006897G^{-1.375} + 0.720$	$3.065G + 0.9684$	$-6.695G + 1.13$
$y_{f,2}$	$3.983 \times 10^{-6}Re + 0.4822$	$3.765 \times 10^{-6}Re + 0.5029$	$4.521 \times 10^{-6}Re + 0.3911$	$8.86 \times 10^{-6}Re - 0.1171$

Surfaces:	Rotor facing cover, $f = 5$	Cover front side, $f = 6$	Cover sidewall, $f = 7$
$\ell_f(m)$	R	$1.4R$	$0.4R + s + 0.04$
a_f^*	0.1464	0.2118	0.277
b_f^*	0.0382	0.0602	0.1014
$\overline{Nu}_f^*$	152.52	182.91	136.58
$f_{f,1}$	$-1.34G + 1.066$	$0.6159G + 1.059$	$2.015G + 1.06$
$f_{f,2}$	$7.306 \times 10^{-7}Re + 0.9151$	$9.235 \times 10^{-7}Re + 0.9216$	$2.738 \times 10^{-7}Re + 0.9643$
$g_{f,1}$	$-3.645G + 1.017$	$-2.198G + 0.9906$	$0.3082G + 0.8688$
$g_{f,2}$	$1.784 \times 10^{-7}Re + 0.9521$	$-3.423 \times 10^{-7}Re + 1.02$	$-3.209 \times 10^{-7}Re + 1.059$
$y_{f,1}$	$-0.3613G + 1.012$	$0.8755G + 0.9922$	$3.0142G + 0.9559$
$y_{f,2}$	$5.449 \times 10^{-6}Re + 0.2956$	$4.72 \times 10^{-6}Re + 0.3663$	$4.541 \times 10^{-6}Re + 0.3873$

3.4.2 Reliability of the proposed correlations

Here, the robustness of the proposed modeling has been examined. As explained before, the correlations have been obtained when, for example, the Reynolds number is fixed at a reference point while varying the gap size ratio, and vice versa. As a result, it is necessary to compare the results with the CFD simulations in the values of Reynolds numbers and gap size ratios where the curve fitting was not performed; i.e. neither Re nor G is in the reference point.

Table 3.5, therefore, shows the comparison between the proposed correlations and the CFD simulations for two cases namely $Re = 1.68 \times 10^5$, $G = 0.01$ and $Re = 8.38 \times 10^4$, $G = 0.02$ with different surface temperatures. From this Table, it can be seen that the proposed correlations are capable of predicting the surface heat transfer rate in each surface as well as the mean fluid temperature adjacent to each surface with an appropriate accuracy (5% average deviation of the total stator heat transfer rate). Note that the positive values of the heat transfer correspond to the direction of heat transfer from surface to fluid, whereas the negative values indicate the direction of heat transfer from fluid to surface. Moreover, it is clear that the mean fluid temperature is different from one another, no matter if the surfaces have the same temperature. For example, the surface temperatures of the rotor's components namely *"Rotor facing stator"*, *"Rotor sidewall"* and *"Rotor facing cover"* are the same. Nevertheless, the values of the mean fluid temperature are not identical. Also, the average convective heat transfer coefficient is no longer dependent on the surface temperature.

Table 3.5: Comparison of the CFD and the proposed correlations results for heat transfer rate (W) and average bulk fluid temperature (°C) adjacent to each surface. Positive values represent the heat transfer direction from the surface to the fluid.

Surfaces	For $Re = 8.38 \times 10^4$ and $G = 0.02$ $T_S = 100$ °C, $T_R = 80$ °C & $T_C = 50$ °C				For $Re = 1.68 \times 10^5$ and $G = 0.01$ $T_S = 120$ °C, $T_R = 100$ °C & $T_C = 50$ °C			
	Proposed correlations		CFD		Proposed correlations		CFD	
	$\dot{Q}$(W)	T_f (°C)	$\dot{Q}$(W)	T_f (°C)	$\dot{Q}$(W)	T_f (°C)	$\dot{Q}$(W)	T_f (°C)
Stator facing rotor	6.6	89.7	6.2	90.3	23.3	110.2	24.9	110.0
Rotor facing stator	-6.4	89.7	-6.5	90.3	-23.6	110.2	-24.7	110.0
Stator sidewall	10.7	63.3	13.2	63	42.0	70.5	38.5	71.2
Rotor sidewall	1.0	65.3	2.1	64.8	8.1	72.7	7.1	73.3
Rotor facing cover	10.4	56.2	10.5	55.9	55.7	60.5	58.9	60.2
Cover front side	-7.2	59.6	-7.0	59.3	-36.2	66.0	-36.7	65.3
Cover sidewall	-15.4	63.6	-18.5	63.2	-70.2	71.3	-68	71.2

3.4.3 Importance of the reference temperature

In all YASA disk type electrical machines, the heat transfer direction is usually from the stator to the two rotors, as the stator has higher losses and the disk-shaped rotors have a large cooling surface. Hence, it is expected that the core fluid temperature is lower than the stator surface temperature.

Fig. 3.20 shows the variations of core fluid temperature in the gap for different gap size ratios and Reynolds numbers. The same trend reported by Howey et al. [135] is seen here. Specifically, the core fluid in the air-gap cools down as the gap size increases. This is because the wider gap allows the cold air to penetrate into the gap and it decreases the core fluid temperature accordingly. Also, the core fluid temperature cools down slightly with the Reynolds number in the narrow gap size $G \leq 0.04$, whereas the opposite trend is observed for the wider gap sizes.

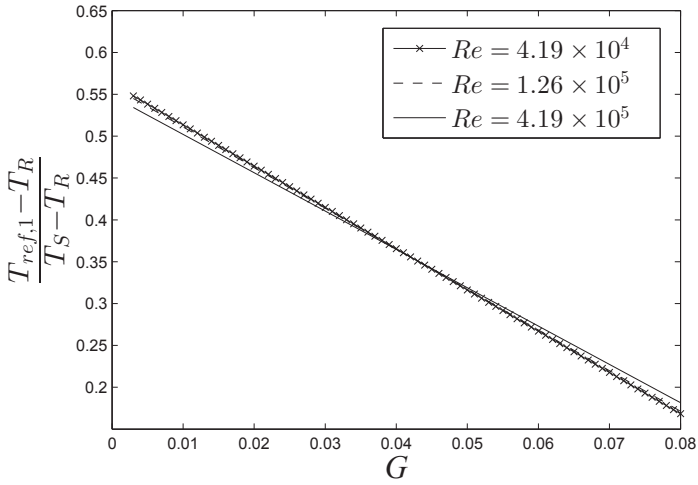

Figure 3.20: Non-dimensional mean fluid temperature in the gap versus G for different Re numbers when $T_S = 120°\text{C}$, $T_R = 100°\text{C}$ & $T_C = 50°\text{C}$.

Figs. 3.21-3.22 demonstrate the variations of the mean Nusselt number and the average heat transfer from the surface *"Stator facing rotor"* in the gap versus G at different Re numbers. There is a sharp decline for both the mean Nusselt number and the average heat transfer rate as G increases up to 0.02 (narrow gap size). The reason for this trend is that the temperature variations are almost linear across the air-gap for the narrow gap sizes (see Fig. 3.10(a)). Therefore, an increase in the gap size leads to the smaller temperature gradients, which consequently decreases heat transfer rate for the surfaces in the gap. As the gap size enlarges further, the values of the mean Nusselt number remain constant for all Reynolds

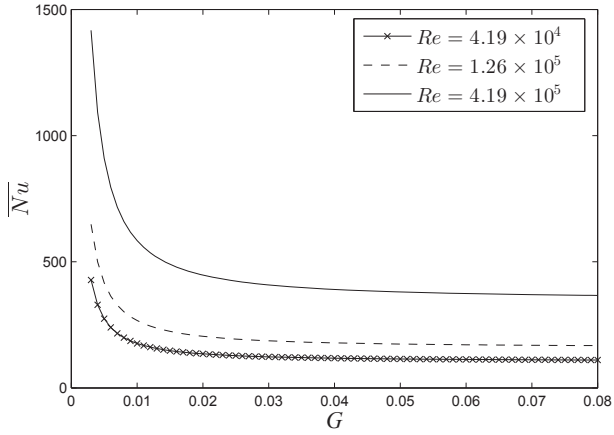

Figure 3.21: Mean Nusselt number of the stator surface in the gap versus G for different Re numbers.

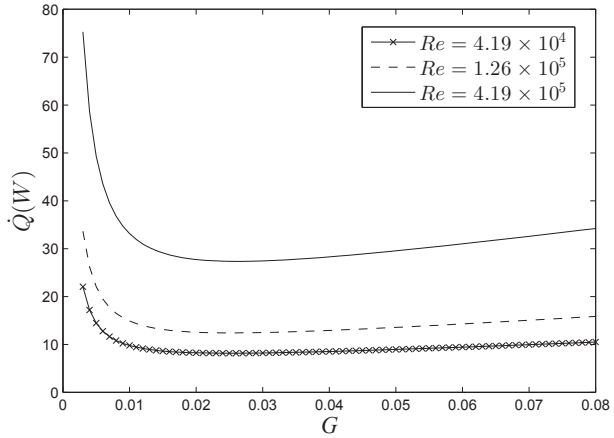

Figure 3.22: Average convective heat transfer rate of the stator surface in the gap versus G for different Re numbers when $R = 75$mm, $T_S = 120°$C, $T_R = 100°$C & $T_C = 50°$C.

numbers. By contrast, there is a slight growth in the average convective heat transfer on the stator surface (when $R = 75$ mm, $T_S = 120°$C, $T_R = 100°$C & $T_C = 50°$C). This implies that there exists an air-gap size for which the convective heat transfer on the surface *"Stator facing rotor"* reaches a minimum.

At a first glance, this may seem to be incompatible with the results given by Yuan et al. [131] who observed a local maximum for the heat transfer rate as a function of the air-gap size. To interpret this inconsistency, the

attention should be given to a difference between the flow patterns in the air-gap. The flow structure here is basically either a Couette-type flow or Batchelor flow structure, while in the study reported by Yuan et al. [131] an open discoidal system with the wide air-gap size was studied. In open systems, i.e. without enclosure, Stewartson type flow occurs, which is characterized by the absence of a rotating fluid core. Moreover, by only considering the mean Nusselt number variations, one may conclude that the convective heat transfer remains unchanged as the gaps size goes up from 0.02 to 0.08 (see Fig. 3.21). In reality, however, the core fluid temperature becomes colder and it results in an increase in the convective heat transfer rate. The possible implication is that knowing the core fluid temperature variations in the air-gap is vital in evaluating the convective heat transfer of the stator surface in the gap.

3.4.4 Variation of viscosity and thermal conductivity with temperature

The proposed correlations are using non-dimensional numbers. In order to build the correlations, different cases were run. The parameters for these cases were chosen to be representative for the operation of an electrical machine running in an air environment. Consequently, values for the viscosity were chosen to correspond with those for air in the expected temperature range. In order to check the validity of this approach, we have simulated a case in which the viscosity varies with temperature through Sutherland's viscosity law as,

$$\mu = \mu_0 \left(\frac{T}{T_0}\right)^{3/2} \frac{T_0 + C}{T + C} \tag{3.9}$$

where C corresponds to a Sutherland constant of 110 K, $T_0 = 273$ K, $\mu_0 = 1.716 \times 10^{-5}$ kg/(m.s). The Prandtl number in the temperature range between 50 °C and 120 °C differs by at most 1.5% from 0.7. It was therefore kept constant at 0.7 which defines the variation of the thermal conductivity with temperature. We call this: case *"Sutherland"*, and compare it with the case where constant values for viscosity and thermal conductivity are considered: case *"fixed"*.

For both cases, the tip velocity of the rotor is 30 m/s, and the surface temperatures of the stator, the rotor and the cover are kept at 120°C, 80°C & 50°C, respectively. The heat transfer rate of different surfaces are compared. Note that the Reynolds number is different for both cases since the viscosity for the case *"Sutherland"* is considered at the mean fluid temperature adjacent to the surfaces under study. For example, for the

Table 3.6: Comparison of the CFD and the proposed correlations results for heat transfer rate (W) for Case *"Sutherland"* and Case *"fixed"* when $G = 0.01333$, $T_S = 120°C$, $T_R = 80°C$ & $T_C = 50°C$.

Surfaces	Case "*Sutherland*"		Case "*fixed*"	
	Proposed correlation	CFD	Proposed correlation	CFD
Stator facing rotor	29.7	30.3	26.1	26.7
Rotor facing stator	-31.1	-31.9	-27.1	-28
Stator sidewall	32.9	33.1	29.3	31.1
Rotor sidewall	2.2	-0.3	2.0	0.1
Rotor facing cover	22.2	21.7	19.6	21.7
Cover front side	-17.5	-16.8	-15.5	-15.8
Cover sidewall	-36.8	-36.2	-31.9	-33.4

surfaces in the gap it would be 100°C. For the case *"fixed"*, however, the air properties have been evaluated at 50°C. The thermal conductivity for both cases is also different. For this reason, the CFD results will be different but also the proposed correlation will predict different results.

Table 3.6 shows the comparison between the CFD and proposed correlation results of convective heat transfer for case *"Sutherland"* and case *"fixed"*. It is seen that for both cases the proposed correlation can accurately predict the heat transfer rate for the different surfaces. Consequently, also if the variation of viscosity and thermal conductivity with temperature has to be considered, taking into account the influence on the Reynolds number, the proposed correlation is capable of predicting the convective heat transfer in the current discoidal configuration.

3.4.5 Comparison to the studies in the literature

To check the validity of our proposed correlations, a comparison has been made with the experimental results of the available data in the literature, shown in Fig. 3.23. Since the reference fluid temperature in our case is different than their test runs, the comparison is made on the basis of the heat transfer rate instead of the Nusselt number. Specifically, the values for the surface *"Stator facing rotor"* are compared. For the case of $G = 0.0976$ and $Re = 3.33 \times 10^5$, an agreement (with 30% deviation) can be observed between our result and Yuan et al. [131], where extrapolation has been done for this high value of G. In addition to that, the comparison has been made between the proposed model and the experimental study by Howey et al. [135] for $G = 0.01$ at $Re = 1.1 \times 10^5$, 1.47×10^5 & 1.85×10^5. The trends are similar; however, the proposed method underestimates the heat transfer

on the surface *"Stator facing rotor"*. The main reason for this discrepancy is that the study zone to assess the mean Nusselt number in the experiment by Howey et al. [135] lies in the range of $0.6 \leq r/R \leq 1$, whereas the entire stator disk is considered in the thermal modeling presented in this chapter. In fact, heat transfer from the stator surface in the gap mainly occurs at the higher radii. This can be seen from the slope of temperature profiles in the gap as discussed in Fig. 3.10. On the other hand, there is a central admission of air without an imposing airflow at the stator in the measured values by Howey et al. [135], while our case the stator is without central opening. The presence of the central opening in the stator is advantageous to the stator heat transfer, as discussed by Boutarfa and Harmand [117]. As a consequence, the results of the proposed correlation in this chapter underestimate the stator heat transfer prediction as compared to the experimental data in the literature.

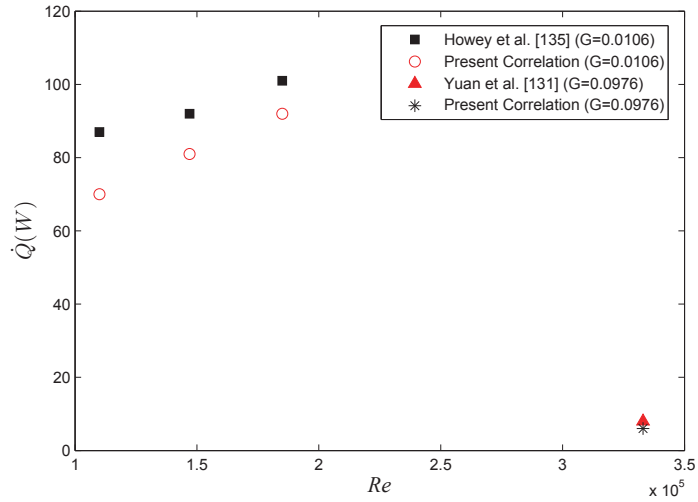

Figure 3.23: Comparison of the proposed correlations results for the heat transfer rate from stator surface in the gap with the literature.

3.5 Correlations for windage power losses

This section deals with the calculation of the losses due to friction between air and the rotor, so-called windage losses, in the current discoidal configuration. Table 3.7 shows the comparison between windage losses and other types of losses in the AFPMSM under investigation. According to this Table, the windage losses in the AFPMSM become very important at

Table 3.7: Comparison between the losses in the AFPMSM.

Rotational speed (rpm)	Windage losses	iron losses	copper losses	PM losses
2000	1.4	40	100	10
4000	11.3	100	100	20

high speed applications. These losses can be determined by semi-empirical analytical equations.

As seen in Fig. 3.18, the rotor comprises of three surfaces namely *"Rotor facing stator"*, *"Rotor sidewall"* and *"Rotor facing cover"*. The objective is to find a correlation between the power associated with the drag torque of the rotor on the one hand and the Reynolds number and the gap size ratio on the other hand, for each of these surfaces.

Similar to the procedure to find correlations for the convective heat transfer, CFD simulations are performed when the Reynolds number is kept at the reference point, while the gap size ratio is subjected to change, and vice versa. For the case of the convective heat transfer rate, the variations of the fluid properties, e.g., thermal conductivity and the viscosity with temperature were found to be insignificant in the considered temperature range. However, for windage losses evaluation, the influence of the temperature on the air properties is taken into consideration. The viscosity is related to temperature by Sutherland's viscosity law. The non-dimensional friction losses, $P_f^{'}$, for the surface f are defined as,

$$P_f^{'} = \frac{P_f}{\mu\omega^2 R^3} \tag{3.10}$$

where the subscript f corresponds to the surface for which the friction loss is calculated. The goal is then to find the correlations which express the variation of $P_f^{'}$ with Re and G as,

$$P_f^{'} = L_f(G, Re) \tag{3.11}$$

The above function of two variables can be written as the product of two functions of one variable as,

$$P_f^{'} = P_f^{'*} l_{f,1}(G) \times l_{f,2}(Re) \tag{3.12}$$

where the superscript $*$ refers to the values of $P_f^{'}$ at the reference point for the surface *f*. The fitting values of these formulas at the reference point is close to one. The curve fittings of the results have been performed for each surface of the rotor. The details of the formulation for the rotor surfaces are given in the Table 3.8.

Table 3.8: Correlations for windage losses estimation in each surface within the current discoidal system.

Surfaces:	Rotor facing stator, $f = 2$	Rotor sidewall, $f = 4$	Rotor facing cover, $f = 5$
$P_f^{'}$	222.47	153.68	295.19
$l_{f,1}$	$6.041 \times 10^{-7} G^{-2.538} + 5.428G + 0.901$	$0.4743G^{-0.157}$	1
$l_{f,2}$	$5.025 \times 10^{-6} Re + 0.4391$	$6.213 \times 10^{-6} Re + 0.2908$	$5.517 \times 10^{-6} Re + 0.3797$

Fig. 3.24 indicates the variation of friction losses for the surface *"Rotor facing stator"* versus the gap size ratio at different Reynolds numbers. There is a sharp drop in the windage losses, as G increases to about 0.01. This is because for narrow gap sizes the boundary layers of the rotor and the stator are merged. An increase in the gap size therefore results in the tangential velocity gradient to decrease and lowering the shear stress on the rotor and the frictional losses accordingly. In contrast, the windage losses increase slightly when G increases further. This is more noticeable at higher Reynolds numbers. The minimum in the frictional losses appears due to transition from the Couette-type of flow (narrow gap) to the Batchelor flow (wide gap) with unmerged boundary layers on the disks. The same phenomenon was reported by Daily and Nece [89]. When the Reynolds number increases, the minimum windage losses occur at the higher gap size ratio.

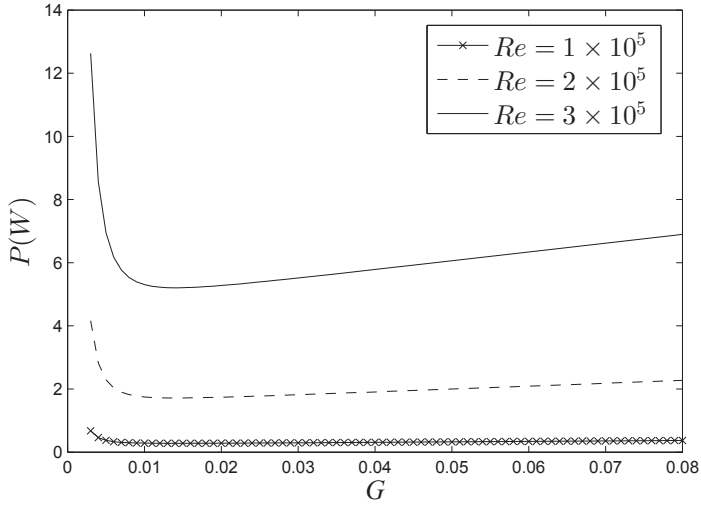

Figure 3.24: windage losses variations for the rotor surface in the gap versus G when $R = 75$ mm.

Table 3.9: Comparison of the CFD and proposed correlations results for windage losses (W) at rotor surfaces within the discoidal system.

Surface	$Re = 7.16 \times 10^4$, $G = 0.02$		$Re = 1.43 \times 10^5$, $G = 0.01$	
	Proposed Correlations	CFD	Proposed Correlations	CFD
Rotor facing stator	0.19	0.18	0.69	0.75
Rotor facing cover	0.23	0.23	0.54	0.58
Rotor sidewall	0.10	0.16	0.36	0.31

3.5.1 Correctness of the correlations for the windage losses

In the same manner as explained for the convective heat transfer coefficient modeling, the results of the correlations for the windage losses at the rotor surfaces are compared with the CFD results for the cases that Re and G are not at the reference point. Table 3.9 shows these comparisons at $Re = 1.68 \times 10^5$, $G = 0.01$ and $Re = 8.38 \times 10^4$, $G = 0.02$. It is concluded from this table that the correlations for the windage losses are quite trustworthy with the engineering accuracy (4% average of deviation from the overall windage losses.)

In the limit of a very narrow gap size, Couette flow is recovered. An analytical solution for the windage loss exists for this case (with the assumption of a linear shear stress with the rotor radius), which is given by Eq. (3.13).

$$P = \frac{\pi \mu \omega^2 R^4}{2s} \tag{3.13}$$

The accuracy of the correlations has been further verified with the results of the above equation together with the data reported by Daily and Nece [89] at $Re = 1.07 \times 10^5$. In Table 3.10, the results of the correlations are compared with the narrow gap formulation at $G = 0.0033$ and good agreement can be seen. Also, the results agree well with the empirical equation given by Daily and Nece [89] at $G = 0.013$. These comparisons demonstrate the efficacy of the correlations for the windage losses for the rotor surface in the air-gap of the current discoidal arrangement presented in this chapter.

Table 3.10: Comparison of the results for Mechanical losses (W) at rotor surface in the gap when $Re = 1.07 \times 10^5$.

G	Proposed correlations	Narrow gap formulation	Daily and Nece [89]
0.0033	0.70	0.71	-
0.0133	0.35	-	0.36

3.6 Application to the coupled electromagnetic and thermal analysis [2]

In order to find out the temperature distribution inside the rotor and the stator, both Navier Stokes and thermal conduction equations have to be solved. Typically, a transient 3-D model solves these equations simultaneously, considering the conjugate heat transfer. However, this requires huge amount of computational costs, which it is a serious drawback.

Alternatively, the proposed correlations in this chapter can be considered as the boundary conditions to the energy equation in the solid parts of the machine. The electromagnetic losses in the machine are included into the model as the source terms for the energy equation in the solid parts. The advantage of this 3-D coupled electromagnetic and thermal modeling representing a segment of the stator and the rotor is a detailed temperature distribution in the different parts of the machine, which is less present while other approaches including 2-D FEM approximations [34], analytical equation [138] or lumped parameter models [64, 62] are employed.

3.6.1 Electromagnetic modeling

The multilayer 2-D FEM technique was used for the electromagnetic analysis [139]. With respect to the coupled electromagnetic and thermal modeling, the calculation of the different power losses in the machine is the key point. These electromagnetic power losses will be the energy sources in the thermal model. In this analysis, the losses in the stator cores, the winding, and the PMs are considered. This methodology was also employed to simulate the flux density distribution in the stator cores as a function of the rotor position. Afterwards, this flux density pattern was considered to calculate the core losses using the principles of loss separation [140]. The detailed calculation of the eddy current losses in the PMs was carried out for this prototype machine by A. Hemeida [5].

[2] This section is based on the journal paper: H. Vansompel, A. Rasekh, A. Hemeida, J. Vierendeels and P. Sergeant, "Coupled Electromagnetic and Thermal Analysis of an Axial Flux PM Machine" IEEE Transactions on Magnets, 51(11):8108104, 2015

As the thermal time constant is much larger than the electric one, the time averaged values of the electromagnetic power losses have been utilized as source terms in the thermal model.

3.6.2 Coupled electromagnetic model and convective heat transfer correlations

The key point in the thermal modeling is the introduction of the correlations for the convective heat transfer coefficients in disk-type electrical machines, which are developed in this chapter. To this end, the formulations in Table 3.4 are considered as the thermal boundary conditions for the rotor and the stator surfaces. Note that due to thermal periodicity, only one segment of the rotor and the stator is modeled. The principle of this approach is elaborately explained in the PhD thesis of A. Hemeida [5].

In order to perform the transient simulations on the stator and the rotor model, the following equation inside both the parts should be solved:

$$\rho_j c_{p,j} \frac{\partial T}{\partial t} + \nabla.(-k_j \nabla T) = q_j \tag{3.14}$$

where the subscript j denotes to the different materials used in the machine and q_j is the volumetric heat generation rate associated with the electromagnetic losses. It should be mentioned that the anisotropy of the laminated silicon steel stator cores and windings is included by specifying a tensor for the thermal conductivity rather than a scalar value. In addition, the temperature dependence of the electromagnetic losses, e.g., the temperature-dependent stator resistance, taken into account. In this approach, the model for the rotor and the stator is separated. The convective heat transfer coefficients from the proposed correlations are considered as the boundary conditions for each disk. The energy equations for the rotor and the stator disk are solved with initial guess of $T_R = T_S = T_\infty$. The resulting temperature distribution at the stator and the rotor surface is used to calculate the reference temperatures. This procedure is repeated until the temperature profile stabilizes and reaches to the steady state condition.

The contours of the steady state temperature inside the rotor and the stator disk are demonstrated in the Figs. 3.25-3.26.

Here, the huge temperature gradient over the epoxy compound in the stator and the rotor is clearly visible. As a consequence, the heat generated in the stator cores of the machine is evacuated radially through the machine winding and axially by conductive flux from the stator cores to the air-gap where convective cooling from the stator to the rotor occurs. Despite the heat flux toward the rotor, good convective heat transfer at the backplane of the rotor results in a limited temperature of the PMs.

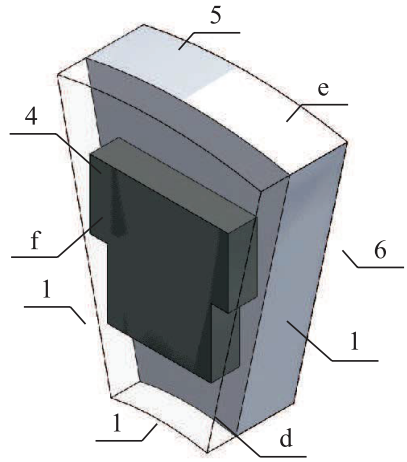

(a)

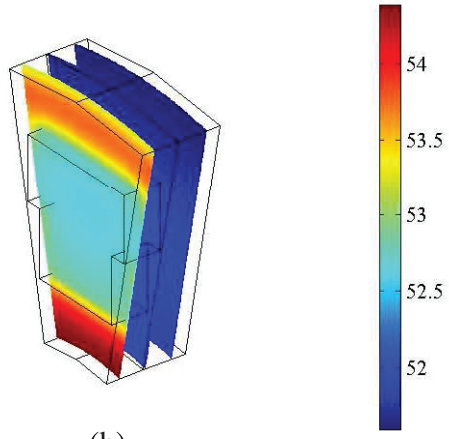

(b)

Figure 3.25: Thermal model of the rotor. (a) Rotor segment model. (b) Steady-state temperature distribution (°C), at no load and T_{amb} = 23°C. Boundary conditions: 1) thermal insulation; 4) convective heat flux rotor facing stator; 5) convective heat flux rotor edge; and 6) convective heat flux rotor backside. Subdomain materials: d) epoxy compound; e) cast steel; and f) NdFeB [14].

To illustrate the possibilities of the coupled model, the influence of the rotational speed on the temperatures in the machine at no load is depicted in Fig. 3.27. A variation of the rotational speed has a direct influence on the rotational Reynolds number. By consequence, it has an influence on

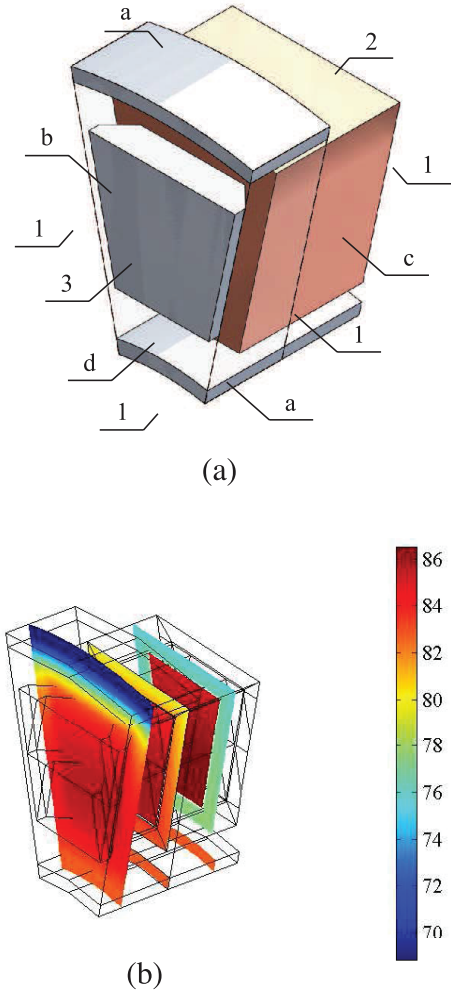

Figure 3.26: Thermal model of the stator. (a) Stator segment model. (b) Steady-state temperature distribution (°C), at no load and $T_{amb} = 23$°C. Boundary conditions: 1) thermal insulation; 2) convective heat flux stator housing; and 3) convective heat flux stator facing rotor. Subdomain materials: a) aluminum; b) laminated silicon steel; c) copper winding; and d) epoxy compound [14].

the bulk mean temperature and the Nusselt number according to the correlations. Even though an increasing rotational speed results in increasing convective heat coefficients in the air-gap and at the rotor backside, its corresponding higher electromagnetic frequency will result in increasing core

losses in the stator cores as well. In Fig. 3.27, the temperatures in the different parts of the machine resulting from the coupled electromagnetic and thermal analysis are presented for a speed range from 0 to 2500 rpm.

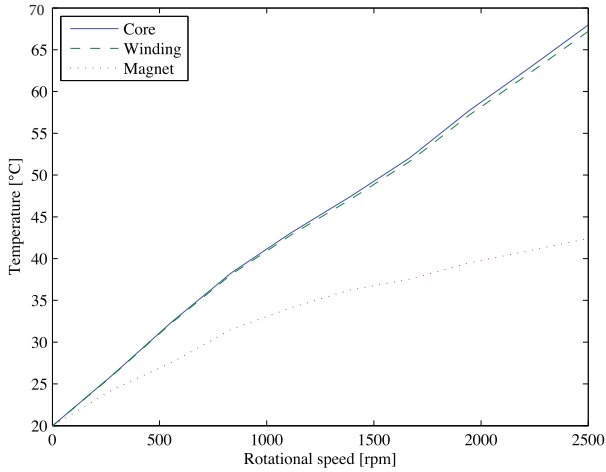

Figure 3.27: Influence of rotational speed on the temperature in the different parts of the machine evaluated at no load [14].

Temperature differences between stator cores and windings are negligible due to the good thermal contact and the high thermal conductivity of both materials. The temperatures in the magnets are significantly lower than those of the stator, which is a result of their direct mounting on the rotor disks, which are well cooled by convection.

3.7 Conclusion

This chapter presented a novel approach that can accurately estimate the convective heat transfer in the simplified discoidal system of disk-type electrical machines. This model has been constructed based on the CFD simulations in the practical range of the rotational Reynolds number $4.19 \times 10^4 \leq Re \leq 4.19 \times 10^5$ and the gap size ratio $0.00333 \leq G \leq 0.08$. Given the rotational Reynolds number, the gap size ratio as well as the surface temperature of the stator, the rotor, and the cover, the proposed model was able to fully predict the mean Nusselt number for all the surfaces and the power associated with the resisting drag torque of the rotor surfaces. The results were compared with the data in the literature and good agreement was found. The results revealed that small gap size ratios improve the average heat transfer rate on the stator surface in the gap. This finding

could also be important since the small gap size ratios generally enhance the electromagnetic properties of electrical machines.

The influence of the predominant parameters, including the rotational Reynolds number and the gap size ratio, on the fluid structure and convective heat transfer in the simple rotor-stator system of AFPMSMs was studied. It was concluded that there is a gap size ratio for a given Reynolds number for which the average convective heat transfer on the stator surface in the gap reaches a minimum. Furthermore, the presence of the holes at the rotor disk was advantageous to the stator heat transfer in the gap region as the airflow was allowed to enter into the air-gap through the holes, resulting in a net radial flow in between the rotor and stator.

Additionally, the idea of considering the bulk fluid temperature in the gap as the reference temperature to calculate the mean Nusselt number was discussed. By doing so, the proposed correlations for the convective heat transfer coefficient for the surfaces in the gap have become independent of the surface and ambient temperatures. In order to predict the bulk fluid temperature, a linear correlation between the surface temperature of the rotor, the stator and the cover was found to work well. The unknown coefficients of this equation were given by the least squares method. Moreover, it was found that the variations of the mean Nusselt number and the bulk fluid temperature are equally important to assess the heat transfer rate on the stator surface in the gap.

The applications of the proposed correlations in a coupled thermal and electromagnetic analysis were elaborately discussed. It was shown that the correlations can be used as boundary conditions to simulate the solid segments of the machine. In this way, the temperature distribution inside the material within the machine can be determined. It was indicated that the simulation time has strongly been reduced compared with fully coupled transient 3-D simulations.

To sum up, it can be concluded that the correlations presented in this chapter are quite efficient tools, not only for the thermal performance assessment, but also in windage losses modeling of the disk-type electrical machines.

3.A Appendix: Curve fitting to find the correlations for the convective heat transfer

The graphical illustrations of the curve fitting to achieve the correlations for the bulk fluid temperature along with the convective heat transfer coefficient on the surface *"Stator facing rotor"* are presented in Fig. 3.28.

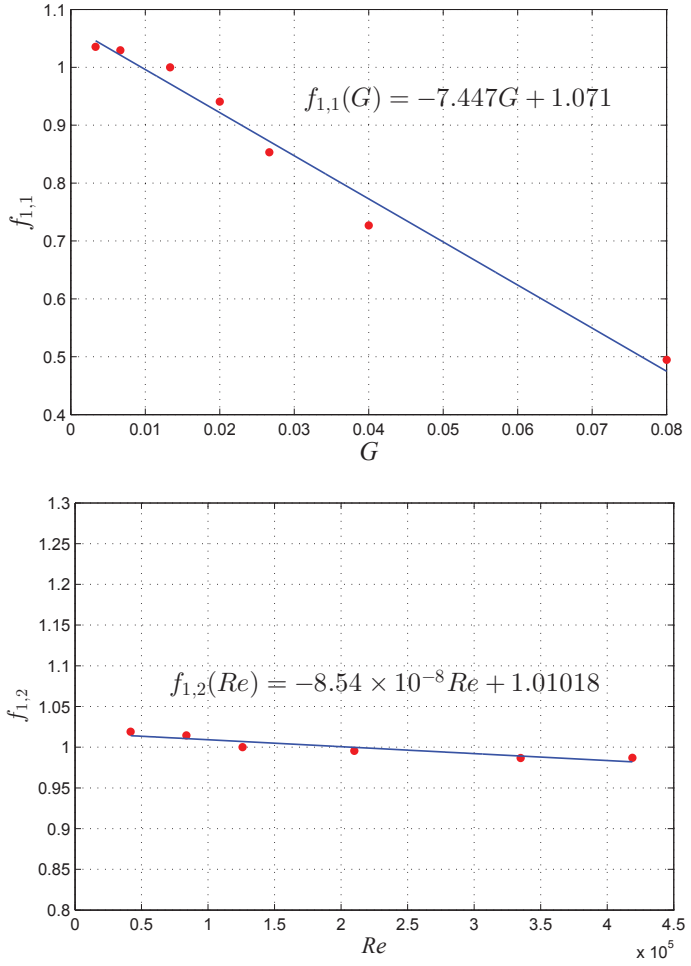

Figure 3.28: Curve fitting for the surface *"Stator facing rotor"* ($R^2 = 0.9822$ and $R^2 = 0.8534$, respectively.)

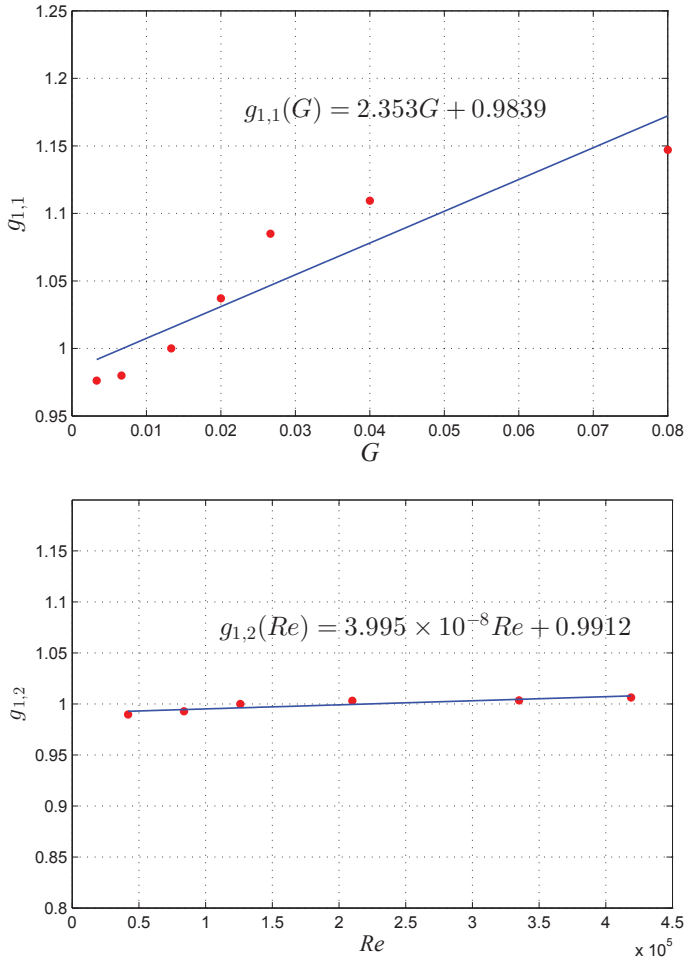

Figure 3.28: Curve fitting for the surface *"Stator facing rotor"* (cont). ($R^2 = 0.8535$ and $R^2 = 0.8015$, respectively.)

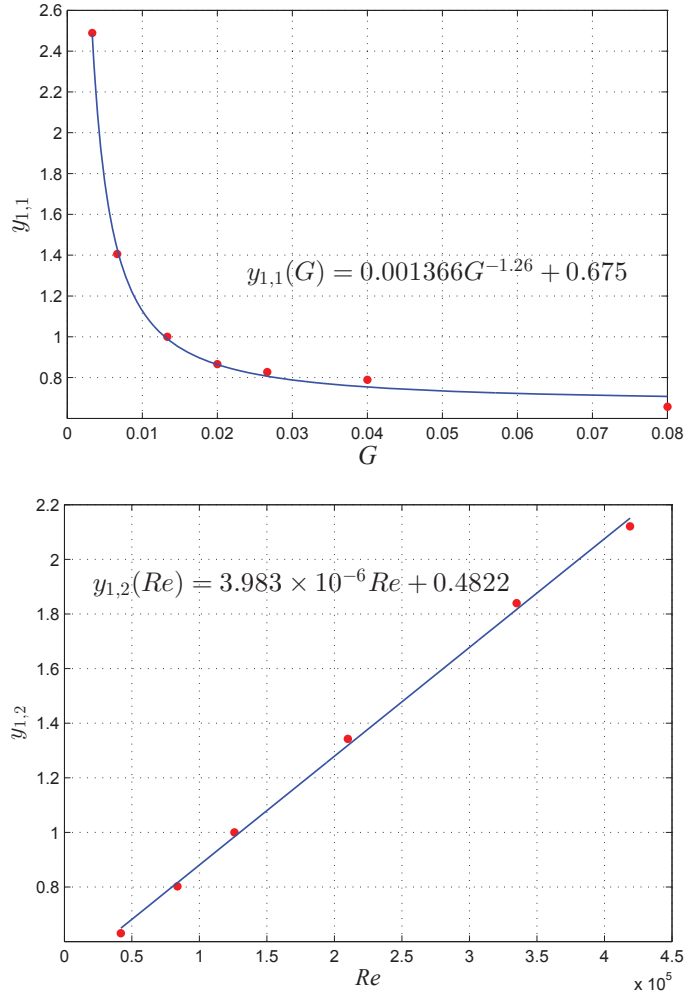

Figure 3.28: Curve fitting for the surface *"Stator facing rotor"*.($R^2 = 0.9979$ and $R^2 = 0.9984$, respectively.)

4

Convective heat transfer modeling in an AFPMSM [1]

The rudimentary discoidal arrangement of an AFPMSM has been discussed in Chapter 3. It was shown that the air-gap region critically affects the thermal performance of the disk-type electrical machines, because a large part of the heat transfer rate required to compensate the stator heat gains occurs through the air-gap. This finding makes the further study on the convective heat transfer in the real configuration of the machine absolutely essential.

Within this in mind, the present chapter elaborates the numerical modeling of the rotor-stator system with the presence of the magnets on the rotor disk. This assembly resembles the real configuration of the YASA topology of an AFPMSM. The objective is to formulate the convective heat transfer coefficients according to the governing geometrical and physical parameters in the system. Once again, it is vital to express the correlations in such a way that the heat transfer coefficients become independent of the surface temperatures. Furthermore, the influence of the geometrical parameters of the magnets, the air-gap distance as well as the rotational speed of the rotor on the flow field and the overall heat transfer rates are investigated.

[1] This chapter is written based on the journal paper: A. Rasekh, P. Sergeant and J. Vierendeels, "Fully predictive heat transfer coefficient modeling of an axial flux permanent magnet synchronous machine with geometrical parameters of the magnets" Journal of Applied Thermal Engineering, 110:1343–1357, 2017.

Based on the CFD results, the correlations for the mean Nusselt numbers of the different surfaces within the machine are constructed. Details of the proposed method and the results are discussed in the following sections.

4.1 Problem description and CFD set-up

Fig. 4.1 depicts the schematic diagram of the rotor-stator system in the AFPMSM under investigation. The configuration is composed of two rotors and one stator, so that only half of the geometry with a symmetry plane in the middle is studied. In order to expedite the geometry parametrization procedure, the model is slightly simplified as compared to the real machine. The right disk corresponds to the stator, and the left one to the rotor. There are sixteen magnets that are evenly distributed on the rotor side, facing the stator disk in the gap. Thus, the Pole Pitch angle, which is the angular distance between two adjacent poles on the machine, is equal to $1/16 \times 360° = 22.5°$. Due to 22.5° periodicity, only 1/16 of the whole system is taken into account. There also exists an annular opening at the rotor disk. The effects of the radial spokes, connecting the inner edge of the rotor to the outer side across the annular opening, on the flow field have been neglected.

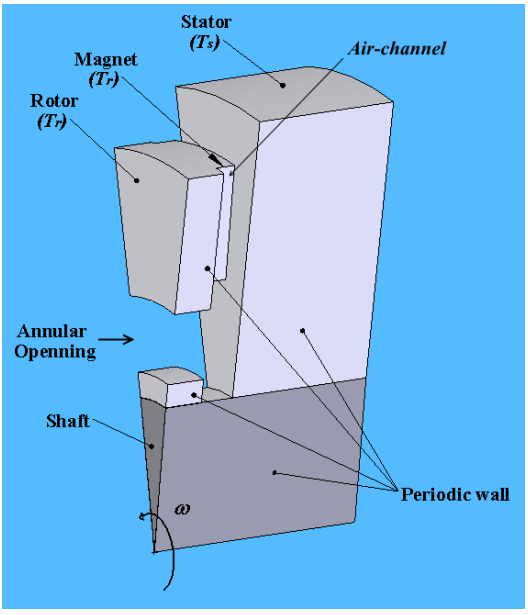

Figure 4.1: Schematic of the rotor-stator system in the AFPMSM under study.

The geometrical details of this rotor-stator arrangement have been shown in Fig. 4.2. The radius of the rotor and the stator are kept constant at 74 mm and 84 mm, respectively. The surfaces *"Stator gap upper"* and *"Stator gap lower"* lie between $0.6 \leq r/R_s \leq 1$ and $0.3 \leq r/R_s \leq 0.6$ respectively, where R_s is the radius of the stator.

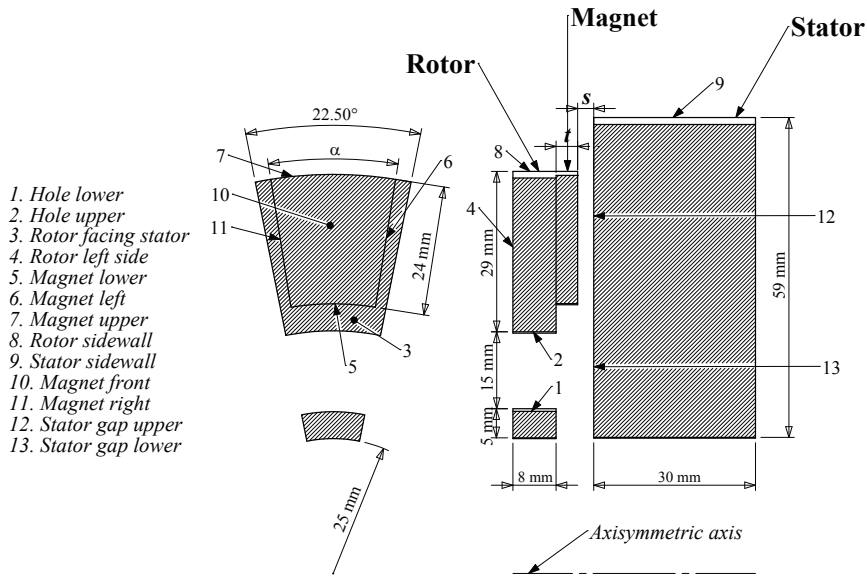

Figure 4.2: Geometrical details and name of each surface in the machine.

The current system can be characterized by four non-dimensional parameters, namely the gap size ratio $G = s/R$, the rotational Reynolds number $Re = \omega R^2/\nu$, the magnet angle ratio $\alpha_m = \frac{\alpha}{\alpha_p}$ with $\alpha_p = 360°/16 = 22.5°$ the pole angle, and the magnet thickness ratio $L = t/R$. In these definitions, s is the air-gap thickness, R denotes the radius of the rotor, ω is the angular velocity of the rotor, ν represents the kinematic viscosity of air, α is the magnet angle, and t denotes the magnet thickness as shown in Fig. 4.2. The objective is to construct correlations to express the mean Nusselt number for the practical ranges of $0.0068 \leq G \leq 0.0811$, $3.53 \times 10^4 \leq Re \leq 3.53 \times 10^5$, $0.7 \leq \alpha_m \leq 0.9$ and $0.027 \leq L \leq 0.0811$. For the case-study here, these ranges of non-dimensional parameters correspond to a rotor tip velocity of $10 - 100$ m/s (equivalent to the angular velocity of $1290.4 - 12904$ rpm), a gap thickness of $0.5 - 6$ mm, a magnet angle of $0.7 \times 22.5 - 0.9 \times 22.5°$ and a magnet thickness of $2 - 6$ mm. It is assumed that the surfaces are isothermal, since the thermal conductivities of the materials in the rotor and the stator are relatively high. The Biot numbers (Bi) for the rotor and

the stator disks at the reference point are 0.003 and 0.013, respectively. Air is considered as an incompressible gas, obeying the incompressible ideal gas law as,

$$\rho = \frac{P_{atm}}{\overline{R}T} \tag{4.1}$$

where P_{atm} is the atmospheric pressure, $\overline{R}$ is the specific gas constant and T is the air temperature. Note that the compressibility effect is negligible as the value of Mach number is below 0.3. The air viscosity varies with temperature through Sutherland's viscosity law as,

$$\mu = \mu_0 \left(\frac{T}{T_0}\right)^{3/2} \frac{T_0 + C}{T + C} \tag{4.2}$$

where C corresponds to a Sutherland constant of 110 K, T_0 = 273 K, $\mu_0 = 1.716{\times}10^{-5}$ kg/(m.s). The thermal conductivity of air varies with temperature, keeping the Prandtl number constant at 0.7. It is also presumed that the buoyancy effect is negligible. The properties for the Reynolds number are evaluated at the average temperature of the rotor, the stator and the atmosphere, that is, $\frac{T_r + T_s + T_{amb}}{3}$.

The Frozen Rotor (FR) concept, (or MRF method) which yields a steady state solution, is applied to model the motion of the rotor. In the MRF method, as explained briefly in Chapter 3, the computational mesh is fixed, and the flow in each domain is solved using the moving reference frame equations. For the machine under consideration, the flow is steady since the stator surface is smooth and the influence of the natural convection is negligible. Thus, the results of the MRF method will be the same as when sliding interfaces would have been used. This approach has been successfully applied in the modeling of the electrical machines [43, 81]. The governing continuity, momentum, and energy equations in this method are given by:

$$\nabla.(\rho\overrightarrow{v}) = 0 \tag{4.3}$$

$$\nabla.(\rho\overrightarrow{v_r} \otimes \overrightarrow{v}) + \rho(\overrightarrow{\Omega} \times \overrightarrow{v}) = -\nabla p + (\mu + \mu_t)\nabla^2\overrightarrow{v} \tag{4.4}$$

$$\nabla.\left(\rho\overrightarrow{v_r}h + p(\overrightarrow{\Omega} \times \overrightarrow{r})\right) = \nabla.((k + k_t)\nabla T) \tag{4.5}$$

In the above, $\overrightarrow{v_r}$ is the relative velocity with respect to the rotating frame, $\overrightarrow{v}$ is the absolute velocity in the stationary frame, $\overrightarrow{\Omega}$ represents the angular velocity vector of the rotating domain, h is the specific enthalpy of air, k is air thermal conductivity, k_t denotes the turbulent thermal conductivity, μ is the molecular viscosity and μ_t is the turbulent viscosity.

As shown in Fig. 4.3, the computational domain is divided into a rotating and a stationary part by an interface which is situated in the middle

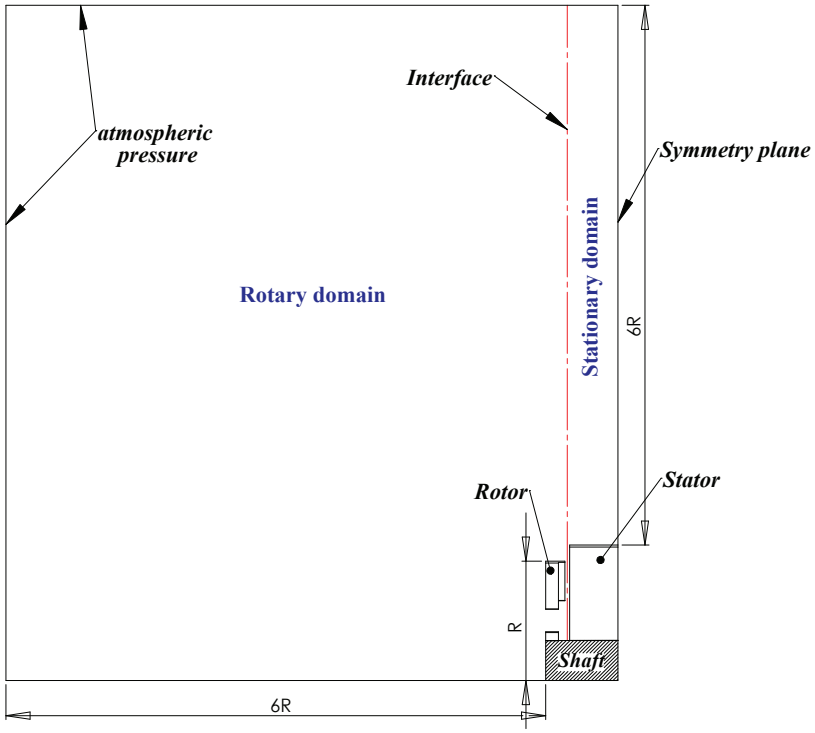

Figure 4.3: Side view of the computational domain (The shaft is not included in the numerical model.)

of the gap between the magnets and the stator. The governing equations in each subdomain are written with respect to that subdomain's reference frame; nevertheless, the velocities in each subdomain are calculated in the absolute frame. Thus, no further transformation is required at the interface between the rotary and the stationary subdomain. The atmospheric pressure boundary is placed far away from the rotor.

4.2 CFD simulation results

The case of $G = 0.0135$, $Re = 1.06 \times 10^5$, $\alpha_m = 0.8$ and $L = 0.0540$, along with the surface temperature of $T_s = 120°\text{C}$ and $T_r = 100°\text{C}$, is chosen as a reference point for this parametric study. This corresponds to an air-gap thickness of 1.0 mm, a rotational speed of 3871.3 rpm, a magnet angle of 18° and a magnet thickness of 4.0 mm. CFD simulations are used to provide adequate data to construct empirical correlations for the convective heat transfer coefficient. The commercial CFD software Ansys FLUENT

has been utilized to simulate the 3-D flow fields and the heat transfer. The governing equations are solved by using the SIMPLE-algorithm and the convective terms in the momentum, turbulence and energy equations are spatially discretized using a second-order upwind scheme. The turbulence is treated with a SST $k-\omega$ model. Iterative convergence was achieved as the relative residual of the momentum-related variables, the turbulence-related variables and energy are below 10^{-6}, 10^{-7} and 10^{-10}, respectively. These residuals ensured that the monitored values of the surface heat fluxes reached a constant value independent of the number of iterations.

Fig. 4.4 shows the mesh of the rotor surface with the magnet. For the whole domain, a hexahedral mesh type with 2,944,000 cells is used. Moreover, a mesh independency study was carried out by making a comparison between the results of the heat fluxes with the coarse and the fine mesh sizes including 478,800 and 10,605,250 cells. It was found that the results are roughly mesh independent with the relative error of 0.5 % in predicting the stator heat transfer rate. Furthermore, the computational mesh ensures that the y^+ values at the solid walls are less than unity.

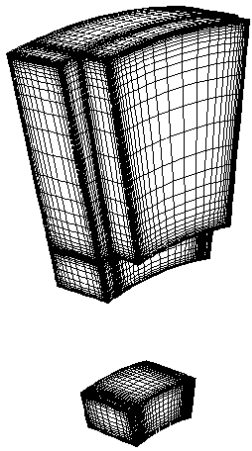

Figure 4.4: The surface mesh of the rotor disk.

4.2.1 Flow structure in the air-gap and the air-channel

It is worth highlighting that the air-gap specifies the axial distance between the surfaces of *"magnet front"* and *"Stator gap upper"*, and the air-channel represents the chamber being made between two successive magnets. The accurate prediction of the boundary layer flow in the air-gap as well as in the air-channel is crucial to evaluate the convective heat transfer coefficients. In

this section, therefore, we focus on the influence of significant parameters on the flow characteristics across these regions.

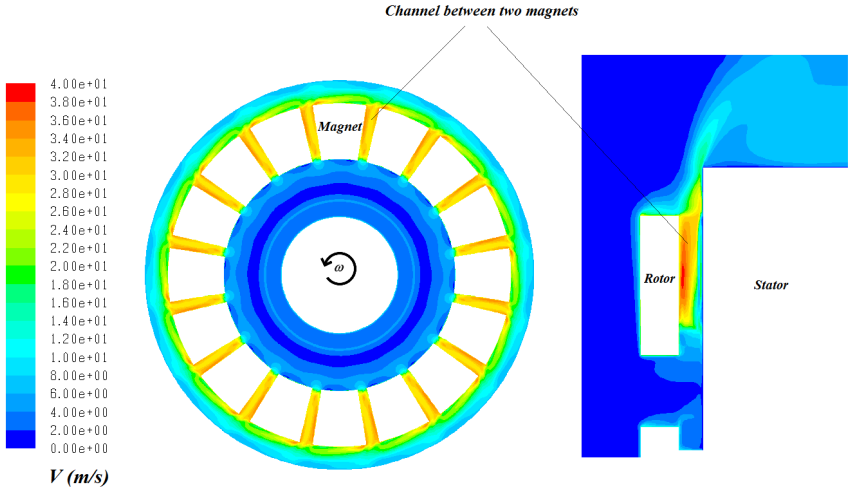

Figure 4.5: The velocity contour in the orthogonal plane through the middle of the magnets (left figure) and in the meridional plane through the center of the air-channel (right figure) for $G = 0.0135$, $Re = 1.06 \times 10^5$, $\alpha_m = 0.8$, $L = 0.0540$, $R_r = 74$ mm and $R_s = 84$ mm.

Fig. 4.5 illustrates the velocity contours in the orthogonal plane through the middle of the magnets (left figure) and in the meridional plane through the center of the air-channel (right figure) for $G = 0.0135$, $Re = 1.06 \times 10^5$, $\alpha_m = 0.8$ and $L = 0.0540$. The other magnets have been made visible through CFD Post-processing. It is observed that the magnets act as a centrifugal channel, accelerating the airflow outward through the air-channel.

To give a better understanding of the flow field, the non-dimensional radial and tangential velocity profiles across the air-gap for the narrow and the wide gap size ratio have been shown in the Figs. 4.6–4.7. Note that the horizontal axis indicates the position between the surfaces of *"Magnet front"* and *"Stator gap upper"*. It can be seen that, for both gap size ratios, there is a net outflow alongside the air-gap. In fact, the annular opening allows the airflow to go into the gap region, resulting in a net radial flow outward. For the small gap size ratio ($G = 0.0068$), the gradient of the tangential velocity at the higher radii is rather constant, typical for Couette flow. For the wide gap size, however, the Stewartson type of flow [126] with only one boundary layer on the rotating disk can be observed. In other words, the tangential component of the velocity is almost zero everywhere except for in the rotor boundary layer.

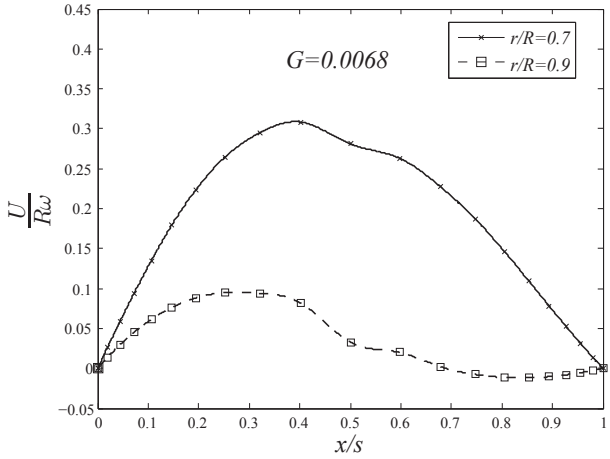

(a)

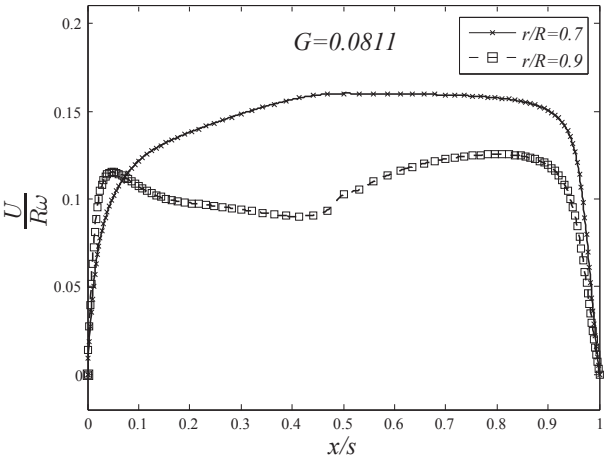

(b)

Figure 4.6: Non-dimensional radial velocity variations across the air-gap at $Re = 1.06 \times 10^5$, $\alpha_m = 0.8$ and $L = 0.0540$. On the x axis, $x/s = 0$ denotes the magnet surface and $x/s = 1$ is the stator surface. (a) $G = 0.0068$, (b) $G = 0.0811$.

4.2.2 Heat transfer characteristics in the air-gap and the air-channel

Fig. 4.8 illustrates the temperature contours in the midplane of the rotor-stator configuration, with, as mentioned before, the rotor and the stator surface temperatures at 100°C and 120°C, respectively. The ambient air temperature is considered 25°C. It is observed that the cold air flows through

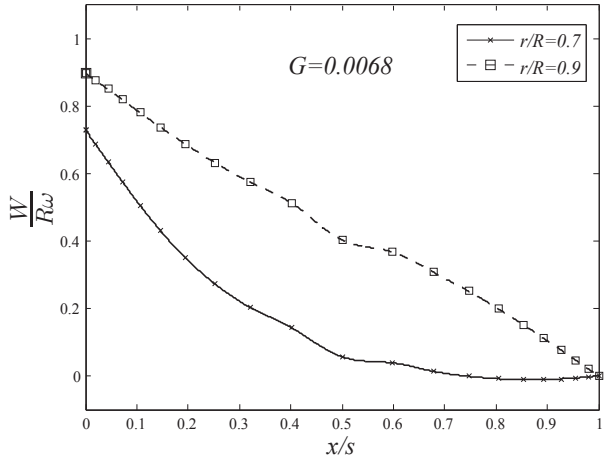

(a)

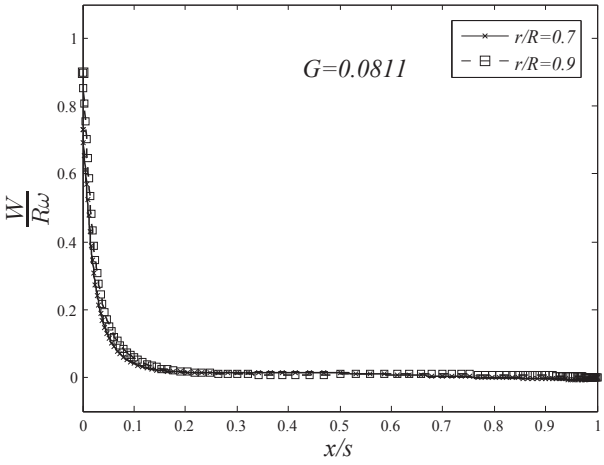

(b)

Figure 4.7: Non-dimensional tangential velocity variations across the air-gap at $Re = 1.06 \times 10^5$, $\alpha_m = 0.8$ and $L = 0.0540$ for (a) $G = 0.0068$, (b) $G = 0.0811$.

the annular opening, entering into the gap region.

To have a clear view of the convective heat transfer for the current rotor-stator system, the temperature profiles across the air-gap between the magnet and the stator surface for different radii have been depicted in Fig. 4.9. The right side of the horizontal axis represents the area adjacent to the surface *"Stator gap upper"* and the left side belongs to the surface *"magnet front"*. For the case of the narrow gap size, the thermal boundary

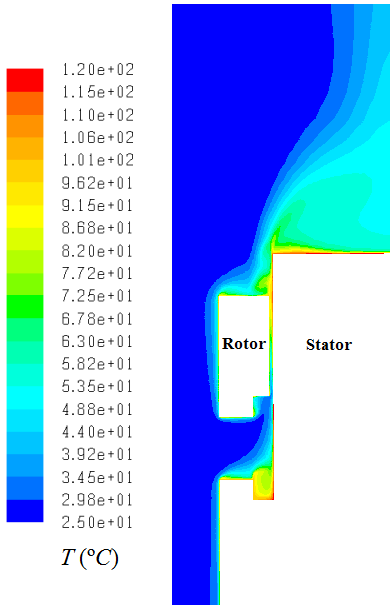

Figure 4.8: Temperature contour at the meridional plane through the center of the magnets for $G = 0.0135$, $Re = 1.06 \times 10^5$, $\alpha_m = 0.8$, $L = 0.0540$, $T_s = 120°\text{C}$ and $T_r = 100°\text{C}$.

layers next to the magnet and the stator surface are merged, while for the wide gap thickness, two distinguishable unmerged thermal boundary layers can be noticed. Furthermore, the slope of the graphs in the vicinity of the stator surface (right side of the horizontal axis) shows that the heat transfer rate increases at the outer periphery of the gap region. For the wide gap sizes, the direction of the heat transfer is always from the surface towards the fluid, considering the higher value of the surface temperature than the fluid adjacent to it.

The contours of the convective heat flux for the stator and the rotor surfaces are shown in Fig. 4.10. It can be interpreted that the local heat transfer is highest at the place on the magnet where the airflow starts entering the air-channel, this is at low radius. In fact, the ingress of the cold air with very low temperature (almost equal to the ambient temperature) at the inlet of the channel between the consecutive magnets can give rise to a maximum in the local heat flux. The peak spots in the stator surface correspond with the air-channel position in the rotor.

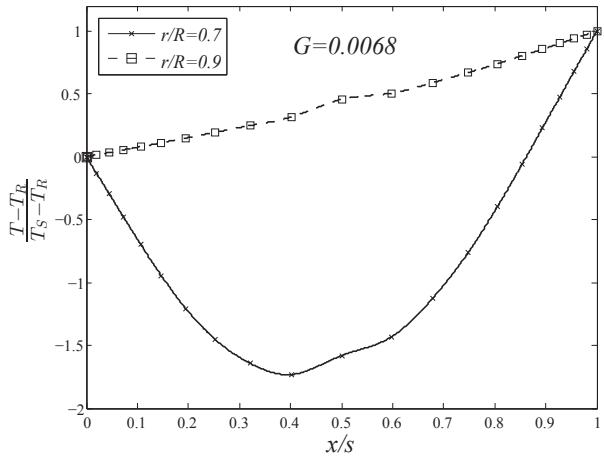

(a)

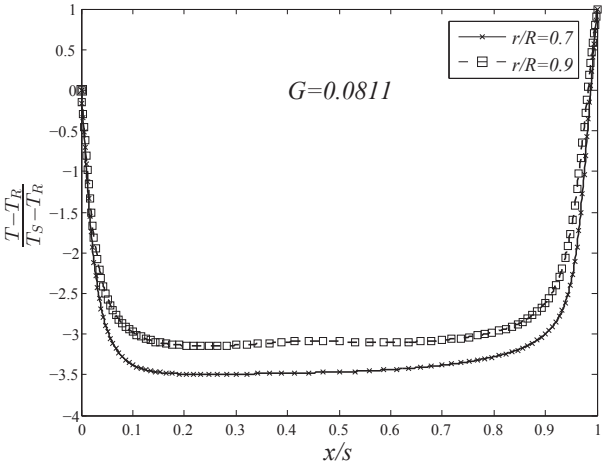

(b)

Figure 4.9: Non-dimensional temperature variations across the air-gap at $Re = 1.06 \times 10^5$, $\alpha_m = 0.8$, $L = 0.0540$, $T_s = 120°\text{C}$ and $T_r = 100°\text{C}$ for (a) $G = 0.0068$, (b) $G = 0.0811$.

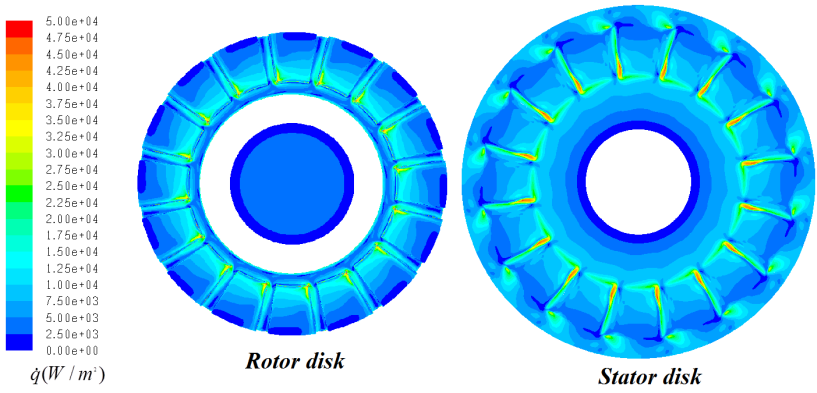

Figure 4.10: Heat flux contours at the front view of the rotor and the stator disks for $G = 0.0135$, $Re = 1.06 \times 10^5$, $\alpha_m = 0.8$, $L = 0.0540$, $R_r = 74$ mm, $R_s = 84$ mm, $T_s = 120°\text{C}$ and $T_r = 100°\text{C}$.

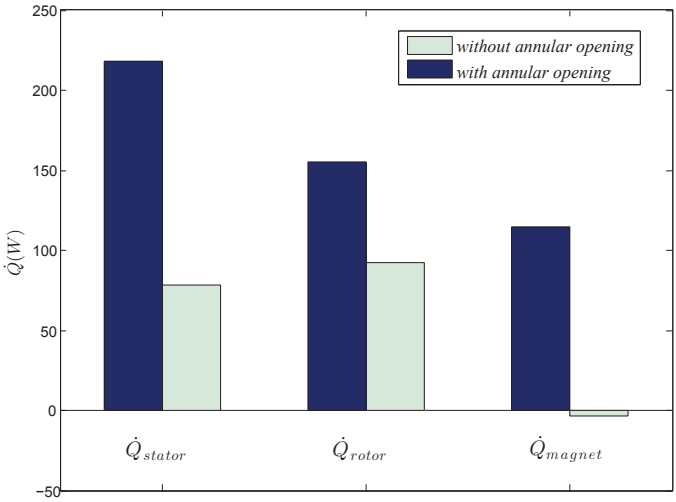

Figure 4.11: Effects of the annular opening on the overall heat transfer rate at $G = 0.0135$, $Re = 1.06 \times 10^5$, $\alpha_m = 0.8$, $L = 0.0540$, $R_r = 74$ mm, $R_s = 84$ mm, $T_s = 120°\text{C}$ and $T_r = 100°\text{C}$.

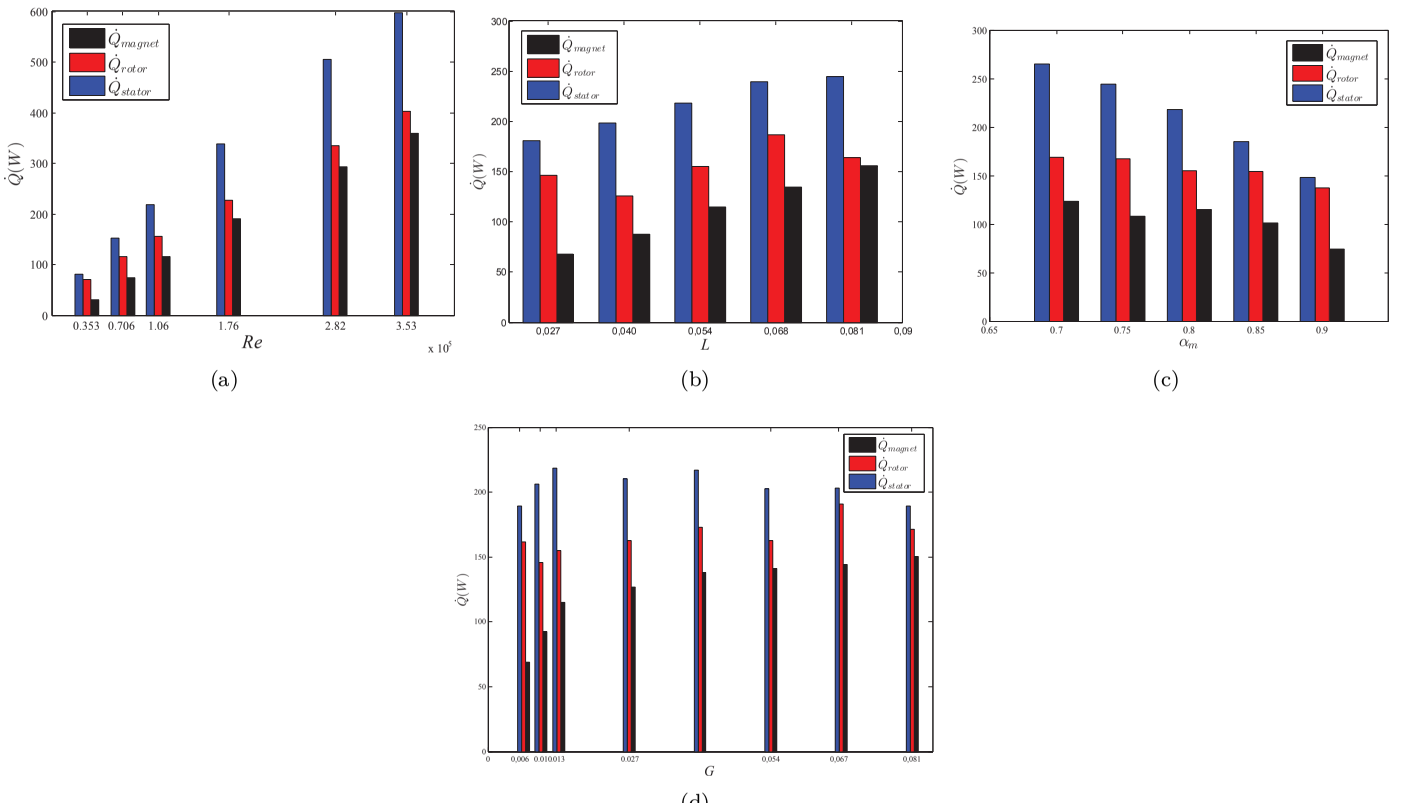

Figure 4.12: The influence of the important parameters on the overall heat transfer rate (W) per rotor when $R_r = 74$ mm, $R_s = 84$ mm, $T_s = 120°$C and $T_r = 100°$C for various (a) Re, (b) L, (c) α_m and (d) G.

To see how the annular opening contributes to the heat evacuation of the system, the total heat transfer from the rotor, the stator, and the magnet surfaces for two cases with and without annular opening has been compared in Fig. 4.11. The positive values of the heat transfer rate correspond to the direction of heat transfer from surface to fluid, whereas the negative values denote the direction of heat transfer from fluid to surface. It is clear that the addition of the annular opening enormously improves the cooling of the system. For example, the heat transfer rate becomes more than double for the entire rotor and stator surfaces. To take advantage of the magnet as a centrifugal channel, the annular opening should be introduced to the rotor disk. In this way, more air flow is allowed to pass through the air-channels and the air-gap between the rotor and the stator disk.

Fig. 4.12 clarifies the influence of significant parameters including the rotational Reynolds number (Re), the magnet thickness ratio (L), the magnet angle ratio (α_m) and the gap size ratio (G) on the overall convective heat transfer on the surfaces of the stator, the rotor and the magnet. These data account for the half of the machine. By default the values of the parameters here are $G = 0.0135$, $Re = 1.06 \times 10^5$, $\alpha_m = 0.8$ and $L = 0.0540$. There is an increase in the heat transfer rate within the system as either Re or L goes up. In fact, the increase of Re from 3.53×10^4 to 3.53×10^5 results in the heat transfer for the stator surfaces increasing by 600%. From the graph it is also clear that the stator heat transfer increases by 35% as L varies from 0.027 to 0.081. By contrast, the overall heat transfer diminishes when α_m increases; in particular, the total heat transfer of the stator surfaces drops by approximately 40% as α_m increases from 0.7 to 0.9. Additionally, an increase in the gap size ratio from 0.006 to 0.081 leads to the overall heat transfer rate on the magnet surfaces to improve by more than 110%, while the stator heat transfer remains rather constant.

4.3 Correlations for convective heat transfer

4.3.1 Minimization method for the reference temperature

The aim of the CFD simulations is to construct the correlations for the convective heat transfer for all the surfaces in the AFPMSM under study. The current rotor-stator configuration consists of thirteen surfaces, including hole lower, hole upper, rotor facing stator, rotor left side, magnet lower, magnet left, magnet upper, rotor sidewall, stator sidewall, magnet front, magnet right, stator gap upper and stator gap lower. The proposed correlations are capable of predicting the average heat flux for all the surfaces as

a function of the important parameters, namely the gap size ratio, the rotational Reynolds Number, the magnet angle ratio, the magnet thickness ratio and the surface temperatures of the rotor and the stator and the ambient temperature.

For an isothermal surface *f*, the convective heat transfer coefficient h_f is defined as,

$$h_f = \frac{\dot{q}_f}{(T_{sur,f} - T_{ref,f})} \tag{4.6}$$

where $\dot{q}_f$ represents the heat flux of the surface *f*, $T_{sur,f}$ is the surface temperature and $T_{ref,f}$ denotes the reference temperature. Also, the Nusselt number for the surface *f*, Nu_f, is given by,

$$Nu_f = \frac{h_f R}{k} \tag{4.7}$$

where R is the radius of the rotor/stator (depending on the respective surface whether it belongs to the rotor or to the stator) and k is the thermal conductivity of air.

As mentioned earlier, for convenience, the ambient temperature has been widely used as the reference temperature in the literature, which has a serious drawback. In fact, the choice of using the ambient temperature makes the presented correlations for the convective heat transfer coefficients dependent on the ambient temperature and the surface temperature. It would be much more convenient if a reference temperature could be chosen such that the heat transfer coefficient becomes independent of the temperatures. To tackle this problem, it is assumed here that the reference temperature, T_{ref}, can be correlated with the surface temperatures and the ambient temperature through the following linear formulation,

$$T_{ref,f} = a_f T_r + b_f T_s + [1 - (a_f + b_f)]\, T_{amb} \tag{4.8}$$

where the subscripts *r, s* and *amb* denote rotor, stator and ambient. The unknown coefficients of a_f and b_f are dependent on *G, Re*, α_m and L which will be further discussed in this section.

To begin with, Eq.(4.8) is substituted in Eq.(4.6) and then in Eq.(4.7). Subsequently, Nu_f can be given as a function of the coefficients a_f and b_f as follows,

$$Nu_f = \frac{\dot{q}_f R}{(T_{sur,f} - a_f T_r - b_f T_s - [1 - (a_f + b_f)]\, T_{amb})\, k} \tag{4.9}$$

CFD simulations are carried out with the non-dimensional parameters kept at the reference point ($G = 0.0135$, $Re = 1.06 \times 10^5$, $\alpha_m = 0.8$ and $L =$

0.0540) with four combinations of T_s and T_r according to Table 4.1. In this way, the heat flux for each case can be obtained. Thus, the only unknowns in Eq.(4.9) are a_f and b_f. The objective is to find the appropriate values of the coefficients a_f and b_f that minimize the standard deviation (σ) of the estimated Nusselt numbers in Eq.(4.9) for the surface f according to,

$$\sigma_f = \left[\frac{1}{n-1} \sum_{i=1}^{n} (Nu_{f,i} - \overline{Nu}_f)^2 \right]^{1/2} \tag{4.10}$$

where $n = 4$ corresponding to the number of temperature combinations. To achieve the global minimum of the standard deviation of Nu_f, a Pattern-Search algorithm from the Matlab Optimization Toolbox is used. The lower and upper limits of a_f and b_f are set to 0 and 1, in line with the physics of the problem. The initial points are the results of the solution by setting a_f and b_f to 0.001 in the first place. Once the minimization algorithm yields the solution, the coefficients a_f and b_f will be defined. The mean value of the Nusselt number $\overline{Nu}_f$ from Eq.(4.10) will be considered as the desired value for the Nusselt number. The mean Nusselt number becomes nearly independent of the surface temperature of the rotor and the stator, as long as the standard deviation resulting from Eq.(4.10) is small.

Table 4.1: Different approaches to find the appropriate values of the reference temperature from CFD. Results for the surface *"magnet front"*.

Combination	T_s (°C)	T_r (°C)	$\dot{Q}$ (W)	Different approaches for the reference temperature									
				Ambient temperature			Average bulk temperature				Minimization method			
				$Nu_{f,i}$	$\overline{Nu}_f$	σ_f	T_{ref} (°C)	$Nu_{f,i}$	$\overline{Nu}_f$	σ_f	T_{ref} (°C)	$Nu_{f,i}$	$\overline{Nu}_f$	σ_f
1	120	100	55.4	301.8	285.5	16.0	75.7	929.8	1180.2	271.8	41.6	387.6	384.6	6.2
2	120	80	35.3	262.6			70.7	1550.6			41.6	376.2		
3	130	110	62.2	299.2			82.1	910.0			43.4	381.8		
4	100	70	30.6	278.5			60.6	1330.4			38.1	392.8		

Table 4.2: Minimization method to find a and b for the surface *"hole lower"*.

Combination	T_s (°C)	T_r (°C)	$\dot{Q}$ (W)	a_1	b_1	T_{ref} (°C)	$Nu_{1,i}$	$\overline{Nu}_1$	σ_1
1	120	100	24.2	0.0010	0.0010	25.2	294.4	293.5	2.0
2	120	80	17.6			25.2	291.3		
3	130	110	27.2			25.2	292.1		
4	100	70	14.6			25.1	296.3		

The applicability of the proposed method is confirmed through comparing the results with different choices for the reference temperature as the ambient temperature and the average bulk fluid temperature discussed in Chapter 3 (see Table 4.1). The latter was demonstrated to be effective for a simple rotor-stator system enclosed in a cylindrical cover. Nonetheless, with the annular opening and the magnets present at the rotor disk, the minimization method is a far superior approach determining an appropriate reference temperature. According to Table 4.1, the deviation of the mean Nusselt number in the minimization method with each of the four temperature combinations is less than 3%.

It is easily discernible through Eq.(4.8) that as long as the values of a_f and b_f are close to zero, the reference temperature would be equal to the ambient temperature. This seems to be a good choice for the surfaces hole lower, hole upper, rotor facing stator, rotor left side, magnet lower, magnet left, magnet upper, rotor sidewall and stator sidewall. As an example, the results for the surface *"hole lower"* has been shown in Table 4.2. For the rest of the surfaces, such as magnet front, magnet right, stator gap upper and stator gap lower the appropriate values of a_f and b_f are required to be predicted.

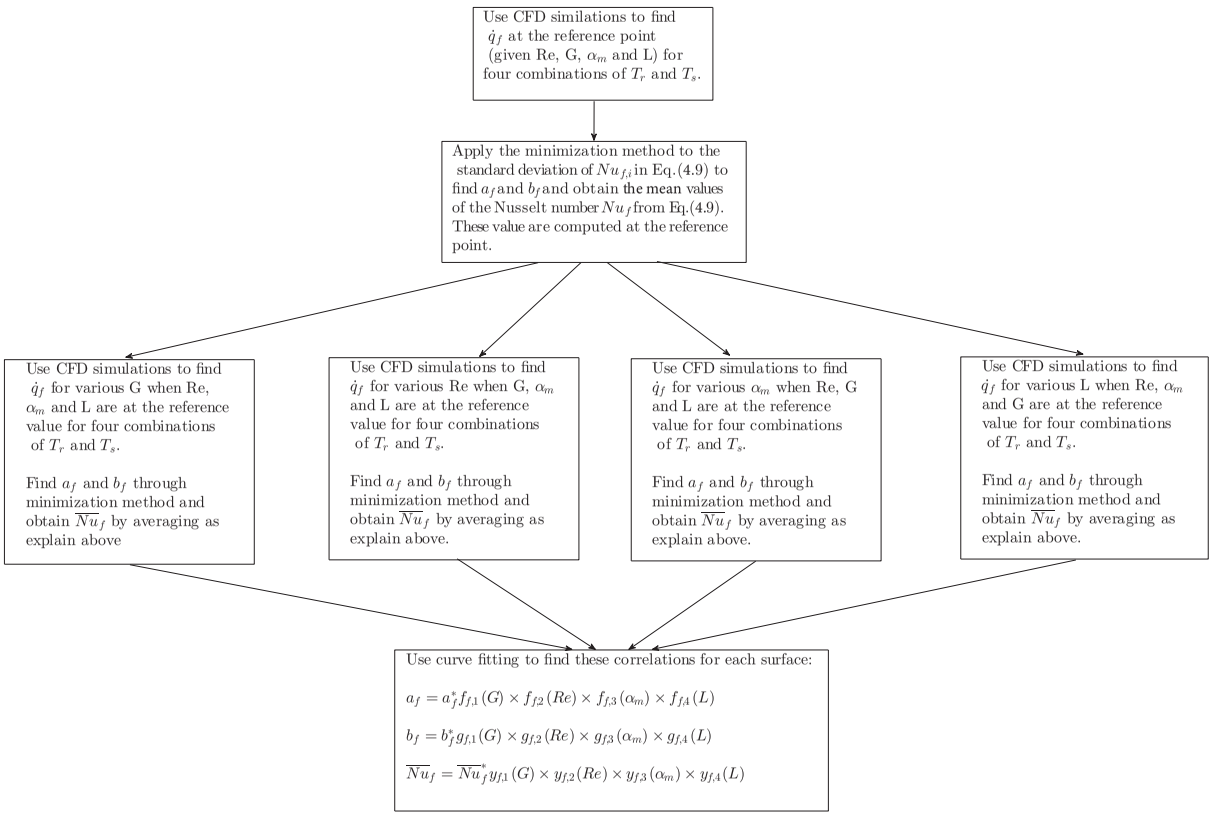

Figure 4.13: The procedure for obtaining the correlations of the convective heat transfer.

4.3.2 Derivation of the correlations

The step-by-step procedure of deriving the correlations is illustrated in Fig. 4.13. Knowing a_f, b_f and $\overline{Nu}_f$ at the reference point as shown in Table 4.1, the goal is to estimate these when the significant non-dimensional parameters namely G, Re, α_m and L as well as the surface temperature of the rotor and the stator vary. To this end, first, a set of CFD simulations are performed for $G = \{0.0068, 0.0101, 0.0270, 0.0405, 0.0541, 0.0676, 0.0811\}$ at four temperature combinations of the rotor and the stator, while the other parameters are kept at the reference point, i.e., $Re = 1.06 \times 10^5$, $\alpha_m = 0.8$, $L = 0.0540$. Thus, the heat fluxes for each surface for all the simulated cases are computed. Once again, the minimization algorithm is employed to calculate the appropriate values of a_f, b_f for each case separately. Afterwards, the mean Nusselt number ($\overline{Nu}_f$) in Eq.(4.10), which is the average of the values acquired from the four temperature combinations, will be considered as the Nusselt number for the case under study. As a consequence, variations of the convective heat transfer with G when other parameters are fixed at the reference point can be known. The same procedure, as explained for G, must be repeated when Re, α_m and L are subjected to change. In this way, the variations of a_f, b_f and $\overline{Nu}_f$ for each surface within the machine at different non-dimensional parameters become known. 96 simulation runs have been performed, altogether. In the end, it is necessary to provide formulations to express the convective heat transfer coefficients as follows,

$$\begin{aligned} a_f &= F_f\left(G, Re, \alpha_m, L\right) \\ b_f &= G_f\left(G, Re, \alpha_m, L\right) \\ \overline{Nu}_f &= Y_f\left(G, Re, \alpha_m, L\right) \end{aligned} \tag{4.11}$$

where the functions F_f, G_f and Y_f need to be defined. These functions with four variables can be rewritten as the product of four functions with one variable as,

$$\begin{aligned} a_f &= a_f^* f_{f,1}(G) \times f_{f,2}(Re) \times f_{f,3}(\alpha_m) \times f_{f,4}(L) \\ b_f &= b_f^* g_{f,1}(G) \times g_{f,2}(Re) \times g_{f,3}(\alpha_m) \times g_{f,4}(L) \\ \overline{Nu}_f &= \overline{Nu}_f^* y_{f,1}(G) \times y_{f,2}(Re) \times y_{f,3}(\alpha_m) \times y_{f,4}(L) \end{aligned} \tag{4.12}$$

At the above, the superscript $*$ represents the values of a_f, b_f and $\overline{Nu}_f$ at the reference point. To obtain all of the above functions with one variable, curve fitting for each surface should be carried out one after the other. Note that the output from each function at the reference point is almost one. As discussed, there are two categories of surfaces in the current system: the ones where the reference temperature is almost equal to the ambient

temperature, and those where the reference temperature differs from the ambient temperature and should, therefore, be predicted. The details of the formulations for each surface are presented in Tables 4.3-4.4.

Table 4.3: Correlations for Nusselt number for the surfaces with $T_{ref} \cong T_{amb}$ (see Fig. 4.2 and Eq. (4.12)).

Surface	hole lower, $f = 1$	hole upper, $f = 2$	Rotor facing stator, $f = 3$	Rotor left side, $f = 4$	Magnet lower, $f = 5$
$\overline{Nu}_f^*$	91.61	239.56	235.85	216.52	492.10
$y_{f,1}$	-4.453G+1.073	1.645G+0.976	$1.647G^{0.1117}$	1.785G+0.9766	-3.29G+1.024
$y_{f,2}$	$5.695 \times 10^{-6}Re + 0.3979$	$5.238 \times 10^{-6}Re + 0.425$	$7.975 \times 10^{-6}Re + 0.1496$	$6.501 \times 10^{-6}Re + 0.3041$	$5.755 \times 10^{-6}Re - 0.3702$
$y_{f,3}$	$0.4525\alpha_m + 1.385$	$-0.7163\alpha_m + 1.567$	$-2.903\alpha_m + 3.29$	$0.1325\alpha_m + 0.8983$	$-1.20163\alpha_m^{7.461} + 1.226$
$y_{f,4}$	-3.447L+1.162	1.478L+0.9211	3.917L+0.7895	1.751L+0.9061	$-0.03425L^{-0.5286} + 1.159$

Surface	Magnet left, $f = 6$	Magnet upper, $f = 7$	Rotor sidewall, $f = 8$	Stator sidewall, $f = 9$
$\overline{Nu}_f^*$	285.20	202.28	181.40	105.76
$y_{f,1}$	$-0.002076G^{-1.193} + 1.345$	$1.62G^{0.11}$	2.322G+0.9728	$-4.476G^{-0.03846} - 6.795G + 6.373$
$y_{f,2}$	$9.1 \times 10^{-6}Re + 0.02189$	$8.669 \times 10^{-6}Re + 0.06863$	$4.737 \times 10^{-6}Re^{1.038} + 0.2024$	$3.91 \times 10^{-5}Re^{0.8773}$
$y_{f,3}$	$-7.126\alpha_m^{29.8} + 0.9939$	$-0.9382\alpha_m^{8.902} + 1.132$	$-1.005\alpha_m + +1.803$	$0.8805\alpha_m^{6.245} + 1.218$
$y_{f,4}$	$6.707L^{0.04971} - 4.8$	$-0.007892L^{-1.107} + 1.189$	$1.806L^{0.2031}$	$-1.246L^{-0.1443} + 2.899$

Table 4.4: Correlations to estimate the convective heat transfer for the surfaces with $T_{ref} \neq T_{amb}$ (see Fig. 4.2 and Eq. (4.12)).

Surface	Magnet front, $f = 10$	Magnet right, $f = 11$	Stator gap upper, $f = 12$	Stator gap lower, $f = 13$
a_f^*	0.00100	0.00100	0.4153	0.2317
b_f^*	0.1744	0.1739	0.0010	0.0010
$\overline{Nu}_f^*$	304.84	606.37	374.53	243.90
$f_{f,1}$	$1.71 \times 10^{-10} G^{5.386}$	$-0.01155G + 1$	$0.2824G^{-0.3381} - 0.2002$	$0.2033G^{-0.373}$
$f_{f,2}$	1	$-1.967 \times 10^{-9} Re + 1$	$74.78Re^{-0.3734}$	$2.096 \times 10^{6} Re^{-1.422} + 0.9092$
$f_{f,3}$	$9.892 \times 10^{-16} \alpha_m + 0.9997$	$1.46 \times 10^{-14} \alpha_m^{-102.4} + 0.9929$	$2.803\alpha_m^{1.518} - 0.9881$	$26.23\alpha_m^2 - 40.02\alpha_m + 16.23$
$f_{f,4}$	$-3.205 \times 10^{-10} L + 0.9996$	$5.96 \times 10^{-11} L + 0.9999$	$0.4205L^{-0.2972}$	$0.1982L^{-0.5497}$
$g_{f,1}$	$0.005875G^{-1.206}$	$-15.73G + 1.135$	$3.386 \times 10^{-16} G^{-7.289} + 0.9843$	$0.009G + 1$
$g_{f,2}$	$1.638 \times 10^{4} Re^{-0.8264} - 0.1472$	$31.79Re^{-0.1803} - 2.969$	$7.556 \times 10^{13} Re^{-3.218} + 0.9953$	$1.824 \times 10^{-9} Re + 1$
$g_{f,3}$	$3.416\alpha_m^{6.722} + 0.2816$	$-0.09794\alpha_m^{-7.204} + 1.452$	$1.731 \times 10^{-15} \alpha_m + 1$	$1.731 \times 10^{-15} \alpha_m + 1$
$g_{f,4}$	$0.03617L^{-0.9332} + 0.4602$	$-4.089 \times 10^{5} L^{5.46} + 1.021$	$-7.017 \times 10^{-11} L + 0.9999$	$2.506 \times 10^{-10} L + 1$
$y_{f,1}$	$-0.0167G^{-0.6493} + 1.277$	$4.723G^{0.3274} - 14.47G$	$-2.967G^{0.6937} + 1.142$	$-0.6211G + 1.005$
$y_{f,2}$	$3.552 \times 10^{-5} Re^{0.886}$	$0.001593Re^{0.5825} - 0.3542$	$0.0001122Re^{0.7824} + 0.04018$	$0.0003289Re^{0.679} + 0.1569$
$y_{f,3}$	$-0.905\alpha_m^{4.158} + 1.35$	$-15.86\alpha_m^{35.42} + 0.998$	$-0.7732\alpha_m^{5.583} + 1.224$	$-0.8183\alpha_m^{6.34} + 1.21$
$y_{f,4}$	$3.607L + 0.8067$	$-113.7L^2 + 12.51L + 0.6539$	$13.86L^{1.709} + 0.9064$	$7.906L^{1.575} + 0.9243$

4.3.3 Validity of the proposed correlations

The correlations presented in this chapter have been obtained by varying one non-dimensional parameter while keeping the rest fixed at the reference point and repeating this for all the other variables. Hence, by comparing the results of the correlation with those obtained by CFD simulation for the cases in which neither G, Re, α_m nor L is at the reference point, the efficacy of the proposed correlations can be ensured. As a result, the comparison has been made for four different cases, shown in Table 4.5. The percentage error presented in this table corresponds to $Error\% = |\frac{\dot{Q}_{f,CFD} - \dot{Q}_{f,Correlation}}{\dot{Q}_{Stator,CFD}}| \times 100$. The denominator refers to the overall heat transfer in the stator surfaces from CFD simulation, and $\dot{Q}_{f,CFD}$ and $\dot{Q}_{f,Correlation}$ represent the heat transfer of the surface f given by CFD and correlations results. According to Table 4.5, the correlations presented in this chapter are able to assess accurately the convective heat transfer for all surfaces in the practical ranges of the important parameters in AF-PMSMs with the error percentage less than 5%.

Furthermore, the results of the correlations for the variations of mean Nusselt number versus Reynolds number for the stator surface in the gap are compared in Fig. 4.14 with the numerical results by Wrobel et al. [81] and also with the experimental data reported by Howey et al. [134].

The presence of the magnet on the rotor disk was also taken into account in their study. In [81], however, the computational domain is slightly different than the case in this chapter as the rotor with magnets along with the stator disk are enclosed in a box with the prescribed ambient temperature. The averaged volume temperature was used as the reference temperature (no value was reported) which is expected to be higher than the calculated one in the open rotor-stator here. For this reason, the results of the proposed correlation underpredict the convection coefficient on the stator surface as compared to the numerical data reported by Wrobel et al. [81]. On the other hand, the results of the correlations are compared with the experimental data measured by Howey et al. [134] for the mean Nusselt number prediction. There is a small opening at the stator center allowing the air passes through the air-gap. The presented Nusselt number has been given by considering the ambient temperature as the reference temperature. To make a rough comparison, the reported value of the Nusselt number has been adjusted with the same reference temperature yielding by the proposed correlations. It is seen that the correlations here overestimate the Nusselt number when compared to the experiment by Howey et al. [134]. The main reason for this trend is that the influence of the annular opening in the rotor disk in this chapter is more prominent than the small opening in their

experiment so that more heat could be evacuated from the stator surface in our electrical machine. Generally, good agreements between the fully predictive model in this work with the available numerical and experimental data in the literature can be observed.

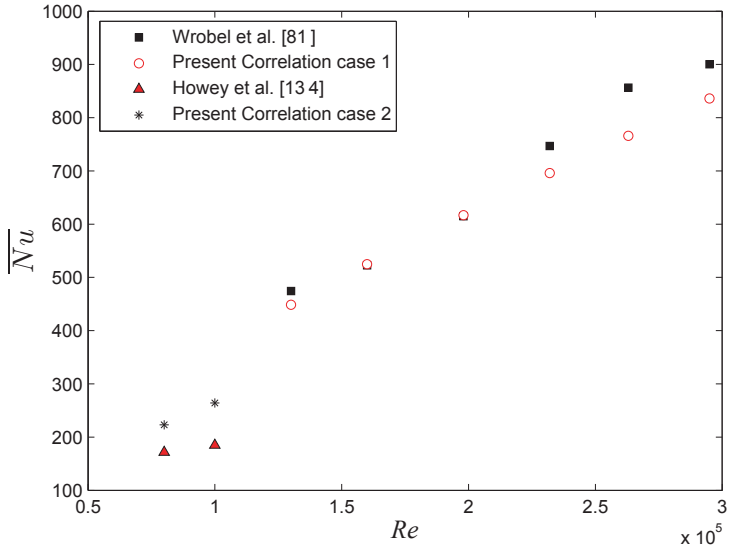

Figure 4.14: Comparison between the results of the proposed correlations at case 1 ($G = 0.0156$, $L = 0.0376$ and $\alpha_m = 0.8$) with the numerical results presented by Wrobel et al.[81] and also at case 2 ($G = 0.0212$, $L = 0.0540$ and $\alpha_m = 0.844$) with the experimental data of Howey et al. [134] for variations of $\overline{Nu}$ at the stator surface in the gap versus Re.

Table 4.5: Comparison between the CFD and the proposed correlations results for heat transfer rate (W) at different cases when $R_r = 74$ mm, $R_s = 84$ mm.

Surface	$Re = 8.931\times10^4$, $G = 0.0203$, $L = 0.0338$, α_m=0.77, $T_s = 115°C$, $T_r = 95°C$			$Re = 3.381\times10^5$, $G = 0.0203$, $L = 0.0338$, α_m=0.77, $T_s = 100°C$, $T_r = 80°C$			$Re = 1.210\times10^5$, $G = 0.0108$, $L = 0.0642$, α_m=0.82, $T_s = 125°C$, $T_r = 105°C$			$Re = 3.112\times10^5$, $G = 0.0108$, $L = 0.0642$, α_m=0.82, $T_s = 125°C$, $T_r = 105°C$		
	Proposed Correlations	CFD	Error%	Proposed Correlations	CFD	Error%	Proposed Correlations	CFD	Error%	Proposed Correlations	CFD	Error%
hole lower	3.7	3.7	0.0	7.4	6.2	0.3	4.8	5.0	0.1	9.5	9.8	0.0
hole upper	13.5	14.9	0.7	25.6	26.5	0.2	18.5	19.3	0.3	35.9	34.3	0.3
Rotor facing stator	21.5	23.3	0.9	54.7	60.2	1.2	25.6	26.9	0.5	60.3	60.4	0.0
Rotor left side	71.9	76.6	2.5	156.4	158.0	0.3	107.3	106.7	0.2	229.0	220.2	1.5
Magnet lower	7.1	7.6	0.3	14.3	15.9	0.3	19.9	20.8	0.3	40.4	40.5	0.0
Magnet left	6.2	7.6	0.7	17.8	20.4	0.6	17.2	18.8	0.6	43.8	46.6	0.5
Magnet upper	4.0	4.9	0.5	11.0	12.7	0.4	13.1	12.3	0.3	32.3	30	0.4
Rotor sidewall	15.4	18.5	1.6	38.9	37.1	0.4	24.3	24.0	0.1	57.4	51.4	1.1
Stator sidewall	43.1	43.7	0.3	113.1	124.1	2.3	66.2	65.5	0.3	151.7	152 .3	0.1
Magnet front	44.4	46.1	0.9	130.9	132.5	0.3	58.0	61.7	1.5	168.8	173.7	0.9
Magnet right	11.4	12.2	0.4	26.8	29.1	0.5	29.2	29.7	0.2	65.7	70.5	0.8
Stator gap upper	97.7	106.1	4.5	259.5	278.5	4.1	137.8	143.4	2.2	330.2	338.5	1.5
Stator gap lower	33.0	36.4	1.8	62.9	65.3	0.5	45.0	45.3	0.1	81.3	77.5	0.7

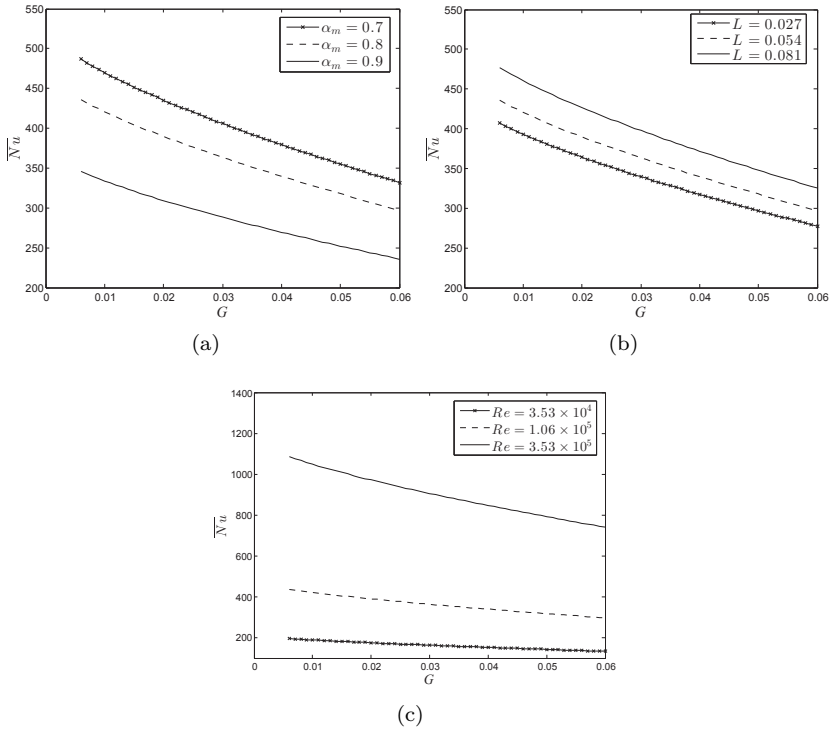

Figure 4.15: Variations of $\overline{Nu}$ versus G for *"Stator gap upper"* at different (a) α_m, (b) L and (c) Re.

4.3.4 Stator surface heat transfer

In YASA disk type electrical machines, more electromagnetic losses occur on the stator side. Therefore, the study of the convective heat transfer in this region is of much interest. Fig. 4.15 demonstrates the variations of the mean Nusselt number with G for the surface *"stator gap upper"* at various α_m, Re and L. Overall, it can be seen that the mean Nusselt number goes down with an increase in G and α_m, whereas the opposite trend is observed as L or Re increases. In order to evaluate properly the convective heat transfer in this study, it is equally important to examine the variations of the reference temperature as provided in Fig. 4.16. As can be seen from the graphs, the reference temperature decreases considerably with an increase in G, Re and L. In contrast, there is a consistent surge in the reference temperature when α_m goes up. The logic behind this trend is that the air-channel between the consecutive magnets would become narrow as the

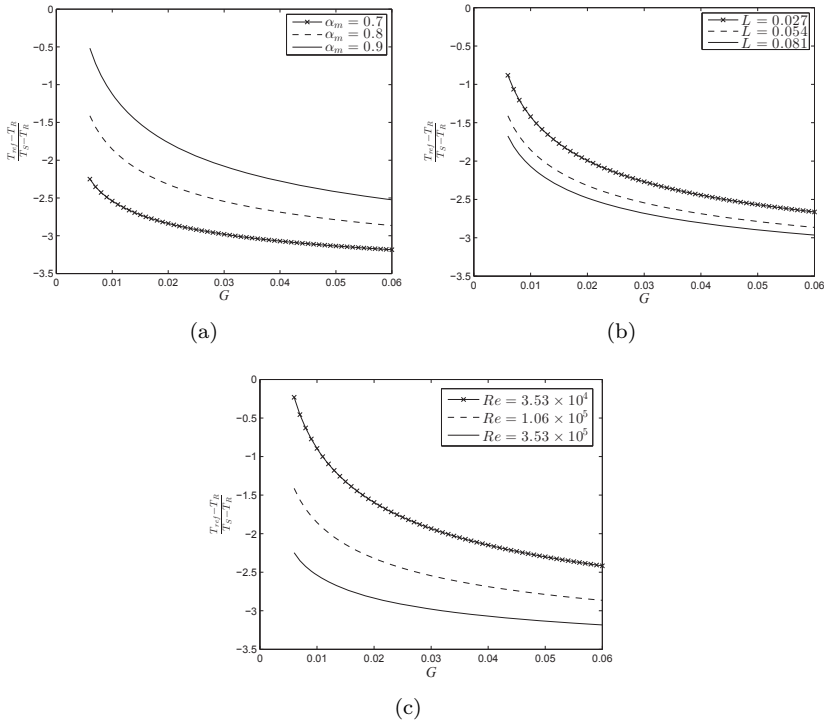

Figure 4.16: Variations of non-dimensional reference temperature versus G for *"Stator gap upper"* at different (a) α_m, (b) L and (c) Re.

magnet angle ratio enlarges and this results in less air being able to pass through the gap region and raising the reference temperature accordingly.

Fig. 4.17 indicates the variations of the convective heat transfer rate on *"stator gap upper"* surface versus G for different Re, α_m and L. The heat transfer rate experiences a sharp decline with an increase in α_m while an increase in Re or L improves the convective heat transfer significantly. The gap size ratio has a different influence on the variations of the heat transfer rate for the surface *"stator gap upper"*. In other words, the heat transfer increases as the gap size ratio becomes larger and reaches a maximum at $G \approx 0.02$. Once the gap size ratio increases further, there is a smooth decline in the convective heat transfer rate. This behaviour is mainly due to switching the flow pattern from Couette flow ($G \leq 0.02$) to Stewartson type, i.e., the transition from the narrow gap size to the wide gap size. Another reason for this trend is that an increase in G brings about a decline in the convective heat transfer coefficient, while also lowering the reference temperature for the stator surface (see Figs.4.15-4.16). These tendencies

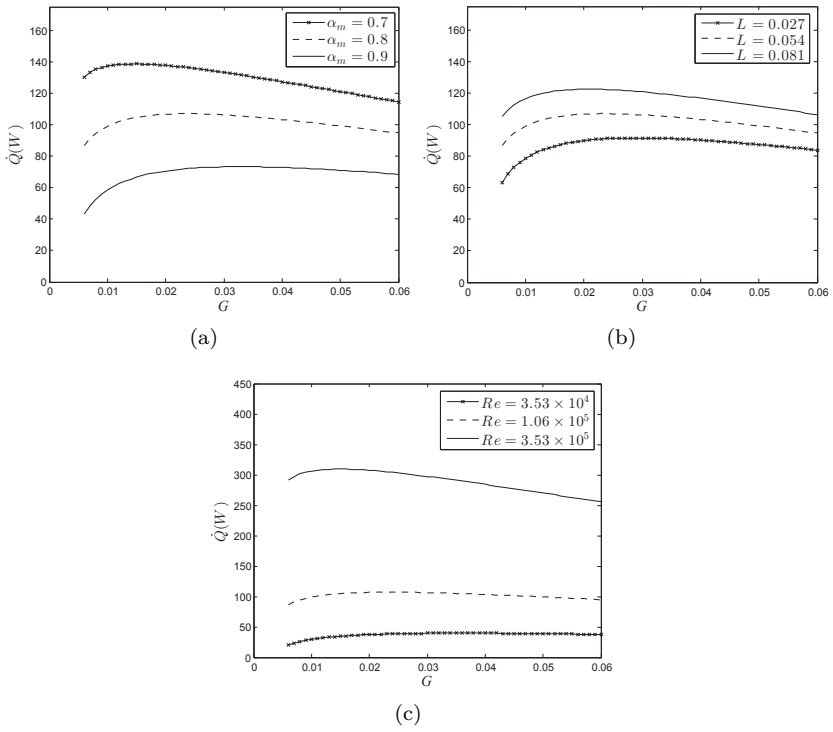

Figure 4.17: Variations of the convective heat transfer rate (W) for *"Stator gap upper"* versus G when $R_r = 74$ mm, $R_s = 84$ mm, $T_s = 120°$C and $T_r = 100°$C at different (a) α_m, (b) L and (c) Re.

have competing effects on the heat transfer rate, according to Eq.4.6. As a result, contrary to the findings of the simple rotor-stator system in an enclosed cylinder in Chapter 3, there is a gap size ratio, for a given Re, α_m and L, in which the convective heat transfer for the stator surface in the gap reaches a maximum. The same behaviour has been reported by Yuan et al. [131].

4.4 Conclusions

This chapter deals with the prediction of the convective heat transfer coefficients in the rotor-stator system of AFPMSMs. CFD simulations have been performed, considering different ranges of the predominant non-dimensional parameters that govern the heat transfer and fluid flow. Specifically, these are the rotational Reynolds number Re, the gap size ratio G, the magnet angle ratio α_m and magnet thickness ratio L. It was shown that the magnets forms radial air-channels by conducting the flow in between the space being made between the magnets and also into the gap region, so that it facilitates the cooling of the system. In addition to that, the existence of the annular opening was demonstrated to be equally important to the heat transfer in this configuration. By allowing the cold air to enter into the air-channels as well as through the air-gap, a net radial outflow from these channels becomes possible. This improves the cooling performance.

A minimization method by means of a Pattern-Search algorithm has been employed to find the proper value of the reference temperature that makes the estimated convective heat transfer coefficient the least dependent on the surface temperatures. It was shown that this approach is much more practical than using the ambient temperature for all surfaces, or using the bulk fluid temperature as the reference temperature. Using this reference temperature, the correlations for the Nusselt number for all surfaces were constructed.

The effects of important parameters on the overall heat transfer rate in the system were also investigated. It was shown that an increase in the Reynolds number and the magnet thickness ratio can significantly improve the cooling of the machine. On the other hand, there is a sharp decline in the overall heat transfer, e.g., a 40% drop in the stator surfaces heat transfer, as the magnet angle ratio goes up from 0.7 to 0.9. For a given Re, α_m and L, there is a gap size ratio for which the stator heat transfer rate in the gap reaches a peak.

In conclusion, the proposed correlations are quite versatile tools in the thermal modeling of AFPMSMs. The presented results in this chapter will be exploited in a coupled thermal and electromagnetic analysis to fulfill the complete design optimization of the AFPMSMs.

5

Windage losses modeling in an AFPMSM [1]

This chapter copes with the prediction of the power associated with the aerodynamic forces (viscous or pressure) on the rotary parts of the AFPMSM, so-called "windage losses". A set of correlations for the windage power losses prediction in the current machine is presented based on the numerical model. In the literature, it is quite common to use the empirical formulations of a simple rotor-stator arrangement to predict the windage power losses in a real disk type electrical machine. This has a significant drawback, as the windage loss caused by the magnets and air-channels between them is neglected. In this chapter, however, these effects are taken into account. Two categories of formulations are defined to make the windage losses dimensionless, based on whether the losses are due to the viscous forces or the pressure forces. Details of the proposed correlations and the results are discussed in the following sections.

[1] This chapter is written based on the journal paper: A. Rasekh, P. Sergeant and J. Vierendeels, "Development of correlations for windage power losses modeling in an axial flux permanent magnet synchronous machine with geometrical features of the magnets." Energies 9(12)2016, doi:10.3390/en9121009.

5.1 Numerical set-up

The CFD simulation presented in the Chapter 4 will be used to assess the windage power losses in the AFPMSM under investigation. Once again, the case of an air-gap thickness of 1.0 mm, a tip velocity of the magnets of 30 m/s, a magnet angle of 18°, a magnet thickness of 4.0 mm along with surface temperatures of $T_s = 120°C$ and $T_r = 100°C$, is chosen as a reference point for this CFD-parametric study.

5.1.1 Flow structure characteristic

The proper analysis of the windage loss requires detailed knowledge of the flow field. Indeed, the spatial distribution of the tangential velocity component determines the shear stress and therefore the contribution of the shear stress to the torque required to rotate the rotor disk. Fig. 5.1 depicts the tangential velocity contours in the midplane of the rotor-stator configuration at $G = 0.0135$, $Re = 1.06 \times 10^5$, $\alpha_m = 0.8$ and $L = 0.0540$. This figure highlights the strong tangential velocity gradient between the magnet and the stator surface in the air-gap.

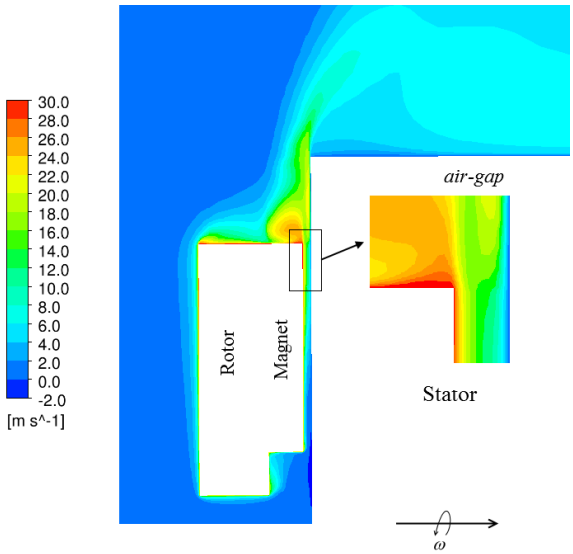

Figure 5.1: Absolute tangential velocity contour in the meridional plane through the center of the air-gap for $G = 0.0135$, $Re = 1.06 \times 10^5$, $\alpha_m = 0.8$ and $L = 0.0540$.

The contours of the relative tangential velocity at different radii in the air-channel are illustrated in Fig. 5.2. There is a significant gradient of the

tangential velocity across the air-channel, which implies a large shear stress at the wall. This elucidates the contribution of this region to the windage power losses of the machine. Furthermore, the positive and negative velocities in the air-channel demonstrate the presence of a vortex with radial core in this region.

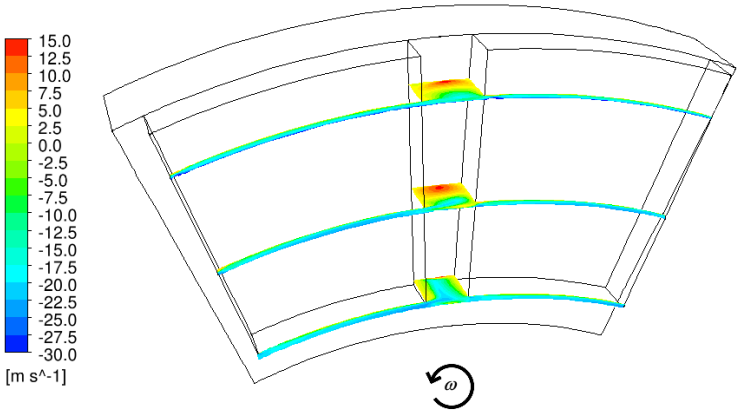

Figure 5.2: Relative tangential velocity contour across the air-channel for different radii at $G = 0.0135$, $Re = 1.06 \times 10^5$, $\alpha_m = 0.8$, and $L = 0.0540$. Positive values indicate a relative flow in the direction of the rotation.

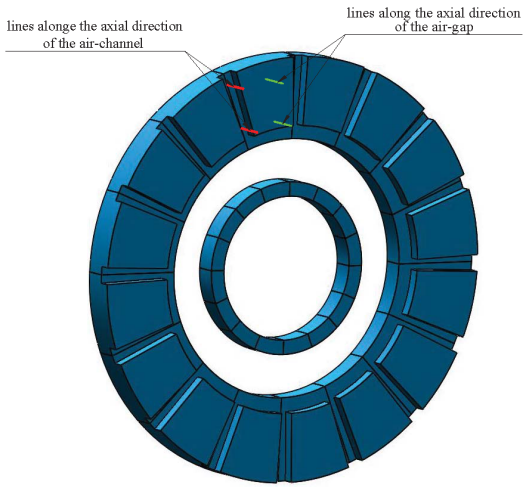

Figure 5.3: The schematic diagram of the rotor in an AFPMSM.

To give more insight about the shear stress for the current discoidal system, the non-dimensional tangential velocity variations across the air-

gap from the middle of the magnet to the stator surface (green lines in Fig 5.3) at different radii have been shown in Fig. 5.4. The left side of the axis belongs to the surface *"magnet front"* and the right side represents the stator surface in the gap. Two different flow patterns are observed according to the gap size. For the small gap size ratio ($G = 0.0068$), the gradient of the tangential velocity at the higher radii is rather constant, typical for Couette flow. For the wide gap size ($G = 0.0811$), however, the Stewartson type of flow is seen, i.e., the tangential component of the velocity is almost zero everywhere except for the rotor boundary layer.

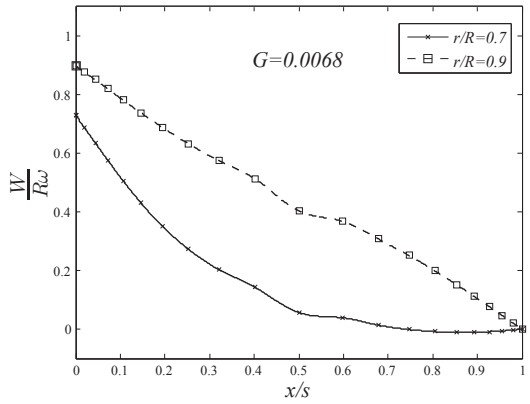

(a)

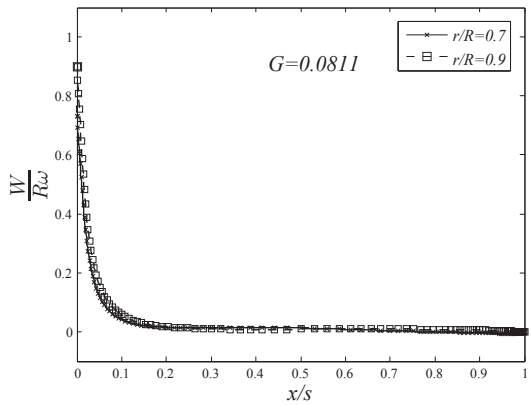

(b)

Figure 5.4: Non-dimensional tangential velocity ($\frac{W}{R\omega}$) across the air-gap (green lines in Fig. 5.3) at $Re = 1.06 \times 10^5$, $\alpha_m = 0.8$ and $L = 0.0540$ for (a) $G = 0.0068$, (b) $G = 0.0811$. The left side of the axis belongs to the surface *"magnet front"* and the right side represents the stator surface in the gap.

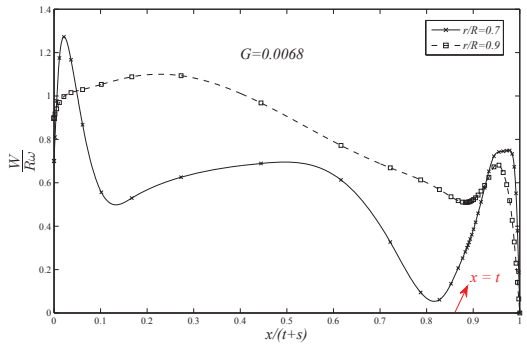

(a)

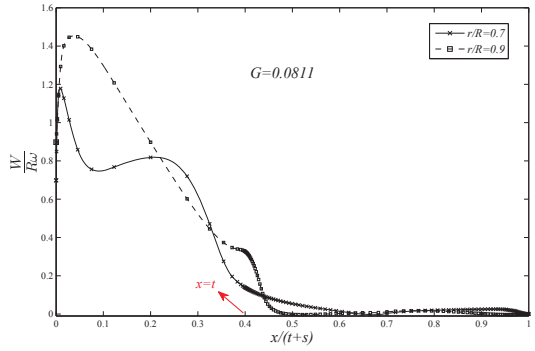

(b)

Figure 5.5: Non-dimensional tangential velocity ($\frac{W}{R\omega}$) across the air-channel (red lines in Fig. 5.3) at $Re = 1.06 \times 10^5$, $\alpha_m = 0.8$ and $L = 0.0540$ for (a) $G = 0.0068$, (b) $G = 0.0811$. The left side of the horizontal axis denotes the point on the surface *"Rotor facing stator"* in the middle between two magnets.

The variations of the non-dimensional tangential velocity alongside of the air-channel (the red lines marked in Fig. 5.3) are depicted in Fig. 5.5. The left side of the horizontal axis denotes the point on the surface *"Rotor facing stator"* in the middle between two magnets. It is remarked that away from the rotor surface towards the stator surface in the air-channel there is initially an increase in the tangential velocity magnitude, due to the presence of the vortex within the channel, generated by the friction with the stator wall. The implication of this trend is that the surface *"Rotor facing stator"* does not counteract the rotation of the disk. Moreover, the tangential velocity increases again after $x = t$ for the small G, whereas for larger gap sizes it keeps decreasing.

In addition to the shear stress contribution in the windage losses, torque is also generated due to pressure forces. Depending on the actual geome-

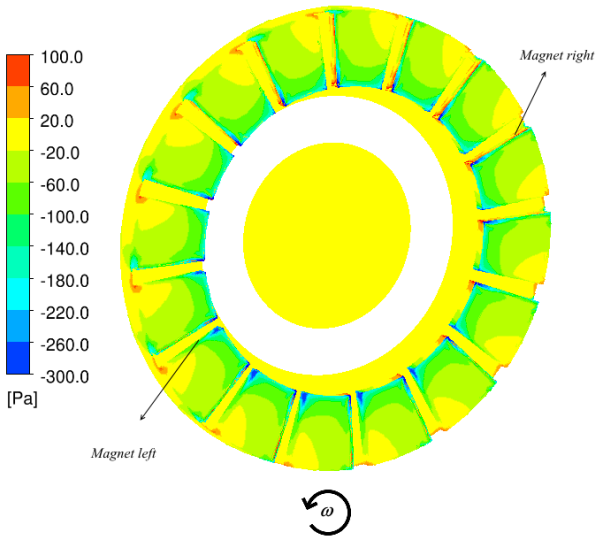

Figure 5.6: Static pressure contour on the rotor disk and the magnet at $G = 0.0135$, $Re = 1.06 \times 10^5$, $\alpha_m = 0.8$ and $L = 0.0540$.

try, this could give the largest contribution to the total torque. The static pressure contours on the rotor disk with the magnets on it have been illustrated in Fig. 5.6. The other magnets have been represented through post-processing of the periodic data. There is a noticeable pressure difference between the surface *"magnet left"* and *"magnet right"*, which in turn generates pressure forces acting against the rotary motion of the rotor disk. In this way, the side surfaces in the air-channel play an important role in the overall windage losses in the AFPMSM.

5.1.2 Total windage power losses

Fig 5.7 clarifies the influence of the gap size (s), the tip velocity of the magnet (v), the magnet angle (α) and the magnet thickness (t) on the overall windage power losses in the current arrangement.

Notice that the default values of these geometrical parameters here are $s = 1$ mm, $v = 30$ m/s, α=18° and $t = 4$ mm, which are indicated with the red dots in the figures. This reference point is equivalent to $G = 0.0135$, $Re = 1.06 \times 10^5$, $\alpha_m = 0.8$ and $L = 0.0540$. The overall losses have been computed by accumulating the losses generated at each individual surface. The results of Fig 5.7 account for one rotor disk. The parametric study reveals that the rise of the rotational Reynolds number from 3.5×10^4 to 3.5×10^5 enormously increases the total windage losses from 0.2 to 220

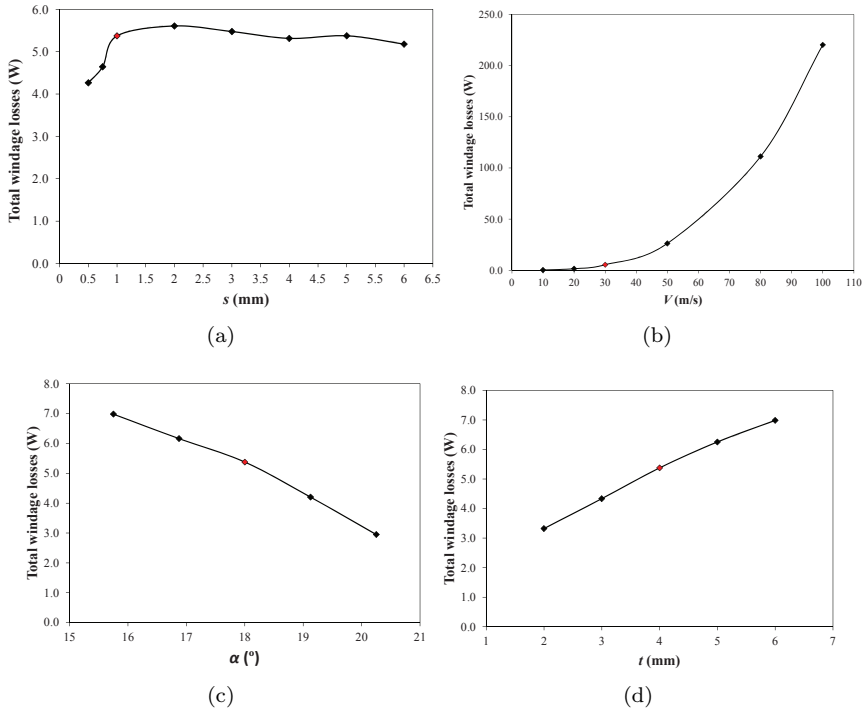

Figure 5.7: The influence of (a) gap size s(mm) (b) tip velocity of the magnets v(m/s) (c) magnet angle $\alpha(^\circ)$ and (d) magnet thickness t(mm) on the overall windage power losses (W) per rotor (reference point is highlighted with the red point).

W. Additionally, the iron losses in terms of excess, hysteresis, and dynamic losses substantially increase with an increase in the rotational speed [141]. This also gives rise to more copper losses, as the skin effect in the windings increases with frequency. Furthermore, the permanent magnet losses (Eddy currents losses) increase for greater values of the rotational speed [5].

The same trend, but much less profound, can be seen with variations of the magnet thickness ratio. The total windage losses increase by more than double as the magnet thickness ratio L varies from 0.0270 to 0.0811. The reason behind this behavior is that the increase of the magnet thickness rises the contact area between the airflow and the magnet. Not only does this area triple in size, but that this area, although relatively small, has a big impact on the losses because pressure is working there. However, from the electromagnetic point of view, thicker PMs lead to greater air-gap flux density, resulting in a more efficient machine. At a certain point, an

additional increase in the PM thickness will bring about additional cost without any added value to the electromagnetic performance [5].

By contrast, as the magnet angle α enlarges from 15.75° to 20.25 ° (α_m varies from 0.7 to 0.9.), the overall windage power losses diminish by about 60%. The implication is that a wider magnet angle shrinks the total size of the air-channel, resulting in a decrease in the air mass flow rate inside the air-channel between the consecutive magnets. This lowers the windage losses. In view of the electromagnetic analysis, a wider PM magnet angle results in a more air-gap flux density as well as a more efficient machine. This, however, increases the volume of the PMs, which in turn raises the PM losses [5].

The gap size ratio exhibits a discernible trend, i.e., there is a growth in the overall windage losses, in the course of the transition from the very narrow gap to the wide gap size. As the gap size becomes larger, the value of the windage losses remains almost unchanged. It can be deduced that the gap size greater than nearly 2 mm does not affect the amount of the air mass flow rate entering into the air-channel. The overall windage losses are therefore also not affected. The same trend was reported by Luo et al. [82]. Unlike for the windage loss, an increase in the air-gap distance, while keeping the same PM width, deteriorates the electromagnetic performance of the machine [5].

5.2 Correlations for windage losses

The purpose of the CFD simulations is not only to perform the parametric study, but more importantly, to construct correlations for the overall windage power losses in an AFPMSM. As shown before in Fig. 4.2, there are eleven surfaces at the rotor disk, namely hole lower, hole upper, rotor facing stator, rotor left side, magnet front, magnet lower, magnet left, magnet right, magnet upper, rotor sidewall and shaft. These are surfaces that contribute to the overall windage losses in the machine. The idea is to find formulations for the windage losses of each surface as a function of the gap size ratio, the rotational Reynolds number, the magnet angle ratio and the magnet thickness ratio. To make the correlations applicable for different scales of the AFPMSMs, it is required to express the windage losses as non-dimensional numbers. Since the windage losses occur as a result of two different sources, namely the viscous forces and the pressure forces, two distinct non-dimensional numbers should be defined. The windage power losses can be expressed as the following function,

$$P = f(\mu, \rho, \omega, R) \tag{5.1}$$

where R is the outer radius of the rotor, which is also the length scale of the machine. According to the dimensional analysis, the non-dimensional windage power losses $P^{'}$ can be written as,

$$P^{'} = P_f \mu^a \rho^b \omega^c R^d \tag{5.2}$$

P_f denotes the windage losses generated in surface f, μ is dynamic viscosity of air and ρ represents air density.

The windage losses due to viscous forces scale proportional to the viscosity. Therefore, a is chosen to be -1. From this should then follow that $b = 0$. The other coefficients follow from the requirement that $P^{'}$ should be dimensionless. Thus, the non-dimensional windage losses due to the viscous forces on the surface f are expressed as,

$$P^{'}_{f,\nu} = \frac{P_f}{\mu \omega^2 R^3} \tag{5.3}$$

The non-dimensional windage losses due to pressure forces scale proportionally to the density. Thus, b is chosen to be -1. From this should then follow that $a = 0$. In the same manner, the unknown coefficients can be obtained by considering dimensional analysis. After that, the non-dimensional windage losses due to the pressure forces on the surface, f, are given by the following formulation,

$$P^{'}_{f,\rho} = \frac{P_f}{\rho \omega^3 R^5} \tag{5.4}$$

In above formulations, $P^{'}_{f,\nu}$ and $P^{'}_{f,\rho}$ are the non-dimensional windage losses for surface f due to viscous forces and pressure forces, respectively.

Only two surfaces in this arrangement, namely *"magnet left"* and *"magnet right"*, give rise to windage losses due to the pressure forces. The rest of the surfaces contribute to the windage losses only because of the viscous forces. As a matter of fact, for both surfaces *"magnet left"* and *"magnet right"* the contribution of the viscous forces is even negligible, which explains the different choices of variables to make the contribution to the power dimensionless for these surfaces.

To construct the correlations, a set of CFD simulations are performed for $G = \{0.0068, 0.0101, 0.0270, 0.0405, 0.0541, 0.0676, 0.0811\}$, while the other parameters are kept at the reference point, i.e. $\{Re = 1.06 \times 10^5$, $\alpha_m = 0.8$, $L = 0.0540\}$. Afterwards, $P^{'}_{f,\nu}$ and $P^{'}_{f,\rho}$ are computed according to Eqs.(5.3-5.4). By doing so, the variations of the windage power losses with G when other parameters are fixed at the reference point are obtained. The same procedure as explained for G, is repeated when Re, α_m and L are being changed. In this way, the variations of $P^{'}_{f,\nu}$ and $P^{'}_{f,\rho}$ for each corresponding

surface within the machine at different non-dimensional parameters will be known. In the end, it is necessary to provide formulations to express the non-dimensional windage losses as follows,

$$\begin{aligned} P_{f,\nu}^{'} &= Z_f\left(G, Re, \alpha_m, L\right) \\ P_{f,\rho}^{'} &= X_f\left(G, Re, \alpha_m, L\right) \end{aligned} \tag{5.5}$$

where the functions Z_f and X_f need to be defined. It is assumed that these functions with four variables can be rewritten as the product of four functions with one variable as,

$$\begin{aligned} P_{f,\nu}^{'} &= P_{f,v}^{'*} z_{f,1}(G) \times z_{f,2}(Re) \times z_{f,3}(\alpha_m) \times z_{f,4}(L) \\ P_{f,\rho}^{'} &= P_{f,\rho}^{'*} x_{f,1}(G) \times x_{f,2}(Re) \times x_{f,3}(\alpha_m) \times x_{f,4}(L) \end{aligned} \tag{5.6}$$

where the superscript $*$ represents the values of $P_{f,\nu}^{'}$ and $P_{f,\rho}^{'}$ at the reference point. To find all of the above functions with one variable, curve fitting for each case should be carried out one after the other. The output from each function at the reference point is almost one. As discussed, there are two categories of surfaces in the current system: those where the windage losses are only a result of the viscous forces and those where the windage losses are almost entirely due to the pressure forces. The details of the formulations with respect to this classification of the surfaces are demonstrated in Tables 5.1-5.2.

Table 5.1: Correlations to estimate the windage losses (W) due to viscous forces.

Surface	hole lower, $f = 1$	hole upper, $f = 2$	Rotor facing stator, $f = 3$	Rotor left side, $f = 4$	Magnet front, $f = 5$	Magnet lower, $f = 6$	Magnet upper, $f = 9$	Rotor sidewall, $f = 10$	Shaft, $f = 11$
$P^{*}_{f,v}$	5.600	42.108	-20.796	420.403	251.028	62.156	27.902	150.382	2.868
$z_{f,1}$	$0.6065G + 1.004$	$1.505G + 0.9783$	$-4.389 \times 10^{-7} G^{-2.942} + 1.112$	1	$0.8593G + 0.9902$	$-1.9016G^{0.4745} + 1.231$	$0.6994G^{-0.09581}$	$1.894G + 0.9848$	$11.76G + 0.8452$
$z_{f,2}$	$6.144 \times 10^{-6} Re + 0.3495$	$5.225 \times 10^{-6} Re + 0.4248$	$-17.19Re^{-0.07896} + 7.895$	$6.423 \times 10^{-6} Re + 0.3119$	$6.324 \times 10^{-6} Re + 0.3254$	$0.0007882Re^{0.6173}$	$1.023 \times 10^{-5} Re - 0.08718$	$7.285 \times 10^{-6} Re + 0.2174$	$4.432 \times 10^{-6} Re + 0.5308$
$z_{f,3}$	$-0.6796\alpha_m + 1.57$	$-0.6358\alpha_m + 1.502$	$-8.61\alpha_m^{4.393} + 4.212$	$0.2052\alpha_m + 0.8358$	$3.551\alpha_m^{23.38} + 0.9882$	$3.551\alpha_m^{23.38} + 0.9882$	$1.854\alpha_m^{9.287} + 0.7816$	$-0.7086\alpha_m + 1.579$	$-0.144\alpha_m + 1.114$
$z_{f,4}$	$-0.7068L + 1.035$	$0.664L + 0.9677$	$-7311L^{3.265} + 1.518$	$0.4958L + 0.9742$	$2.715L + 0.8581$	$20.74L - 0.1176$	$13.88L + 0.2696$	$2.688L + 0.8593$	$9.633L + 0.4791$

Table 5.2: Correlations to estimate the windage losses (W) due to pressure forces.

Surface	Magnet left, $f = 7$	Magnet right, $f = 8$
$P^{'*}_{f,\rho}$	0.02218	0.00527
$x_{f,1}$	$0.688G^{-0.2192} - 0.7961$	$-0.01947G^{-1.104} + 3.299$
$x_{f,2}$	$0.1116Re^{0.1866}$	$-1.633 \times 10^{8} Re^{-1.806} + 1.121$
$x_{f,3}$	$-3.876\alpha_m + 4.101$	$-7.127\alpha_m^{10.56} + 1.645$
$x_{f,4}$	$142.4L^{1.703}$	$-1.708 \times 10^{4} L^{3.453} + 1.733$

5.2.1 Robustness of the correlations

The verification presented in the chapter 4 (section 4.3.3) show the reliability of the CFD modeling used in this study. The correlations for the windage losses have been obtained by varying one non-dimensional parameter while keeping the other parameters at the reference point and repeating this for all the other variables. Therefore, to check the robustness of the correlations, the comparison should be made with CFD simulations for the cases where neither G, Re, α_m nor L are at the reference point. Table 5.3 demonstrates these comparative studies for four different cases. It is seen that the percentage error, $Error\% = |\frac{P_{f,CFD} - P_{f,Correlation}}{P_{Overall,CFD}}| \times 100$ is less than 3%, which indicates the good fit of the presented correlations. The numerator represents the difference between the estimated windage losses on the surface, *f*, through CFD simulation and those predicted by proposed correlations. Moreover, the denominator refers to the overall windage losses through CFD simulation, which can be obtained by summing up the losses for each surface within the machine. The values of windage losses for the surface *"Rotor facing stator"* are negative, corresponding to the case where the flow was helping the rotary motion of the rotor disk as explained above in Fig 5.5. According to the data in Table 5.3, the proportion of the windage losses due to pressure forces is dominant as a whole in the AFPMSM under investigation.

The results of the correlations for windage losses due to viscous forces for the surfaces in the gap are also compared with the results reported by Wrobel et al. [84] in Fig. 5.8, and an agreement with 25% average deviation is observed. It should be mentioned that the computational domain is slightly different from the case in this chapter as the rotor with magnets along with the stator disk are enclosed in a box with the prescribed ambient temperature. It can be concluded that the correlations presented in this chapter are able to assess accurately the windage power losses for all surfaces in the practical ranges of the important parameters in AFPMSMs.

Table 5.3: Comparison between the CFD and the proposed correlations results for windage losses (W) at different cases when $R_r = 74$ mm.

Surface	$Re = 8.931\times10^4$, $G = 0.0203$, $L = 0.0338$, α_m=0.77			$Re = 2.322\times10^5$, $G = 0.0203$, $L = 0.0338$, α_m=0.77			$Re = 1.210\times10^5$, $G = 0.0108$, $L = 0.0642$, α_m=0.82			$Re = 1.901\times10^5$, $G = 0.0108$, $L = 0.0642$, α_m=0.82		
	Proposed Correlations	CFD	Error%	Proposed Correlations	CFD	Error%	Proposed Correlations	CFD	Error%	Proposed Correlations	CFD	Error%
hole lower	0.005	0.005	0.01	0.067	0.070	0.00	0.012	0.012	0.00	0.041	0.040	0.00
hole upper	0.039	0.037	0.07	0.478	0.457	0.00	0.087	0.083	0.00	0.277	0.276	0.00
Rotor facing stator	-0.055	-0.041	0.51	-0.747	-0.428	0.01	-0.005	-0.013	0.00	-0.022	-0.039	0.00
Rotor left side	0.365	0.355	0.34	5.096	4.888	0.00	0.891	0.878	0.00	3.113	3.052	0.00
Magnet front	0.204	0.206	0.07	2.809	2.811	0.00	0.562	0.548	0.00	1.940	1.897	0.00
Magnet lower	0.031	0.029	0.06	0.392	0.356	0.00	0.156	0.160	0.00	0.508	0.522	0.00
Magnet left	0.649	0.727	2.68	15.897	15.281	0.01	6.811	6.599	0.03	28.085	27.861	0.01
Magnet right	1.522	1.494	0.97	35.777	30.536	0.08	-0.719	0.170	0.11	-2.686	0.627	0.10
Magnet upper	0.020	0.016	0.14	0.316	0.297	0.00	0.062	0.082	0.00	0.214	0.327	0.00
Rotor sidewall	0.144	0.128	0.56	1.963	1.888	0.00	0.324	0.325	0.00	1.141	1.170	0.00
Shaft	0.002	0.002	0.00	0.024	0.026	0.00	0.006	0.006	0.00	0.019	0.020	0.00

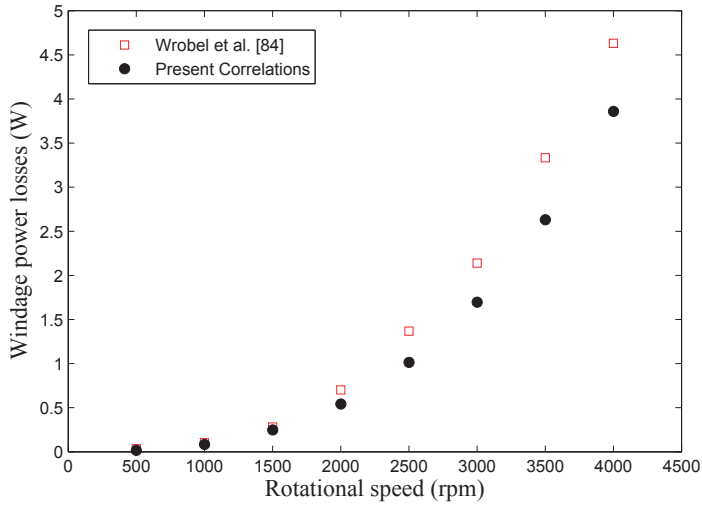

Figure 5.8: Comparison the results of the windage losses due to viscous forces for surfaces in the gap region with the data reported by Wrobel et al.[84] at $G = 0.0156$, $L = 0.0376$ and $\alpha_m = 0.8$.

5.2.2 Windage losses at magnet surfaces

Since a great part of the windage power losses is associated with the magnet surfaces, the surfaces *"magnet front"* and a combination of *"magnet left"* and *"magnet right"* are precisely investigated in this section. The surface *"magnet front"* contributes to the windage losses as a result of the viscous forces, whereas the other ones are responsible for the windage losses due to pressure forces.

Figs. 5.9-5.10 illustrate the variations of $\acute{P_\nu}$ and $\acute{P_\rho}$ versus G for the surfaces *"magnet front"* and the sum of surfaces *"magnet left"* and *"magnet right"* at various non-dimensional parameters, respectively. It is perceived that $\acute{P_\nu}$ slightly increases with G, which can be attributed to the transition from the narrow gap to the wide gap size (see Fig. 5.4). The same reasoning as for $\acute{P_\nu}$ can be applied to the variation of $P_\rho^{'}$ for the side surfaces of the magnet, as more air is allowed to enter to the air-channel. For the wide gap size ratio, however, the flow path is shifted away more into the air-gap as compared to the air-channel region which slightly reduces the value of $P_\rho^{'}$ for the side surfaces of magnets, i.e., *"magnet left"* and *"magnet right"*. In similar manner, the influence of the magnet angle is inferred. In fact, higher α_m implies that less air enters into the air-channel, so that $P_\rho^{'}$ declines with increasing α_m. The opposite trend is observed for the variations of $\acute{P_\nu}$. Both $\acute{P_\nu}$ and $P_\rho^{'}$ increase with increasing L, as and increase in the magnet

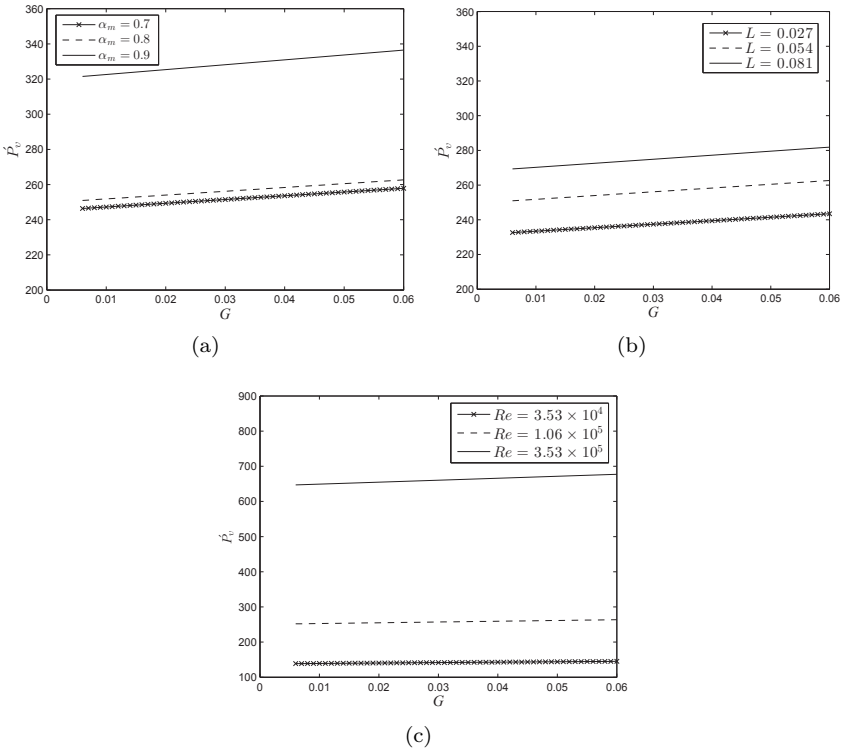

Figure 5.9: Variations of the dimensionless viscous power, $\acute{P}_\nu$, versus G for the *"magnet front"* surface at different values of (a) magnet angle ratio, (b) magnet thickness ratio and (c) rotational Reynolds number.

thickness results in more air passing between rotor and stator. An increase of the rotational Reynolds number makes $\acute{P}_\nu$ and $P_\rho^{'}$ larger, although the latter is less affected. The effect of the rotational Reynolds number is greatly noticeable for the windage losses due to viscous force; i.e., variations of $\acute{P}_\nu$.

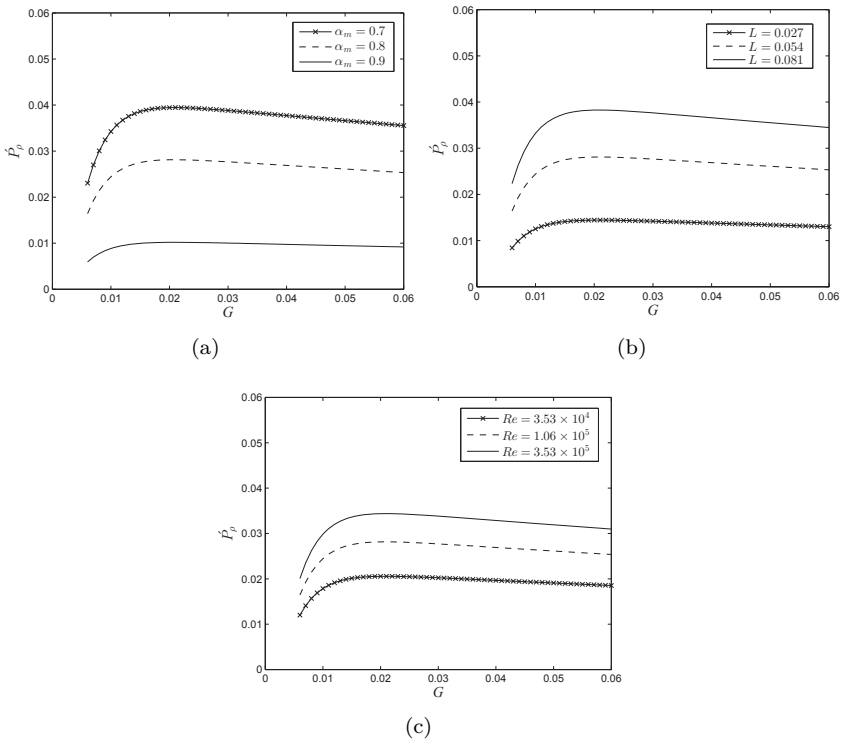

Figure 5.10: Variations of the dimensionless pressure power, $\acute{P}_p$, versus G for the sum of side surfaces of the magnet (*"magnet left"* and *"magnet right"*) at different values of (a) magnet angle ratio, (b) magnet thickness ratio and (c) rotational Reynolds number.

5.3 Conclusions

The windage power losses in an AFPMSM have been studied in this chapter. 3-D CFD simulations of the rotor-stator configuration with 16 magnets on the rotor disk were carried out with the aid of the Frozen Rotor method. The importance of the geometrical parameters of the magnets on the flow fluid and their contribution on the overall windage losses in the machine were analyzed.

The variations of the tangential velocity component demonstrated that there exist two types of flow structures in the air-gap between the magnet and stator surface, i.e., the Couette flow for the narrow gap and the Stewartson flow for the wide gap size ratio. Furthermore, the results of the parametric study indicate that an increase in the Reynolds number from

3.5×10^4 to 3.5×10^5 substantially increases the overall windage losses. The total windage losses become more than double as the magnet thickness ratio goes up from from 0.0270 to 0.0811. In contrast to variations of Re and L, the total windage losses drop by 60%, when the magnet angle ratio increases from 0.7 up to 0.9. The influence of the magnet geometrical parameters on the cooling improvement in the machine has been discussed in the previous chapter, and these effects counterbalance the windage power losses variations. As a result, a compromise should be made between the cooling system and the windage power losses in the design process of the machine.

In order to make the windage losses dimensionless, two formulations were introduced according to the cause of the losses whether they are due to the viscous forces or the pressure forces. Novel correlations for predicting the windage losses for the entire machine were constructed, through the curve fittings of the numerical data. The proposed correlations in this chapter are useful in the design of the AFPMSMs. These correlations along with those presented in the chapter 4 for the convective heat transfer coefficients will be employed in a coupled thermal, electromagnetical and mechanical losses analysis to fully optimize the performance of the machine.

6

Influence of curved-shape magnets on the performance of an AFPMSM

As mentioned in Chapter 4, the rotor disk with the magnets on it in an AFPMSM could act as radial air-channels to the circulation of the cooling flow. This matter becomes even more significant in the YASA topology as it consists of two rotor disks. In order to take full advantage of this effect, the influence of the curved-shape magnets instead of the conventional PMs with trapezoidal shape on the cooling flow characteristics are studied in this chapter. Within this context, only a few studies have been carried out in the literature. As an example, Fawzal et al. [142] performed a comparative study of different fan blade designs of the rotor disk for the cooling of AFPMSM through CFD simulations along with the experimental analysis. They indicated that while the backward-inclined design is appropriate for the windage losses, the radial design results in the better thermal performance with a cost of greater value of windage losses.

In this chapter, several arbitrary pairs of the rotor disk with their respective curved-shape magnets are considered as the case-study. CFD simulations are performed to discover the thermal performance and the windage power losses variations. A conjugate heat transfer calculation is performed to estimate the steady state surface temperature of the rotor and the stator in the full load of the machine. Furthermore, an experimental analysis is conducted by manufacturing various dummy rotor disks having the same curved-shape magnets as used in the CFD modeling. The purpose of the

conjugate heat transfer calculation here is not to predict the exact temperatures of the disks, but to implement the comparative study to figure out the influence of the curved-shape magnets on the cooling performance of the machine. The results reveal that a careful choice of the angles of the curved-shaped PMs could enhance the machine performance.

6.1 Problem description

Fig. 6.1 schematically displays the rotor-stator configuration in the YASA topology of an AFPMSM. As mentioned earlier, the YASA topology is made of two rotor disks surrounding the stator with very tiny air-gaps. The geometrical characteristics of the machine are listed in Table 6.1. For the sake of cooling effectiveness, there is an annular opening in the rotor disk as indicated in chapter 4. Trapezoidal magnets, forming the radial channels, are typically used in the AFPMSMs. In this research, however, curved-shape magnets are being considered (see Fig. 6.1). It should be noted that the actual geometry was unknown when studying the radial channel.

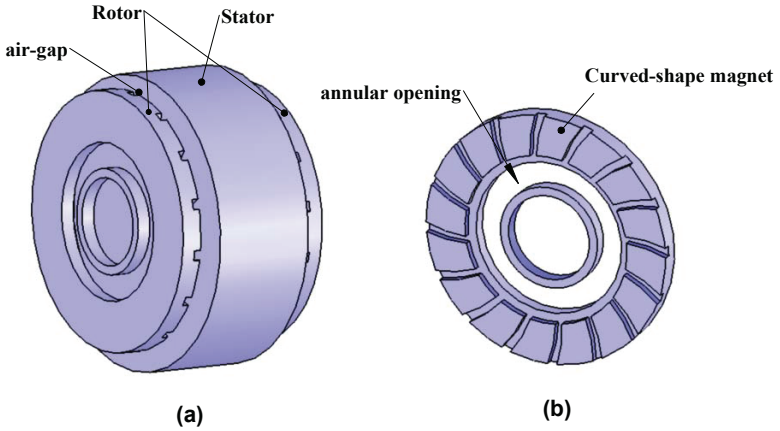

Figure 6.1: (a) The schematic diagram of the YASA type of the AFPMSM (b) Rotor disk with curved-shape magnets.

Fig. 6.2 gives the geometrical details of one complete curved-shape magnet (front view). The curvature type on the both sides of the magnets is a parabola which is defined by three points: 1) the inner vertex of the magnet (the same as when the trapezoidal magnet is used), 2) the shoulder of the arc, defined by θ_1, 3) the tip vertex of the magnet, given by θ_2. The magnet angle (α) is kept constant at 18° along the radial direction.

Five cases are being considered in this work including

Table 6.1: The geometrical features of the AFPMSM under study.

Parameter	**value (mm)**
Air-gap thickness	1.0
Magnet thickness	4.0
Axial length of Rotor	8.0
Axial length of Stator	60
Radial length of Magnet	24
Shaft diameter	50
Outer radius of Rotor	74
Outer radius of Stator	84
Inner radius of Opening	30
Outer radius of Opening	45

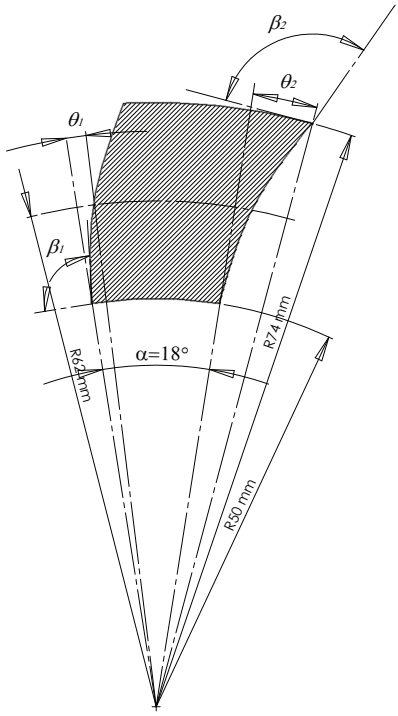

Figure 6.2: The detailed front-view of the curved-shape magnet ($0 < \theta_1$, $0 < \theta_2$) (The rotation direction is counter-clockwise.).

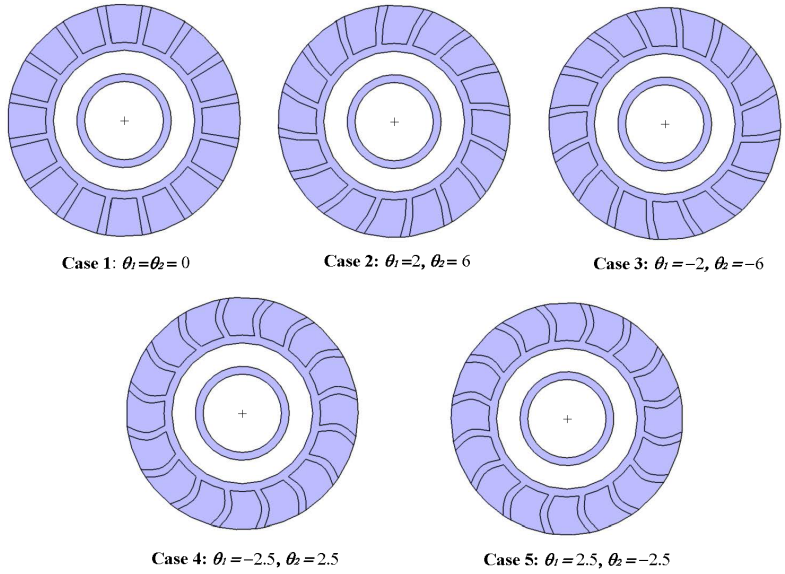

Figure 6.3: The schematic of the rotor disks with their distinct magnet shapes. (The rotation direction is counter-clockwise.)

- Case 1: trapezoidal magnet ($\theta_1 = \theta_2 = 0°$) with ($\beta_1 = \beta_2 = 0$)
- Case 2: ($\theta_1 = 2°$, $\theta_2 = 6°$) with ($\beta_1 = 100.19°$, $\beta_2 = 110.20°$)
- Case 3: ($\theta_1 = -2°$, $\theta_2 = -6°$) with ($\beta_1 = 79.81°$, $\beta_2 = 69.98°$)
- Case 4: ($\theta_1 = -2.5°$, $\theta_2 = 2.5°$) with ($\beta_1 = 69.10°$, $\beta_2 = 122.67°$)
- Case 5: ($\theta_1 = 2.5°$, $\theta_2 = -2.5°$)with ($\beta_1 = 110.90°$, $\beta_2 = 57.33°$)

The rotation direction in Fig. 6.3 is counter-clockwise. The corresponding blade angles in turbomachinery are also indicated, where β_1 is the angle made by the magnet at inlet, with the tangent to the inlet radius, and β_2 represents the magnet angle with the tangent at outlet of the air-channel. The graphical illustrations of these rotor disks with their distinct shape of the magnets are shown in Fig. 6.3. In the experiment, for cases 3 & 5, the same disks are used as for the cases 2 & 4, but the rotor is rotated clockwise.

6.2 Experimental Set-up

An AFPMSM prototype, shown in Fig. 6.4, is manufactured to evaluate the thermal performance of the machine. The main characteristics of this

Table 6.2: The characteristics of the machine used in the test set-up.

Parameter	**Value**	**Unit**
Rated Power	4.0	kW
Rated Speed	2000	rpm
Rated frequency	333.3	Hz
Rated Torque	19	N.m
Number of Magnets	16	-
Number of stator slots	15	-
axial length slot	60	mm
Slot width	12	mm

test set-up are listed in Table 6.2. Note that it has the same geometrical features as in the CFD modeling (see Table 6.1). This prototype is used as a generator. It is powered by an induction machine, and the rotational speed is controlled by an industrial inverter. This experimental study has been performed at the laboratory by colleagues within the scope of a common project [5, 14].

The body of the rotor disk is also made of aluminium. On the stator side, the heat is generated by Joule losses. At full load of the machine, about 100 W power loss is present in the entire stator. The experiments are conducted at rotational speeds of 1000 and 2000 rpm. Temperature sensors are inserted in the test set-up to measure the temperature at different parts of the machine. An infrared temperature sensor ZTP-135SR is used to measure the rotor temperature. To record the stator winding temperature, a PT100 platinum resistance thermometer is placed inside it. The room temperature of the laboratory where the measurement carried out is around 25°C. In order to ensure that the machine has reached the thermal steady state condition, the temperatures are monitored with time. Typically, a steady state temperature was reached after 2.5 hours of running time.

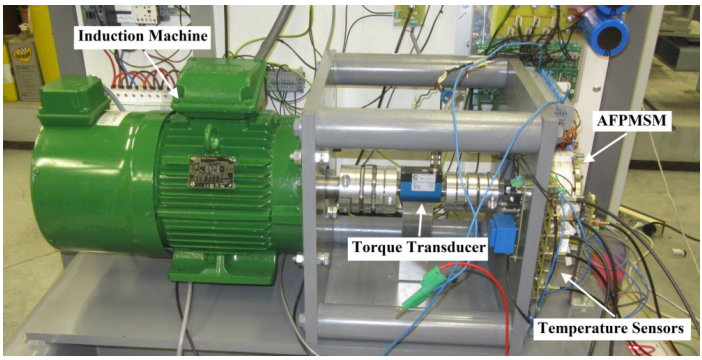

(a)

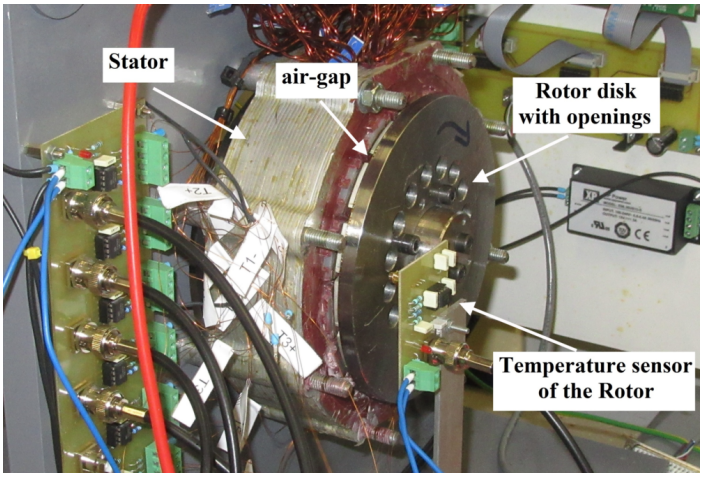

(b)

Figure 6.4: (a) Experimental set-up (b) close-up of the prototype.

6.3 CFD simulations

The objective of the presented numerical modeling is to predict the rotor and stator temperatures with various curved-shape magnets in the working conditions of the AFPMSM. The magnets on the rotor disks are evenly distributed so that the channels being made between the successive magnets occupy equal volumes. Due to the geometrical periodicity, the computational domain contains 1/16 of the rotor-stator arrangement. In addition to this, only half of the stator with one rotor disk is considered while using a symmetry plane in the middle of the stator.

The generations of the 3-D computational grid and the CFD simulations

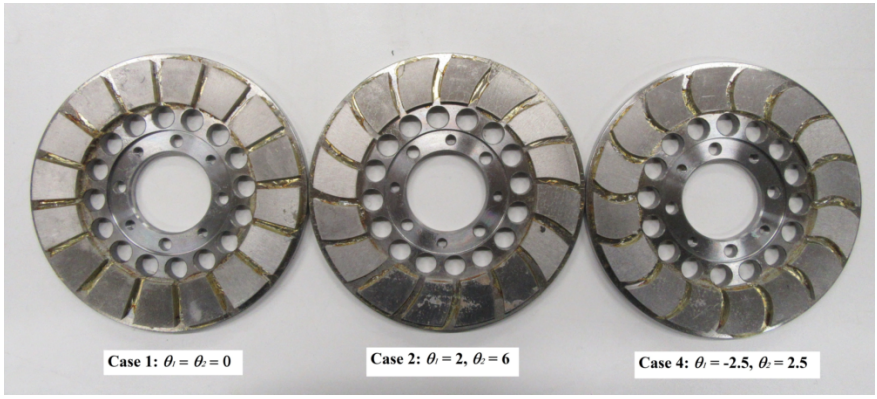

Figure 6.5: The rotor disks with dummy magnets used in the experiment.

are carried out by Ansys FLUENT software. E.g. for case 2, the structured computational mesh contains more than 3,800,000 cells. The distance of the first node to the solid wall of the rotor is chosen in a way that the value of y^+ is kept below unity. Furthermore, a mesh independency study has successfully been performed.

The computational domain for this numerical simulation looks like the one presented in Fig. 4.3 with the exception that the solids parts such as the rotor and the stator are also included. The atmospheric pressure boundary is placed far away from the rotor. The stator is assumed to be made of copper, having the same properties as the winding. Therefore, it is expected that the rotor and the stator will achieve uniform temperatures due to their high thermal conductivities. A comparative study of different curved-shape magnets is presented. The focus of this work is to discover the contribution of the curved-shape magnets on the heat dissipation from the machine through convection heat transfer. Thus, the conduction heat transfers towards the shaft and through the support of the stator are not taken into account in the numerical modeling.

The losses in the machine are introduced in the thermal model as volumetric heat sources in the solid parts. Conjugate heat transfer (CHT) calculations are performed, as the flow and heat transfer of the cooling air should be solved at the same time with the energy equation in the solid domain. As a matter of fact, the governing equations in each of the fluid and the solid regions are solved iteratively. The fluid/solid interfaces are employed to couple the energy equations between the fluid and solid domain to ensure the continuity of temperature and the conservation of energy. The objective is to find out the steady state temperatures in the rotor and the stator. This allows obtaining the temperatures in the rotor and the stator

for a given heat generation rate, instead of needing to impose temperatures on isothermal surfaces.

The same numerical modeling approach presented in Chapter 4 is used here. The steady state governing continuity, momentum and energy equations for the fluid domain will be as follows,

$$\nabla.(\rho_f \overrightarrow{v_r}) = 0 \tag{6.1}$$

$$\nabla.\,(\rho_f \overrightarrow{v_r} \otimes \overrightarrow{v}) + \rho_f(\overrightarrow{\Omega} \times \overrightarrow{v}) = -\nabla p + (\mu + \mu_t)\nabla^2 \overrightarrow{v} \tag{6.2}$$

$$\nabla.\left(\rho_f \overrightarrow{v_r} h_f + p(\overrightarrow{\Omega} \times \overrightarrow{r})\right) = \nabla.\,((k_f + k_t)\nabla T) \tag{6.3}$$

In the above, $\overrightarrow{v_r}$ is the relative velocity with respect to the rotating frame, $\overrightarrow{v}$ is the absolute velocity in the stationary frame, $\overrightarrow{\Omega}$ represents the rotational velocity vector of the rotating domain, ρ_f indicates the air density, h_f is the specific enthalpy of air, μ is molecular viscosity and μ_t is the turbulent viscosity, k_f is air thermal conductivity and k_t denotes the turbulent thermal conductivity. The turbulent properties are computed from the $k-\omega$ SST turbulence model.

Inside the solid region, the energy equation is written as,

$$\nabla.\,(k_s \nabla T) + S_h = 0 \tag{6.4}$$

where S_h represents the volumetric heat source, and k_s is thermal conductivity of the solid parts. It is assumed that the thermal conductivities of the machine parts comprising the rotor, the magnet and the stator are uniform, isotropic and constant with temperature.

6.4 Results and discussion

In this section, the consequences of using curved-shape magnets on the thermal efficiency and the windage losses are elaborately discussed.

6.4.1 Thermal performance

As far as AFPMSMs are concerned, the thermal modeling is always the main design issue, due to the compact structure of the machine. The attention here goes to the influence of the curved-shape magnets on the flow structure of the cooling air and how this affects the thermal performance of the machine.

6.4.1.1 Cooling air characteristics

A good way of improving the efficiency of the cooling system is to induce flow from the surrounding cooler air into the motor. It was shown in Chapter

4 that the more surrounding air is directed towards the channels between the consecutive magnets and the air-gap region, the more cooling can be achieved. Given the critical role of these areas, the results of the flow structure and heat transfer for different curved-shape magnets are compared with each other.

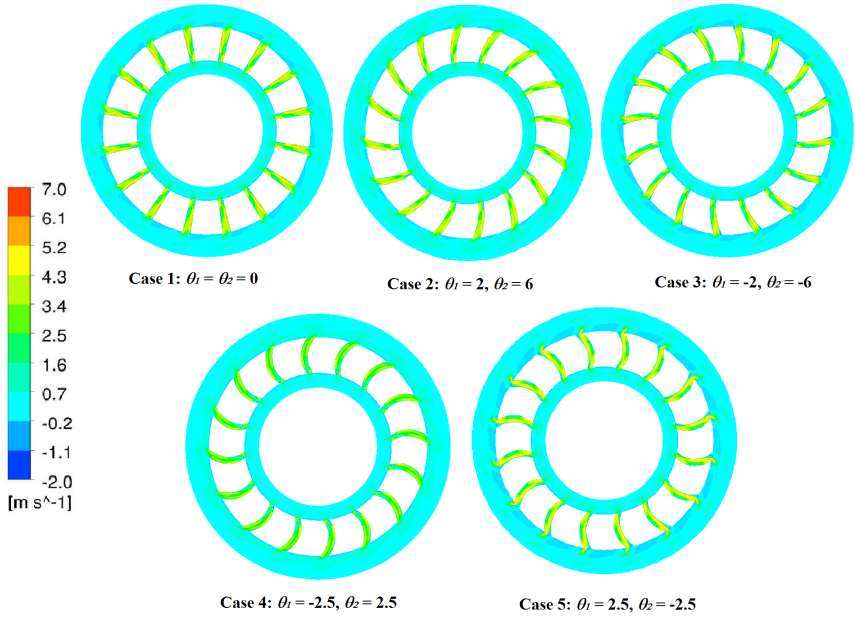

Figure 6.6: Radial velocity contours in the air-channel for various curved-shape magnets at $\omega = 1000$ rpm. (The rotation direction is counter-clockwise.)

Fig. 6.6 elucidates the contour of the radial velocity in the air-channel for several curved-shape magnets at rotational speed of 1000 rpm when the direction of the rotation is counter-clockwise. It is observed that the use of the rotor disk case 5 ($\theta_1 = 2.5, \theta_2 = -2.5$) results in the strongest radial outflow at the periphery of the air-channel, whereas the application of the case 4 ($\theta_1 = -2.5, \theta_2 = 2.5$) leads to the weakest airflow directed in the space between the magnets.

To gain more detailed insight about the flow field, Table 6.3 provides the data for the incoming mass flow rate of the cooling air to the machine passing through the annular opening with different curved-shape magnets. It is found that the case 5 ($\theta_1 = 2.5, \theta_2 = -2.5$) gives rise to the highest mass flow rate of the cooling air for both rotational speeds of 1000 and 2000 rpm. These findings support the results observed in the radial velocity contour alongside the air-channel. From this Table, it is also seen that the

trapezoidal magnets are the second best. Therefore, it can be concluded that having the curved-shape magnet does not necessarily enhance the amount of the cooling air entering to the AFPMSM as compared to the trapezoidal magnets, and it is the shape of the curvature that plays the essential role.

Table 6.3: Mass flow rate (kg/s) passing through the annular opening for various curved-shape magnets and rotational speeds.

	different curved-shape magnets				
Rotational speed (rpm)	$(\theta_1 = \theta_2 = 0)$	$(\theta_1 = 2,\ \theta_2 = 6)$	$(\theta_1 = -2,\ \theta_2 = -6)$	$(\theta_1 = -2.5,\ \theta_2 = 2.5)$	$(\theta_1 = 2.5,\ \theta_2 = -2.5)$
1000	0.00116	0.00111	0.00102	0.00095	0.00118
2000	0.00282	0.00265	0.00250	0.00223	0.00297

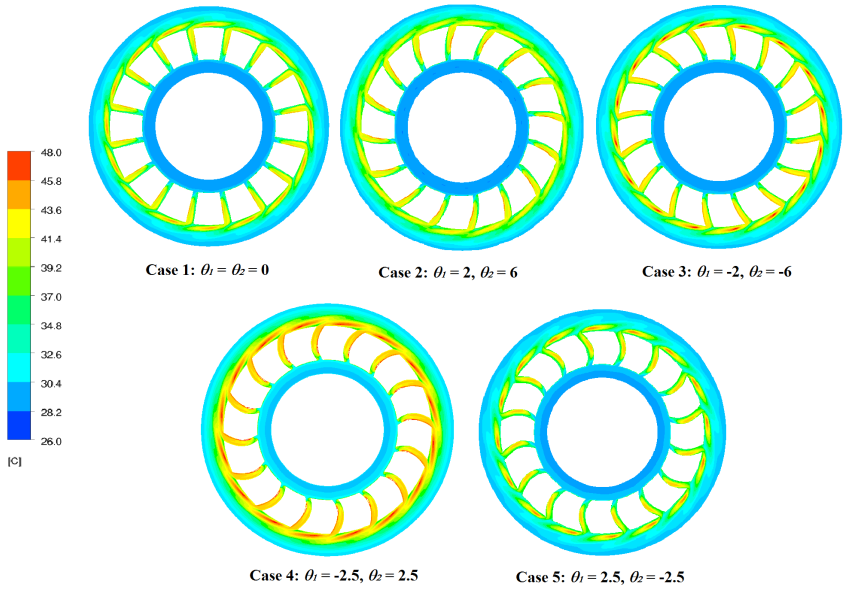

Figure 6.7: Temperature contours in the air-channel for various curved-shape magnets at $\omega = 1000$ rpm. (The rotation direction is counter-clockwise.)

Besides the effects of the curved-magnet on the flow structure, the trends for the air temperature distribution are equally important. Fig. 6.7 illustrates the temperature contours in the air-channel between the magnets when each of the five disks is utilized. The use of the curved-shape magnets with $(\theta_1 = 2.5, \theta_2 = -2.5)$ leads to coldest air in this region as compared to other rotor disks examined here. By contrast, the curved-shape magnet with $(\theta_1 = -2.5, \theta_2 = 2.5)$ brings about the highest air temperature in the air-channel. The lower air temperature represents the effectiveness of the

corresponding rotor disk in the heat losses evacuation.

6.4.1.2 Temperature development in rotor and stator

The measured values of the steady state temperatures of the rotor disk and the stator, together with the CFD modeling results, are used to evaluate the effectiveness of the curved-shape magnets in the full load of the prototype.

Fig. 6.8 demonstrates the temperatures of the rotor and the stator from CFD modeling and the measurement data at the rotational speeds of 1000 and 2000 rpm. The results of CFD simulations for the rotor temperature agree well with the experimental data at 1000 rpm. It is found that the use of the rotor disk with the curved-shape magnet of ($\theta_1 = 2.5, \theta_2 = -2.5$) leads to the lowest temperature of the rotor, i.e., about 33.3°C at 1000 rpm, even though the temperature reduction is not very remarkable. The difference between the maximum temperature of the rotor disk with ($\theta_1 = 2.5, \theta_2 = -2.5$) and the minimum temperature achieved by the curved-shape magnet of ($\theta_1 = -2.5, \theta_2 = 2.5$) is less than 3°C according to the measured data at the rotational speed of 1000 rpm. This difference becomes even smaller once the rotational speed reaches 2000 rpm.

From the experimental data, due to an increase in the rotational speed from 1000 to 2000 rpm, the stator winding temperature drops from 56°C to about 48°C when the trapezoidal magnets ($\theta_1 = \theta_2 = 0$) are used. The CFD results over-predict this temperature drop in the stator winding, e.g., around 20°C for trapezoidal magnets. Note that the same amount of heat losses in the stator is present in the CFD model and the experiment. While in the numerical model the heat losses are evacuated to the surrounding only by means of convection, the conduction heat transfer towards the support, along with the convention to air, is considered in the heat exchanges in the experiment. As a results, the impact of the conduction heat transfer, which is excluded in the CFD simulation, has to be compensated with the greater calculation of the temperature drop in the stator as well as in the rotor.

Similar to the results for the temperature of the rotor disk, it can be deduced from both the numerical and the experimental results that the use of the rotor disk with the curved-shape magnet of ($\theta_1 = 2.5, \theta_2 = -2.5$) brings about the lowest stator winding temperature (about 47°C at 2000 rpm) as compared to other magnets examined in this work.

In order to evaluate the conduction heat transfer away from the stator surfaces, the convection heat transfer rates given by the proposed correlations in Tables 4.3-4.4 in Chapter 4 are subtracted from the total heat losses in the stator. To do so, the steady state temperatures of the rotor and the stator from the experiment are introduced to the correlations. The results for rotational speed of 1000 and 2000 rpm are presented in Table 6.4.

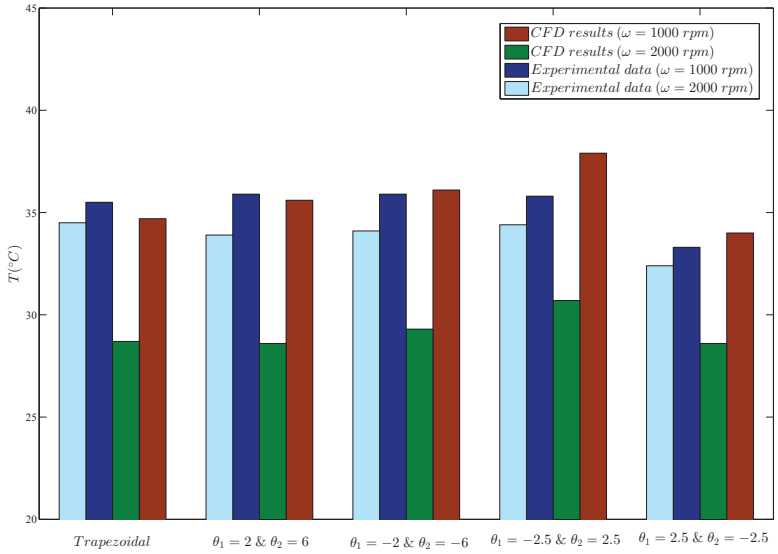

(a) Rotor temperature

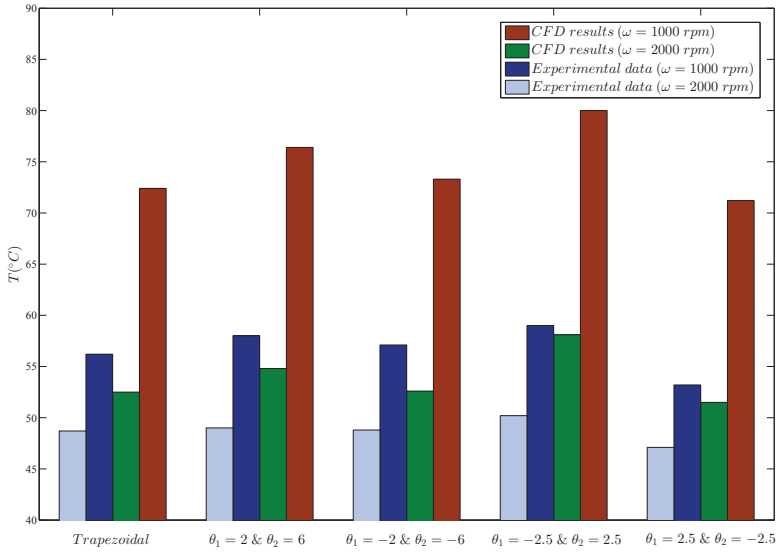

(b) Stator temperature

Figure 6.8: Comparison between the results of CFD simulations and the experimental data according to various curved-shape magnets (a) rotor temperature (b) stator temperature.

The total heat loss for the half of the stator is 50 W. From Table 6.4, the conduction heat transfer away from stator surfaces can be given by subtracting these data from total heat losses. It is seen that with an increase in the rotational speed from 1000 to 2000 rpm the conduction heat transfer from the stator will decrease about 8.5 W, and this has to be evacuated mainly through convection.

Table 6.4: The convective heat transfer rates (W) for the stator surfaces (half of the machine).

Surface:	Rotational speed (rpm)	
	1000	2000
Stator gap upper	18.5	23.7
Stator gap lower	7.0	7.8
Stator sidewall	6.3	8.8
Overall stator surfaces	31.8	40.3

In an alternative way, the conduction heat transfer towards the support, which is made of four connecting rods, can be calculated. These rods in the support resembles to the fins with uniform circular cross-sectional area. The base temperature of the fin equals to the stator surface temperature, i.e., $T(0) = T_{stator}$ and the tip temperature of the fin corresponds to the ambient temperature $T(L) = T_\infty$. The conduction heat transfer in each of the connecting rod is evaluated from the following expression [Incropera [143]],

$$q_c = M \frac{\sinh mL}{\cosh mL} \tag{6.5}$$

In the above equation, $m = \sqrt{\frac{hP}{kA_c}}$ and $M = \sqrt{hPkA_c}(T_{stator} - T_\infty)$, A_c is the cross section area of the fin, P is the fin perimeter, h is the natural convection coefficient, which can be obtained from the equation recommended by Churchill and Chu [144],

$$h = \left[0.60 + \frac{0.387 Ra_D^{1/6}}{\left[1 + (0.559/Pr)^{9/16}\right]^{8/27}} \right]^2 k/D \tag{6.6}$$

where Ra_D is the Rayleigh number based on the fin diameter. Given the dimension of the connecting rod (D=0.06 m & L=0.31 m) and the stator temperatures from the experiments, it is found that there is a decrease of 6 W in the conduction heat transfer in the rods (from 21 to 15 W), when the rotational speed increases from 1000 to 2000 rpm. Therefore, the analysis

presented in Table 6.4 over-predicts the decrease in the conduction away from stator disk with the percentage error of about 5 % (scaling with the overall heat generation in the stator).

6.4.2 Windage losses evaluation

Another issue that can be affected by the curved-shape magnets is the windage power loss. The total windage losses are evaluated by accumulating the power associated with the aerodynamic forces (viscous or pressure) against rotary parts of the machine. It was shown in Chapter 5 that mainly pressure forces are responsible for the windage losses for the side surfaces in the air-channel, whereas for the surfaces facing the stator surface in the gap, obviously only viscous forces contribute to the windage losses.

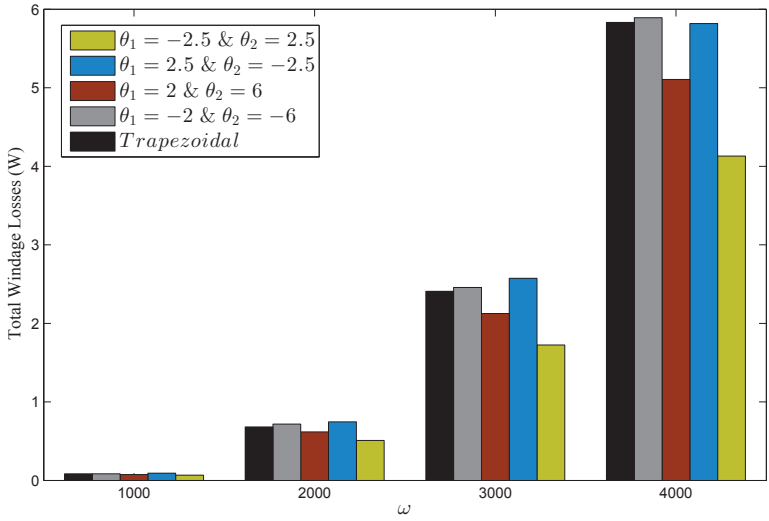

Figure 6.9: The overall windage losses in the AFPMSM for various curved-shape magnets at different rotational speeds.

Fig. 6.9 discloses the effect of the curved-shape magnets on the overall windage losses in the machine at different rotational speeds, based on the results of the CFD simulations. The lowest values of the windage losses can be achieved by using the curved-shape magnet with $(\theta_1 = -2.5, \theta_2 = 2.5)$. This trend is very noticeable at the higher rotational speed, e.g., at 4000 rpm. Furthermore, the forward curved rotors (Case 3 & Case 5) result in greater windage power losses as compared to the backward curved rotors (Case 2 & Case 4), which is quite expected from the turbomachinery point of view [145]. This tendency could be attributed to the stronger radial flow

by using forward curved rotor disk, shown in Fig. 6.6.

6.5 Conclusions

This chapter dealt with the effect of the curved-shape magnets at the rotor disk on the performance of the YASA topology of the AFPMSM. Five pairs of rotor disks with their distinct dummy magnets were considered as the case-study. Given the heat losses as the input to the thermal model, conjugate heat transfer calculations were implemented to assess the steady state temperature of the rotor and stator. Moreover, CFD simulations were used to evaluate the overall power requirements to spin the rotor disk, i.e., the windage power losses. An experimental analysis was also undertaken by manufacturing the same rotor disks with the curved-shape magnets as in the numerical thermal modeling.

The results revealed that the strongest radial outflow at the periphery of the air-channel with the coldest air in this region is achieved for the curved-shape magnet with ($\theta_1 = 2.5, \theta_2 = -2.5$). It was also shown that to attain the lowest windage losses the curved-shape magnet with ($\theta_1 = -2.5, \theta_2 = 2.5$) could be the best choice among the other magnets tested here. From the CFD results, an increase in rotational speed of the rotor from 1000 to 4000 rpm results in the windage losses increase from 0.08 to 5.8 W.

The steady state temperature of the rotor and stator were measured and calculated for the various curved-shape magnets at different rotational speeds. The measurement data indicated that there is about 8°C temperature reduction in the stator winding for the trapezoidal magnets when the rotational speed goes up from 1000 to 2000 rpm. The CFD results over-predicted this temperature drop (about 20°C) as the heat generated in the stator disk was assumed to be evacuated through convection to the surrounding and the effect of the conduction heat transfer towards the support has compensated in this way.

From both the CFD results and the experimental data, it was demonstrated that the use of the rotor disk with the curved-shape magnets ($\theta_1 = 2.5, \theta_2 = -2.5$) results in the lowest temperature on the rotor and stator. However, the temperature differences between the best choice of the rotor disk with the worst one is not very remarkable, e.g. only about 3°C in the stator temperature at 2000 rpm.

In short, defining an optimal shape of the curved-shape magnet at the rotor disk represents a trade-off problem that should be solved by finding the compromise between the thermal performance and the windage losses. For the application presented here, the case of the curve-shape magnet with ($\theta_1 = 2.5, \theta_2 = -2.5$) is recommended for the cooling purposes, whereas the choice of ($\theta_1 = -2.5, \theta_2 = 2.5$) is advantageous in the windage power losses point of view.

7 Concluding Remarks

7.1 Conclusions

The convective heat transfer in an axial flux permanent magnet synchronous machine (AFPMSM) was considered in this work. Among the different topologies of this type of electrical machine, a yokeless and segmented armature (YASA) topology was taken into account, as it possesses an excellent power density and energy efficiency. The YASA machines have extensive flexibility not only at high-speed-low-torque but also at low-speed-high-torque applications. The former is typical for wind turbine applications as the major source of clean and sustainable energy supply. In this regard, any improvement in the performance of the AFPMSMs can make a great impact on the wind turbine industry. For further development of such a machine, the fundamental understanding of contributors to the losses are absolutely essential. While the electromagnetic aspects of the machine have been well addressed in the literature, the thermal modeling of the AFPMSM is still debatable. For instance, the lack of fast and robust formulations to predict convective heat transfer coefficients in such machines is evident. As a result, the objective of this thesis was to numerically investigate the cooling flow characteristics in the machine. To that purpose, this research was divided into three main parts as follows,

- Convective heat transfer in the simple discoidal system
- Flow and heat transfer in the rotor-stator configuration of the AF-

PMSMs

- Effect of the curved-shape magnets on the cooling flow features of the AFPMSMs

After presenting the general goals in Chapter 1, this thesis was proceeded with an elaborate literature study in Chapter 2 regarding the thermal aspects of the disk-type electrical machine in particular AFPMSMs. From the overview of the preceding studies, it was shown that the air-gap convection can greatly attribute to the heat losses evacuation in these machines. For convenience, most authors have used the ambient temperature as the reference temperature to calculate the convective heat transfer coefficients in air-gap of the rotor-stator systems, which has a serious drawback [132–136, 107]. In fact, their proposed correlations become dependent on the ambient temperature and the surface temperatures, making their applications limited to that certain case. To resolve this issue, different approaches were considered in this thesis.

The first step in this research was towards the understanding the heat transfer and flow structure in a rotor-stator system enclosed in a cylindrical cover, representing a simplified discoidal system in a disk-type electrical machine. To that end, CFD simulations were performed in the range of rotational Reynolds number $4.19 \times 10^4 \leq Re \leq 4.19 \times 10^5$ and the gap size ratio $0.00333 \leq G \leq 0.08$. The results of this parametric study demonstrated that the average stator heat transfer in the gap could improve at the narrow air-gap size. It was concluded that there is a gap size ratio for a given Reynolds number for which the average convective heat transfer on the stator surface in the gap reaches a minimum. Furthermore, the presence of the holes at the rotor disk was found to be advantageous to the stator heat transfer in the gap region as air is allowed to enter into the air-gap through the holes, resulting in a net radial flow in between the rotor and stator.

An innovative approach to formulate the convective heat transfer coefficients in this discoidal configuration was presented in Chapter 3, based on the CFD results. In the context of the appropriate choice for the reference temperature, the average bulk fluid temperature adjacent to the corresponding surface was used instead of the ambient temperature. By doing so, the proposed correlations for the convective heat transfer coefficient for the surfaces in the gap would be independent of the ambient temperature as well as the surface temperature. Given the physical and the geometrical parameters such as the disk diameter, the air-gap size, the rotational speed of the rotor along with the surface temperatures as the input to the thermal model, the proposed correlations could accurately yield the convective heat transfer

rate for all the surfaces within the system. A comparison was also made with available data in the literature and good agreement was found. Furthermore, these correlations were successfully applied in a coupled thermal and electromagnetic analysis in an AFPMSM [14].

In Chapter 4, the flow and heat transfer in the rotor-stator configuration of the YASA topology AFPMSM were investigated, considering the presence of trapezoidal magnets. The case-study here was composed of an open rotor-stator with sixteen magnets at the periphery of the rotor with an annular opening in the entire disk. In addition to the rotational Reynolds number and the gap size ratio, it was found that two more non-dimensional numbers, the magnet angle ratio and magnet thickness ratio, contribute to the overall heat transfer and flow structure in this system. CFD simulations by means of the Frozen Rotor (FR) concept were carried out in the practical dimensionless ranges of these geometrical parameters. The magnets on the rotor could act as radial channels by conducting the flow in between the space being made between the magnets and also into the gap region, so that it would facilitate the cooling of the machine. The existence of the annular opening was demonstrated to be also effective for the cooling purpose. The results revealed that an increase in the Reynolds number and the magnet thickness ratio could tremendously enhance the evacuation of heat losses from the machine, whereas there was a sharp decline in the overall heat transfer, e.g. a drop of 40% in the stator surfaces heat transfer, as the magnet angle ratio goes up from 0.7 to 0.9. On the other hand, there was a gap size ratio, for a given Re, α_m and L, at which the stator heat transfer in the gap reached a peak.

Another objective of Chapter 4 was to construct the parametrized formulations for the convective heat transfer coefficients according to the aforementioned non-dimensional parameters. It was no longer a good choice to consider the average bulk fluid as the reference temperature to estimate the heat transfer coefficient when the magnets appeared on the rotor disk. To tackle this issue, a minimization method by means of a Pattern-Search algorithm was developed to find the proper value of the reference temperature. In this way, the estimated convective heat transfer coefficient became approximately independent of the surface temperatures. It was concluded that the proposed thermal model is a sophisticated and quite versatile tool in the thermal modeling of an AFPMSM. These correlations are exploited in the coupled thermal and electromagnetic analysis to fulfill the complete design optimization of the machine [5].

The study in Chapter 5 focused on assessing the windage power losses in an AFPMSM using the numerical modeling presented in Chapter 4. The variations of the tangential velocity component showed that there exist two

types of flow structures in the air-gap between the magnet and stator surface, that is, the Couette flow for the narrow gap and the Stewartson flow for the wide gap size ratio. It was found that the total windage losses becomes more than double as the magnet thickness ratio goes up from 0.0270 to 0.0811. By contrast, the losses decrease by 60% as the magnet angle ratio increases from 0.7 up to 0.9. From these trends, one may discover that the effect of the magnet geometrical parameters on the cooling system counterbalances the windage power losses variations. As a consequence, the compromise should be made between the cooling performance and the windage power losses together with the electromagnetic performance in the design of the AFPMSM.

As for the derivation of the correlations for the convective heat transfer coefficients, the goal was to have fast and robust formulations for the windage power losses in the machine. To this end, two formulations were introduced to make the windage losses dimensionless according to whether the losses are due to the viscous forces or the pressure forces. It was deduced that the pressure forces are responsible for the windage losses for the side surfaces in the air-channel, whereas for the surfaces facing the stator surface in the gap, only the viscous forces contribute to the windage losses. Novel correlations for predicting the windage losses for the entire machine were constructed by curve fitting the CFD results. The proposed correlations in this chapter, together with those presented in the chapter 4 for the convective heat transfer coefficients, could pave the way for the full coupled optimization of this type of electrical machine.

The focus of Chapter 6 was on the effect of curved-shape magnets on the performance of the YASA type AFPMSM. The cooling performance is improved with better, aerodynamically designed shapes of the magnets. The case-study in this Chapter considered five pairs of rotor disk with their distinct curved-shape magnets. Conjugate heat transfer calculations were carried out to assess the steady state temperatures of the rotor and the stator according to various curved-shape magnets. Additionally, the overall windage power losses were estimated for these cases. An experimental analysis was undertaken by manufacturing the same rotor disks with the curved-shape magnets as used in the CFD modeling. The measured data demonstrated that stator temperature decreases from 56.2 to 48.7°C with an increase in the rotational speed increases from 1000 to 2000 rpm by using the trapezoidal magnets. It was concluded that the thermal performance of the machine could be enhanced by using the curved-shape magnet with $(\theta_1 = 2.5, \theta_2 = -2.5)$, although this rotor disk has larger windage losses as compared to other magnets studied in this research.

7.2 Suggestions for future work

In this thesis, some important aspects in the thermal modeling of AFPMSMs have been highlighted. The results presented here shed light on possible future work as well as possibilities for further improvement of advanced design codes for such devices.

First of all, future research on the accurate prediction of the transition from laminar to turbulent flow is necessary in the modeling of the rotor-stator system. Future exploration on using CFD transition modelling in this geometry is inevitable. Currently, a RANS method was used to handle turbulent flow. The LES method could also be applied to gain the fundamental insight to the flow field, although it is computationally intensive.

The influence of the surface roughness on the heat transfer and flow model was not included in this work. It would be interesting to investigate this in the wall modeling of the CFD simulations. The full computational model of the stator was considered as a cylinder which is made of copper with a uniform thermal conductivity. This deserves further research in terms of the non-uniform conductivities for the stator slot and end winding in the conjugate heat transfer calculations. Moreover, the conduction heat transfer towards the shaft would be an interesting area for further work.

This study did not cover the radiation heat transfer because of the relatively low temperature of the machine. There is significant scope for further investigation on the applications where radiation heat transfer in the rotor-stator arrangement has to be considered.

The proposed correlations for the convective heat transfer in the machine were given for the machine with 16 magnet poles. An interesting area of investigation is to develop the model in such a way that it accounts for the variable number of the magnets.

It will also be a good research topic to study water cooling for this prototype and calculate the temperature of the machine components and compare it with the results of this work.

List of Figures

List of Tables

Bibliography

[1] W. Fei, P. Luk, and K. Jinupun. A new axial flux permanent magnet segmented-armature-torus machine for in-wheel direct drive applications. *Power Electronics Specialists Conference*, pages 2197–2202, 2008.

[2] F. Giulii Capponi. Recent advances in axial-flux permanent-magnet machine technology. *IEEE Trans. Ind. Appl*, 48(6):2190–2205, 2012.

[3] A. Di Gerlando, M. Foglia, M. Felice Iacchetti, and R. Perini. Parasitic currents in structural paths of YASA axial flux PM machines: Estimation and tests,. *IEEE transactions on Energy Conversion*, 31(2):750–758, 2016.

[4] G. Ahmad and U. Amin. Design, construction and study of small scale vertical axis wind turbine based on a magnetically levitated axial flux permanent magnet generator. *Renewable Energy*, 101:286–292, 2017.

[5] A. Hemeida. Electromagnetic and thermal study of axial flux permanent magnet synchronous machines. *Doctoral Thesis, Ghent University*, 2017.

[6] S. Chapman. Electrical machinery fundamentals. *4th Ed. New York: McGraw Hill*, 2005.

[7] H. Vansompel. Design of an energy efficient axial flux permanent magnet machine. *Doctoral Thesis, Ghent University*, 2013.

[8] Y. Chen, P. Pillay, and A. Khan. Pm wind generator comparison of different topologies. *AS Annual Meeting (IEEE Industry Applications Society*, page 1405–1412, 2004.

[9] M.U. Lamperth, A. Beaudet, , and M. Jaensch. Disc motors for automotive applications. *IET Hybrid and Eco-Friendly Vehicle Conference (HEVC)*, 2008.

[10] K.R. Pullen, M.R. Etemad, and M.R. Fenocchi. The high speed axial flux disk generator unlocking the potential of automative gas turbine.

IEE Colloquiu on Machines and Drives for Electric and Hybrid Vehicles, pages 1–4, 1996.

[11] J.R. Bumby and R. Martin. Axial-flux permanent-magnet air-cored generator for small-scale wind turbines. *IEE Proceedings-Electric Power Applications*, 152(5):1065–1075, 2005.

[12] F. Caricchi, F. Crescimbini, and O. Honorati. Low cost compact PM machine for adjustable speed pump application. *IEEE IAS'96*, 152(5):464—470, 1996.

[13] C. Debruyne, P. Sergeant, J. Desmet, L. Vandevelde, S. Derammelaere, J. Pyrhönen, and M. Polikarpova. Evaluation of the efficiency of line start permanent magnet machines as function of the operating temperature. *IEEE Trans. Ind. Electron*, 61(8):4443–4454, 2014.

[14] H. Vansompel, A. Rasekh, A. Hemeida, J. Vierendeels, and P. Sergeant. Coupled electromagnetic and thermal analysis of an axial flux PM machine. *IEEE Transactions on Magnets*, 51(11):8108104, 2015.

[15] A. Rasekh, P. Sergeant, and J. Vierendeels. Convective heat transfer prediction in disk-type electrical machines. *Applied Thermal Engineering*, 91:778–790, 2015.

[16] A. Rasekh, P. Sergeant, and J. Vierendeels. Development of correlations for windage power losses modeling in an axial flux permanent magnet synchronous machine with geometrical features of the magnets. *Energies*, 9, 1009:doi:10.3390/en9121009, 2016.

[17] A. Rasekh, P. Sergeant, and J. Vierendeels. Fully predictive heat transfer coefficient modeling of an axial flux permanent magnet synchronous machine with geometrical parameters of the magnets. *Applied Thermal Engineering*, 110:1343–1357, 2017.

[18] A. Rasekh, P. Sergeant, and J. Vierendeels. CFD-parametric study in stator heat transfer of an axial flux permanent magnet machine. *International Journal of Mechanical, Aerospace, Industrial, Mechatronic and Manufacturing Engineering*, 11(1):61–65, 2017.

[19] A. Rasekh, A. Hemeida, H. Vansompel, P. Sergeant, and J. Vierendeels. Influence of the curved-shape magnets on the performance of an axial flux permanent magnet synchronous machine. *To be submitted.*

[20] A. Rasekh, P. Sergeant, and J. Vierendeels. Heat transfer study in an enclosed rotor-stator system. *6th International Conference on Advanced Computational Methods in Engineering (ACOMEN), Ghent*, 2014.

[21] A. Rasekh, P. Sergeant, and J. Vierendeels. a parametric-CFD study for heat transfer and fluid flow in a rotor-stator system. *11th World Congress on Computational Mechanics (WCCM XI), Barcelona*, pages 4475–4483, 2014.

[22] A. Rasekh, P. Sergeant, and J. Vierendeels. A study of convective heat transfer in a rotor-stator system of disk-type electrical machines. *11th International Conference on Heat Transfer, Fluid Mechanics and Thermodynamics (HEFAT), South Africa*, pages 487–492, 2015.

[23] A. Rasekh, P. Sergeant, and J. Vierendeels. Stator heat transfer prediction of disk-type electrical machines. *Proceedings of the 1st Thermal and Fluid Engineering Summer Conference, (TFESC), New York*, pages 1–10, 2015.

[24] A. Hemeida, P. Sergeant, A. Rasekh, and J. Vierendeels. An optimal design of a 5MW AFPMSM for wind turbine applications using analytical model. *XXII International Conference on Electrical Machines (ICEM), Switzerland*, pages 1290–1297, 2016.

[25] A. Rasekh, P. Sergeant, and J. Vierendeels. Computational fluid dynamics (CFD)-parametric study in stator heat transfer of an Axial Flux Permanent Magnet Machine. *19th International Conference on Heat Transfer and Applications (ICHTA), London*, 2017.

[26] L. Alberti and N. Bianchi. A coupled thermal–electromagnetic analysis for a rapid and accurate prediction of IM performance. *IEEE Transactions on Industrial Electronics*, 55(10):3575–3582, 2008.

[27] B. Yoheswaran and K.R. Pullen. Flow and convective heat transfer in disk-type electric machines with coolant flow. *International Conference on Electrical Machines (ICEM)*, page 2165–2171, 2014.

[28] F. Sahin. Design and development of a high-speed axial-flux permanent machine. *Doctoral Thesis, Technische Universiteit Eindhoven*, page 2165–2171, 2014.

[29] J. Shazly, S. Wahsh, and A. Yassin. Thermal modeling of an AFPMSM: A review. *Journal of Electrical Systems and Information Technology*, 2:18–26, 2015.

[30] S. Kahourzade, A. Mahmoudi, H.W. Ping, and M.N. Uddin. A comprehensive review of axial-flux permanent-magnet machines. *Canadian Journal of Electrical and Computer Engineering*, 37(1):19–33, 2014.

[31] Y. Alexandrova, R.S. Semken, and J. Pyrhönen. Permanent magnet synchronous generator design solution for large direct-drive wind turbines: Thermal behavior of the LC DD-PMSG. *Applied Thermal Engineering*, 65:554–563, 2014.

[32] Y. Huai, R.V.N Melnik, and P.B. Thogersen. Computational analysis of temperature rise phenomena in electric induction motors. *Applied Thermal Engineering*, 23(7):779–795, 2003.

[33] F. Marignettia, V.D. Colli, and Y. Coia. Design of axial flux pm synchronous machines through 3-D coupled electromagnetic thermal and fluid-dynamical finite-element analysis. *IEEE Transactions on Industrial Electronics*, 55(10):3591–3601, 2008.

[34] F. Marignettia and V.D. Colli. Thermal analysis of an axial flux permanent-magnet synchronous machine. *IEEE Transactions on Magnets*, 45(7):2970–2975, 2009.

[35] G. Airoldi, G.L. Ingram, K. Mahkamov, J.R. Bumby, C. Dominy, N.L. Brown, A. Mebarki, and M. Shanel. Computations on heat transfer in axial flux permanent magnet machines. *Proceedings of the International Conference on Electrical Machines*, 2008.

[36] G. Airoldi, J.R. Bumby, C. Dominy, G.L. Ingram, C.H. Lim, K. Mahkamov, N.L. Brown, A. Mebarki, N.L. Brown, A. Mebarki, and M. Shanel. Air flow and heat transfer modeling of an axial flux permanent magnet generator. *International Journal of Mechanical, Aerospace, Industrial, Mechatronic and Manufacturing Engineering*, 3(10):1307–1311, 2009.

[37] S. Seghir-Oualil, S. Harmand, D. Laloy, and O. Phillipart. Study of the thermal behavior of a synchronous motor with permanent magnets. *International Journal of Engineering (IJE)*, pages 229–256, 2009.

[38] Z. Kolondzovski, A. Belahcen, and A. Arkkio. Multiphysics thermal design of a high-speed permanent-magnet machine. *Applied Thermal Engineering*, 29:2693–2700, 2009.

[39] Y.C. Chong, D.A. Magahy, J. Chick, M.A. Mueller, D.A. Staton, and A.S. McDonald. Numerical modelling of an axial flux permanent magnet machine for convection heat transfer. *IET Conference on Renewable Power Generation (RPG)*, 2011.

[40] Y.C. Chong, J.P. Echenique Subiabre, M.A. Mueller, J. Chick, D.A. Staton, and A.S. McDonald. The ventilation effect on stator convective heat transfer of an axial-flux permanent-magnet machine. *IEEE Transactions on Industrail Electronics*, 61(8):4392–4402, 2014.

[41] K. Sarrafan and A. Darabi. Steady state thermal analysis and design of a cooling system in an AFPM motor. *International Journal of Mechanical, Aerospace, Industrial, Mechatronic and Manufacturing Engineering*, 6(11):2582–2586, 2012.

[42] S. Kahourzade, A. Mahmoudi, A. Gandomkar, N.A. Rahim, H.W. Ping, and M.N. Uddin. Design optimization and analysis of afpm synchronous machine incorporating power density, thermal analysis, and back-EMF THD. *Progress In Electromagnetics Research*, 136:327–367, 2013.

[43] P. Moradnia and H. Nilsson. A parametric study of the air flow in an electric generator through stepwise geometry modifications. *An ECCOMAS Thematic Conference*, page 1–20, 2011.

[44] P. Moradnia, V. Chernoray, and H. Nilsson. Experimental assessment of a fully predictive CFD approach, for flow of cooling air in an electric generator. *Applied Energy*, 124:223–230, 2014.

[45] P. Moradnia, M. Golubev, V. Chernoray, and H. Nilsson. Flow of cooling air in an electric generator model - an experimental and numerical study. *Applied Energy*, 114:644–653, 2014.

[46] M. Polikarpova, P. Lindh, C. Gerada, M. Rilla V. Naumanen, and J. Pyrhönen. Thermal effects of stator potting in an axial-flux permanent magnet synchronous generator. *Applied Thermal Engineering*, 75:421–429, 2015.

[47] R. Wang, R.T. Dobson, and M.J. Kamper. Thermofluid analysis of an axial flux permanent magnet (AFPM) generator. *R & D journal*, 17(1):18–26, 2001.

[48] R. Wang, M.J. Kamper, and R.T. Dobson. Development of a thermofluid model for axial field permanent-magnet machines. *IEEE Transactions on Energy Conversion*, 20(1):80–87, 2005.

[49] S.T. Scowby, R.T. Dobson, and M.J. Kamper. Thermal modelling of an axial flux permanent magnet machine. *Applied Thermal Engineering*, 24:193–207, 2004.

[50] C.H. Lim, G. Airoldi, and K. Mahkamov. Experimental validation of CFD modelling for heat transfer coefficient predictions in axial flux permanent magnet generators. *International Journal of Thermal Sciences*, 50:2451–2463, 2011.

[51] R. Camilleri, P. Beard, D.A. Howey, and M.D. McCulloch. Measuring the heat transfer coefficient in a direct oil-cooled electrical machine using thin film heat flux gauges. *The 14th* UK *Heat Transfer Conference, (UKHTC)*, 2015.

[52] J. Pyrhönen, P. Lindh, M. Polikarpova, E. Kurvinen, and V. Naumanen. Heat-transfer improvements in an axial-flux permanent-magnet synchronous machine. *Applied Thermal Engineering*, 76:245–251, 2015.

[53] D.G. Dorrell. Combined thermal and electromagnetic analysis of permanent- magnet and induction machines to aid calculation. *IEEE transactions on industrial electronics*, 55(10):3566–3574, 2008.

[54] S. Yanhua and J. Chun. Thermal behavior of PM in-wheel motor used in off-road motor driven truck. *Procedia Engineering*, 23:222–228, 2011.

[55] J. Nerg and V. Ruuskanen. Lumped-parameter-based thermal analysis of a doubly radial forced-air-cooled direct-driven permanent magnet wind generator. *Mathematics and Computers in Simulation*, 90:218–229, 2013.

[56] K. Li, S. Wang, and P. Sullivan. A novel thermal network for the maximum temperature-rise of hollow cylinder. *Applied Thermal Engineering*, 52:198–208, 2013.

[57] S. Nategh, Z. Huang, A. Krings, O. Wallmark, and M. Leksell. Thermal modeling of directly cooled electric machines using lumped parameter and limited CFD analysis. *IEEE Transactions on Energy Convercion*, 28(4):979–990, 2013.

[58] C. Kral, A. Haumer, and S.B. Lee. A practical thermal model for the estimation of permanent magnet and stator winding temperatures. *IEEE Transactions on Power Electronics*, 29(1):455–464, 2014.

[59] R. Khlissa, S. Vivier, G. Friedrich, and K. Benkara B. Assaad. Thermal modeling of an asymmetrical totally enclosed permanent magnet integrated starter generator. *Mathematics and Computers in Simulation*, doi:10.1016/j.matcom.2015.06.015, 2016.

[60] J. Hey, D.A. Howey, R. Martinez-Botas, and M. Lamperth. Transient thermal modeling of an axial flux permanent magnet (AFPM) machine using a hybrid thermal model. *International Journal of Mechanical, Aerospace, Industrial, Mechatronic and Manufacturing Engineering*, 4(11):1274–1283, 2010.

[61] J. Hey, D.A. Howey, R. Martinez-Botas, and M. Lamperth. Transient thermal modelling of an axial flux permanent magnet (AFPM) machine with model parameter optimisation using a monte carlo method. *Vehichle Thermal Management Systems* VTMS, 10, 2011.

[62] C.H. Lim, G. Airoldi, J.R. Bumby, R.G. Dominy, G.I. Ingram, K. Mahkamov, N.L. Brown, A. Mebarki, and M. Shanel. Experimental and CFD investigation of a lumped parameter thermal model of a single-sided, slotted axial flux generator. *International Journal of Thermal Sciences*, 49:1732–1741, 2010.

[63] J.M. Owen. An approximation solution for flow between a rotating and stationary disk. *ASME Journal of Turbomachinery*, 111(4):323–332, 1989.

[64] N. Rostami, M.R. Feyzi, J. Pyrhönen, A. Parviainen, and M. Niemelä. Lumped-parameter thermal model for axial flux permanent magnet machines. *IEEE Transactions on Magnetics*, 49(3):1178–1184, 2013.

[65] C. Huynh, L. Zhneg, and D. Acharya. Losses in high speed permanent magnet machines used in microturbine applications. *Journal of Engineering for Gas Turbines and Power*, 131(2):1–6, 2008.

[66] B.C. Mecrow and A.G. Jack. Efficiency trends in electric machines and drives. *Energy Policy*, 36:4336–4341, 2008.

[67] E. Kurt, H. Gör, and U. Döner. Electromagnetic design of a new axial and radial flux generator with the rotor back-irons. *International Journal of Hydrogen Energy*, 71:7019–7026, 2016.

[68] S. Meoa, A. Zohoorib, and A. Vahedi. Optimal design of permanent magnet flux switching generator for wind applications via artificial neural network and multi-objective particle swarm optimization hybrid approach. *Energy Conversion and Management*, 110:230–239, 2016.

[69] C. Ruschetti, C. Verucchi, G. Bossio, C. De Angelo, and G.Garcia. Rotor demagnetization effects on permanent magnet synchronous machines. *Energy Conversion and Management*, 74:1–8, 2013.

[70] J.R Goulburn and J.H Wilson. High speed disk friction losses in a gaseous medium. *International Journal of Mechanical Sciences*, 17(6):379–385, 1975.

[71] P.H. Connor, S.J. Pickering, C. Gerada, C.N. Eastwick, and C. Micallef. CFD modelling of an entire synchronous generator for improved thermal management. *6th IET International Conference on Power Electronics, Machines and Drives (PEMD)*, page 1–6, 2012.

[72] H.P. Liu, C.S. Hearn, M.D. Werst, J.J. Hahne, and D. Bogard. Splits of windage losses in integrated transient rotor and stator thermal analysis of a high-speed alternator during multiple discharges. *IEEE Transactions on Magnetics*, 41(4):217–222, 2004.

[73] H.P. Liu, M.D. Werst, J.J. Hahne, and D. Bogard. Investigation of windage splits in an enclosed test fixture having a high speed composite rotor in low air pressure environments. *12th Symposium on Electromagnetic Launch Technology*, page 223–228, 2004.

[74] J.E. Vranick. Prediction of of windage power loss in alternators. *NASA Technical Note*, 4849:1–18, 1968.

[75] P.M. Wild, N. Djilali, and G.W. Vickers. Experimental and computational assessment of windage losses in rotating machinery. *J. Fluids Eng*, 118:116–122, 1996.

[76] K.R. Anderson, J. Lin, C. McNamara, and V. Magri. CFD study of forced air cooling and windage losses in a high speed electric motor. *Journal of Electronics Cooling and Thermal Control*, 5:27–44, 2015.

[77] T. El-Hasan, P.C.K. Luk, F.S. Bhinder, and M.S. Ebaid. Modular design of high-speed permanent-magnet axial-flux generators. *IEEE Transactions on Magnetics*, 36(5):3558–3561, 2000.

[78] M. Sadeghierad, A. Darabi, H. Lesani, and H. Monsef. Rotor yoke thickness of coreless high-speed axial-flux permanent magnet generator. *IEEE Transactions on Magnetics*, 45(4):2032–2037, 2009.

[79] J.F. Gieras. Design of permanent magnet brushless motors for high speed applications. *17th International Conference on Electrical Machines and Systems (ICEMS)*, pages 1–16, 2014.

[80] A. Giovanni. Numerical investigations of air flow and heat transfer in axial flux permanent magnet electrical machines. *Doctoral Thesis, Durham University*, 2010.

[81] R. Wrobel, G. Vainel, C. Copeland, T. Duda, D. Staton, and P.H. Mellor. Investigation of mechanical loss and heat transfer in an axial-flux pm machine. *IEEE Energy Conversion Congress and Exposition*, pages 4372–4379, 2013.

[82] X. Luo, D. Zhang, Z. Tao, G. Xu, and Q. Wang. Windage measurements in a rotor-stator system with superimposed cooling and rotor-mounted protrusions. *Journal of Engineering for Gas Turbines and Power*, 136:1–11, 2014.

[83] D. Liu, Z. Taho, X. Luo, W. Kang, H. Wu, and X. Yu. Investigation on the impact of protrusion parameter on the efficiency of converting additional windage loss for ingress alleviation in rotor-stator system. *Journal of Engineering for Gas Turbines and Power*, doi:10.1115/1.4033617, 2016.

[84] R. Wrobel, G. Vainel, C. Copeland, T. Duda, D. Staton, and P.H. Mellor. Investigation of mechanical loss components and heat transfer in an axial-flux pm machine. *IEEE Transactions on Industry Applications*, 51:3000–3011, 2015.

[85] G.K. Batchelor. Note on a class of solutions of the Navier-Stokes equations representing steady rotationally-symmetric flow. *Journal of Mechanics and Applied Mathematics*, 4(1):29–41, 1951.

[86] K. Stewartson. On the flow between two rotating coaxial disks. *Mathematical Proceedings of the Cambridge Philosophical Society,*, 49(2):333–341, 1953.

[87] K.G. Picha and E.R.G. Eckert. Study of the air flow between coaxial discs rotating with arbitrary velocities in an open or enclosed space. *In Proc. 3rd U.S. Nat. Cong. Appl. Mech*, page 791–798, 1958.

[88] S.L. Soo. Laminar flow over an enclosed rotating disc. *Transactions of the ASME. Series D, Journal of Basic Engineering*, 80:287–296, 1958.

[89] J.W. Daily and R.E. Nece. Chamber dimension effects on induced flow and frictional resistance of enclosed rotating disks. *Transactions of the ASME. Series D, Journal of Basic Engineering*, 16(10):731–741, 1978.

[90] G.N. Lance and M.H. Rogers. The axially symmetric flow of a viscous fluid between two infinite rotating disks. *Proceedings of the Royal Society A*, 266:109–121, 1962.

[91] C.E. Pearson. Numerical solutions for the time-dependent viscous flow between two rotating coaxial disks. *Journal of Fluid Mechanics*, 21(4):623–633, 1965.

[92] G.L. Mellor, P.J. Chapple, and V.K. Stokes. On the flow between a rotating and a stationary disk. *Journal of Fluid Mechanics*, 31(1):95–112, 1968.

[93] P.Cooper and E. Reshotko. Turbulent flow between a rotating disk and a parallel wall. *AIAA Journal*, 13:573–578, 1975.

[94] R. Kobayashi. Review: Laminar-to-turbulent transition of three-dimensional boundary layers on rotating bodies. *Trans. ASME J. Fluids Engng*, 116:200–211, 1994.

[95] M. Itoh, Y. Yamada, S. Imao, and M. Gonda. Experiments on turbulent flow due to an enclosed rotating disk. *Expl Thermal Fluid Sci*, 5:359–368, 1992.

[96] M. Singh and S.C. Rajvanshi. Computation of the flow between a rotating and a stationary naturally permeable disk. *International Journal of Engineering Science*, 82:217–232, 1960.

[97] N.M. Bujurke and P.K. Achar. A semi-analytic approach to the viscous flow between a rotating and a stationary disk. *Fluid Dynamics Research*, 10(2):91–99, 1992.

[98] S.C. Cheah, H. Iacovides, D.C. Jackson, H. Ji, and B.E. Launder. Experimental investigation of enclosed rotor-stator disk flows. *Experimental Thermal and Fluid Science*, 9(4):445–455, 1994.

[99] S. Bhattacharyya and A. Pal. On the flow between two rotating disks enclosed by a cylinder. *Acta Mechanica*, 135(1):27–40, 1999.

[100] E. Severac, S. Poncet, E. Serre, and M. Chauve. Large eddy simulation and measurements of turbulent enclosed rotor-stator flows. *Physics of Fluids*, 19(8):085113, 2007.

[101] M. Lygren and H.I. Andersson. Turbulent flow between a rotating and a stationary disk. *J. Fluid Mech*, 426:297–326, 2001.

[102] M. Lygren and H.I. Andersson. Turbulence statistics in an open rotor–stator configuration. *Phys. Fluids*, 14(3):1137–1145, 2002.

[103] R. Jacques, P. Le Quere, and O. Daube. Axisymmetric numerical simulations of turbulent flow in rotor stator enclosures. *International Journal of Heat and Fluid Flow*, 23:381–397, 2002.

[104] H.I. Andersson and M. Lygren. LES of open rotor–stator flow. *International Journal of Heat and Fluid Flow*, 27:551–557, 2006.

[105] A. Cros, E. Floriani, P.L. Gal, and R. Lima. Transition to turbulence of the batchelor flow in a rotor/stator device. *European Journal of Mechanics - B/Fluids*, 24:409–424, 2005.

[106] B. Launder, S. Poncet, and E. Serre. Laminar, transitional, and turbulent flows in rotor-stator cavities. *Annual Review of Fluid Mechanics*, 42:229–248, 2009.

[107] D.A. Howey. Thermal design of air-cooled axial flux permanent magnet machines. *Doctoral Thesis, Imperial College London*, 2010.

[108] S.L. Soo, R.W. Besant, and Z.N. Sarafa. The nature of heat transfer from an enclosed rotating disk. *Zeitschrift für Angewandte Mathematik und Physik (ZAMP)*, 13(4):297–309, 1962.

[109] J.M. Owen. The Reynolds analogy applied to flow between a rotating and a stationary disc. *International Journal of Heat and Mass Transfer*, 14:451–460, 1971.

[110] J.M. Owen. The effect of forced flow on heat transfer from a disc rotating near a stator. *International Journal of Heat and Mass Transfer*, 14:1135–1147, 1971.

[111] R.C. Arora and V.K. Stokes. On the heat transfer between two rotating disks. *International Journal of Heat and Mass Transfer*, 15(11):2119–2132, 1972.

[112] C.Y. Soong and H.L. Ma. Unsteady analysis of non-isothermal flow and heat transfer between rotating co-axial disks. *International Journal of Heat and Mass Transfer*, 38(10):1865–1878, 1995.

[113] M. Wilson, R. Pilbrow, and J.M. Owen. Flow and heat transfer in a preswirl rotor-stator system. *J. Turbomach*, 119(2):364–373, 1997.

[114] S. Harmand, B. Watel, and B. Desmet. Local convective heat exchanges from a rotor facing a stator. *Int. J. Therm. Sci.*, 39:404–413, 2000.

[115] C.M. Ellwood and W.J. Korchinsky. The heating, by viscous dissipation, of liquids flowing across an enclosed rotating disc. *International Journal of Heat and Mass Transfer*, 43:1035–1050, 2000.

[116] R.P. Roy, G. Xu, and J. Feng. A study of convective heat transfer in a model rotor–stator disk cavity. *Journal of Turbomachinery*, 123:621–632, 2001.

[117] R. Boutarfa and S. Harmand. Local convective heat exchanges and flow structure in a rotor–stator system. *International Journal of Thermal Sciences*, 42(12):1129–1143, 2003.

[118] G.P. Beretta and E. Malfa. Flow and heat transfer in cavities between rotor and stator disks. *International Journal of Heat and Mass Transfer*, 46:2715–2726, 2003.

[119] J. Pelle´ and S. Harmand. Heat transfer measurements in an opened rotor–stator system air-gap. *Experimental Thermal and Fluid Science*, 31:165–180, 2007.

[120] J. Pelle´ and S. Harmand. Heat transfer study in a discoidal system: The influence of rotation and space between disks. *International Journal of Heat and Mass Transfer*, 51:3298–3308, 2008.

[121] J. Pelle´ and S. Harmand. Heat transfer study in a rotor–stator system air-gap with an axial inflow. *Applied Thermal Engineering*, 29:1532–1543, 2009.

[122] J. Pelle´ and S. Harmand. Convective heat transfer in a rotor stator system air gap with multiple suctions of fluid through the stator. *Journal of Heat Transfer*, 133(11):111702, 2011.

[123] H. Karabay, M. Wilson, and J.M. Owen. Predictions of effect of swirl on flow and heat transfer in a rotating cavity. *International Journal of Heat and Fluid Flow*, 22(2):143–155, 2001.

[124] H.H. Cho, C.H. Won, G.Y. Ryu, and D.H. Rhee. Local heat transfer characteristics in a single rotating disk and co-rotating disks. *Microsystem Technologies*, 9(6):399–408, 2003.

[125] R. Boutarfa and S. Harmand. Local convective heat transfer for laminar and turbulent flow in a rotor-stator system. *Experiments in Fluids*, 38(2):209–221, 2005.

[126] S. Poncet and R. Schiestel. Numerical modeling of heat transfer and fluid flow in rotor–stator cavities with throughflow. *International Journal of Heat and Mass Transfer*, 50(7-8):1528–1544, 2007.

[127] A. Nazir and T. Mahmood. Analysis of flow and heat transfer of viscous fluid between contracting rotating disks. *Applied Mathematical Modelling*, 35(7):3154–3165, 2011.

[128] S. Harmand, J. Pellé, S. Poncet, and I.V. Shevchuk. Review of fluid flow and convective heat transfer within rotating disk cavities with impinging jet. *International Journal of Thermal Sciences*, 67:1–30, 2013.

[129] S. Poncet, T.D. Nguyen, S. Harmand, J. Pellé, R. Da Soghe, C. Bianchini, and S. Viazzo. Turbulent impinging jet flow into an unshrouded rotor-stator system: Hydrodynamics and heat transfer. *International Journal of Heat and Fluid Flow*, 44:719–734, 2013.

[130] G. Liao, X. Wang, J. Li, and J. Zhou. Numerical investigation on the flow and heat transfer in a rotor-stator. *Applied Thermal Engineering*, 87:10–23, 2015.

[131] Z.X. Yuan, N. Saniei, and X.T. Yan. Turbulent heat transfer on the stationary disk in a rotor-stator system. *International Journal of Heat and Mass Transfer*, 46(12):2207–2218, 2003.

[132] D.A. Howey, A.S. Holmes, and K.R. Pullen. Prediction and measurement of heat transfer in air-cooled disc-type electrical machines. *Power Electronics, Machines and Drives (PEMD), 5th IET International Conference on*, 2010.

[133] D.A. Howey, A.S. Holmes, and K.R. Pullen. Measurement of stator heat transfer in air-cooled axial flux permanent magnet machines. *Industrial Electronics, IECON'09. 35th Annual Conference of IEEE*, pages 1197–1202, 2009.

[134] D.A. Howey, A.S. Holmes, and K.R. Pullen. Measurement and CFD prediction of heat transfer in air-cooled disc-type electrical machines. *IEEE Transactions on Industry Applications*, 47(4):1716–1723, 2011.

[135] D.A. Howey, A.S. Holmes, and K.R. Pullen. Radially resolved measurement of stator heat transfer in a rotor–stator disc system. *International Journal of Heat and Mass Transfer*, 53:491–501, 2010.

[136] D.A. Howey, P.R.N. Childs, and A.S. Holmes. Air-gap convection in rotating electrical machines. *IEEE Transaction on Industrial Electronics*, 59(3):1367–1375, 2012.

[137] R. Jacques. Numerical simulations of transitional and turbulent flows in rotor-stator configurations. *Doctoral Thesis, University of Paris*, 1997.

[138] G. Verez, H. Tiegna, G. Barakat, and G. Hoblos. Analytical thermal modelling of axial flux permanent magnet synchronous machines. *Proc. IEEE 20th Int. Conf. Elect. Mach. (ICEM)*, page 2799–2805, 2012.

[139] H. Vansompel, P. Sergeant, L. Dupré, and A. Van den Bossche. Axial-Flux PM machines with variable air gap. *IEEE Transactions on Industrial Electronics*, 61(2):730–737, 2014.

[140] D. Kowal, P. Sergeant, L. Dupré, and A. Van den Bossche. Comparison of nonoriented and grain-oriented material in an axial flux permanentmagnet machine. *IEEE Trans. Magn*, 46(2):279–285, 2010.

[141] G. Bertotti. General properties of power losses in soft ferromagnetic materials. *IEEE Transactions on Magnets*, 24(1):621–630, 1988.

[142] A.S. Fawzal, R.M. Cirstea, K. Gyftakis, T.J. Woolmer, M. Dickison, and M.V. Blundell. The fan design impact on the rotor cooling of axial flux permanent magnet machines. *International Conference on Electrical Machines (ICEM)*, pages 2727–2733, 2016.

[143] F.P. Incropera, D.P. DeWitt, T.L. Bergman, and A.S. Lavine. Fundamentals of heat and mass transfer. *John Wiley and Sons, Inc.*, 2007.

[144] S.W. Churchill and H.H.S. Chu. Correlating equations for laminar and turbulent free convection from a vertical plate. *Int. J. Heat Mass Transfer*, 18:1323–1329, 1975.

[145] E. Dick. Fundamentals of Turbomachines. *London, Springer*, 2015.